

# GYRORESONANT SCATTERING OF RADIATION BELT ELECTRONS BY OBLIQUE WHISTLER WAVES


A DISSERTATION  
SUBMITTED TO THE DEPARTMENT OF ELECTRICAL ENGINEERING  
AND THE COMMITTEE ON GRADUATE STUDIES  
OF STANFORD UNIVERSITY  
IN PARTIAL FULFILLMENT OF THE REQUIREMENTS  
FOR THE DEGREE OF  
DOCTOR OF PHILOSOPHY

Jasna Ljiljane Ristić-Djurović


May 1993

© Copyright by Jasna Ljiljane Ristić-Djurović 1993  
All Rights Reserved

I certify that I have read this dissertation and that in my opinion it is fully adequate, in scope and quality, as a dissertation for the degree of Doctor of Philosophy.

  
\_\_\_\_\_  
Umran S. Inan (Principal Advisor)

I certify that I have read this dissertation and that in my opinion it is fully adequate, in scope and quality, as a dissertation for the degree of Doctor of Philosophy.

  
\_\_\_\_\_  
Timothy F. Bell

I certify that I have read this dissertation and that in my opinion it is fully adequate, in scope and quality, as a dissertation for the degree of Doctor of Philosophy.

  
\_\_\_\_\_  
Albert Macovski

Approved for the University Committee on Graduate Studies:

\_\_\_\_\_

*мами с љубављу*

## Abstract

Radiation belts consist of high energy (ten of eV to tens of MeV) electrons and ions trapped by the Earth's magnetic field with particle source and loss processes in a dynamic equilibrium. When scattered in pitch angle, the energetic electrons precipitate into the upper atmosphere where they cause significant disturbances (produce heating, secondary ionization and conductivity enhancement, emit light or X-rays). Interactions with electromagnetic waves are an important means of loss of these particles from the radiation belts. The Earth's magnetoplasma supports a large variety of natural and man-made electromagnetic waves amongst which are whistler-mode waves. Whistler mode waves are typically in the very low frequency range (hundreds of Hz to tens of kHz), below the electron gyrofrequency so that they can resonantly interact with radiation belt electrons resulting in their precipitation out of the radiation belts and into the atmosphere. A computer simulation model is developed to study the interaction between relativistic charged particles and whistler mode waves traveling obliquely with respect to the ambient magnetic field. This new model is used to investigate the importance of gyroresonant scattering of radiation belt electrons by oblique whistler waves in electron loss from the radiation belts. Application of the model to the parameters of the inner magnetosphere ( $L \leq 4$ ) revealed that: (i) oblique whistlers can efficiently scatter significant fluxes of suprathermal (10–100 eV) electrons, (ii) higher energy electrons are precipitated from lower L-shells and that corresponding precipitated differential electron flux and total precipitated energy flux are higher for higher L-shells, and (iii) electron lifetimes due to this loss process are calculated to be of the order of several days, and are comparable with lifetimes corresponding to other loss mechanisms (e.g., electron-hiss interactions).

## Preface

The time I have spent at Stanford since I came in the Fall of 1989, working on the material presented here, was the most challenging, exciting and rewarding professional experience, but also the most difficult time in my personal life. There are quite a few people whom I would like to thank for sharing the good times and for being with me when I needed help.

My principal advisor Umran Inan is the most energetic, enthusiastic and practical person I have ever met. Not only does he always have time to discuss any research oriented questions, but he also makes an effort to notice and help with any problems that his students might have even if they are not research related. I thank him for everything I have learned from him, for all the support and trust in me, for the opportunity to conduct interesting and challenging research and present it worldwide. I admire Tim Bell, my associate advisor, as a 'theoretical wizard'. I'm grateful for his generous sharing with me the results of his amazing capability to grasp the physical and practical meaning of the most complicated equations, as well as for encouragement when I needed it the most. I thank Martin Walt for many useful comments on the research, for being a member of my thesis defense committee and for all the improvements of this thesis due to his careful reading. I would also like to express my gratitude to Professor Albert Macovski for cheerfully reading and commenting on this dissertation despite his very busy schedule. My thanks go to Professor Stephen Boyd for chairing and to Professor Leonard Tyler for being a member of my oral defense committee.

I also appreciate the help of Vikas Sonwalkar with the raytracing code and reference searches; the many educational conversations I have had with Professor Helliwell and Don Carpenter whose warm welcome to Stanford in my mother tongue I'll never forget; the wit and encouragement of Tony

Fraser-Smith; the assistance of Jerry Yarbrough with spectrograms; and the helpfulness of Jenny Xu and June Wang in administrative work. It has been a great pleasure to discuss various topics both related to our research and to everyday life with my fellow graduate students in VLF group. In particular, I would like to mention and thank Juan Rodriguez, Lee Poulsen, Bill Burgess and Yuri Taranenko.

I am lucky to have numerous friends living both near and far, whom I owe for the wonderful time spent together, for the moral support, encouragement, and listening ear. I can only hope that they enjoyed and benefited from our friendship as much as I did. My special thanks go to my eternal neighbor Boža, roommates Natalie and Vivien, Brian, Chandra and Jelena.

The most important of all is that this dissertation is not only mine, but that it also belongs to a very special lady, my mom, Ljiljana Ristic. I will not even try to put in words what I feel when I think of her, because even if it was expressible nobody would understand it. She, on the other hand, doesn't need words, she knows.

Jasna

Stanford,  
May 1993

Financial support for this research was provided by the National Aeronautics and Space Administrations under grant NAGW-1582.

# Contents

<b>Abstract .....</b>	<b>v</b>
<b>Preface .....</b>	<b>vi</b>
<b>Contents.....</b>	<b>viii</b>
<b>Tables .....</b>	<b>x</b>
<b>Illustrations .....</b>	<b>xi</b>
<b>1. Introduction .....</b>	<b>1</b>
1.1. Magnetosphere.....	1
1.1.1. Radiation Belts .....	7
1.1.2. Cyclotron resonance .....	10
1.2. Review of Previous Work .....	12
1.3. Contributions of the Present Work .....	15
<b>2. Preliminary Assessment of the Efficiency of Cyclotron Resonant Interactions Between Electrons and Oblique Whistlers .....</b>	<b>17</b>
2.1. Equatorial Gyroresonance With the Raytraced Whistlers.....	18
2.1.1. Method of Calculation .....	19
2.1.2. Results .....	21
2.1.3. Conclusions .....	27
2.2. Gyro-averaged Pitch Angle Diffusion.....	27
2.2.1. Gyro-averaged Diffusion Coefficient.....	28
2.2.2. Results .....	30
2.2.3. Conclusions .....	32
<b>3. Theoretical Formulation .....</b>	<b>35</b>
3.1. Mathematical Model of the Cold Magnetoplasma Medium .....	36
3.2. Oblique Whistler-Mode Waves .....	38
3.3. Unperturbed Electron Trajectories .....	44
3.4. Test Particle Equations of Motion .....	46



<b>4. Test Electron Trajectories</b> .....	55
4.1. Problem Formulation .....	55
4.2. Test Particle Trajectories.....	58
4.3. Precipitated Energy Flux Estimates.....	62
4.4. Conclusions .....	64
<b>5. The Interaction Between an Oblique Whistler-Mode Wave and a Full Distribution of Electrons</b> .....	67
5.1. Theoretical Introduction .....	68
5.1.1. Electron Velocity Space .....	68
5.1.2. Particle and Energy Fluxes.....	73
5.1.3. Particle Lifetimes.....	75
5.2. Initial Conditions and Assumptions .....	78
5.2.1. Initial Electron Distribution Function.....	78
5.2.2. Assumptions Concerning the Resonant Wave .....	79
5.3. Comparison of Precipitated Energy Fluxes for Suprathermal and Energetic Electrons .....	80
5.4. Magnetospherically Reflected (MR) Whistlers.....	87
5.5. Electron Precipitation by MR Whistlers.....	91
5.6. Interaction With Incoherent Signals.....	101
<b>6. Summary and Conclusions</b> .....	105
6.1. Radiation Belt Equilibrium.....	105
6.2. Effects on the Upper Ionosphere .....	108
6.2.1. Ionospheric Disturbances Caused by Suprathermal Electrons .....	109
6.2.2. On Secondary Ionization in the Lower Ionosphere Caused by MR Whistlers .....	110
<b>7. Suggestions for Future Work</b> .....	113
7.1. Applications of the Test Particle Simulation Model.....	113
7.2. Further Developments of the Model .....	115
<b>References</b> .....	117

# Tables

2.1. Equatorial electron density and pitch angles .....	29
5.1. Dimensions of various quantities .....	75
5.2. Parameters of non-ducted waves .....	92
5.3. Simulation parameters .....	92

# Illustrations

1.1. Magnetosphere .....	2
1.2. Inner magnetosphere .....	2
1.3. Equatorial electron density .....	4
1.4. Ducted and non-ducted whistler-mode waves .....	5
1.5. Whistler mode waves .....	6
1.6. The trajectory of a radiation belt electron .....	8
1.7. Dependence of electron trajectories on the equatorial pitch angle .....	9
1.8. Electron-wave cyclotron resonance .....	11
2.1. Example of an MR whistler .....	18
2.2. Sample raypath .....	20
2.3. Equatorial electron density profile .....	21
2.4. Resonant electron energy along the raypath .....	23
2.5. Equatorial resonant electron energy dependence on the ray parameters .....	25
2.6. The dependence of equatorial resonant electron energy on the wave normal angle at the injection point .....	26
2.7. Wave frequencies and diffusion coefficients .....	31
3.1. Dipole magnetic field geometry .....	37
3.2. Wave vector orientation .....	39

3.3. Wave refractive index .....	42
3.4. Wave polarization: electric field .....	42
3.5. Wave polarization: magnetic field .....	43
3.6. Wave phase and group velocities .....	43
3.7. Wave-particle interaction geometry .....	48
3.8. Electron phase with respect to the wave .....	49
4.1. Schematic illustration of the electron-oblique wave interaction.....	56
4.2. Dependence of wave frequency on wave normal angle $\psi$ for equatorial gyroresonance .....	57
4.3. Sample raypath.....	58
4.4. Sample trajectories of suprathermal ( $E=100$ eV) electrons .....	60
4.5. Sample trajectories of energetic ( $E=100$ keV) electrons.....	61
4.6. Dependence of electron scattering on initial electron velocity for suprathermal ( $E=100$ eV) electrons .....	63
4.7. Dependence of electron scattering on initial electron velocity for energetic ( $E=100$ keV) electrons .....	64
5.1. Velocity space cells .....	68
5.2. Test electron trajectories in the velocity space .....	70
5.3. A single test electron scattering in velocity space .....	71
5.4. Coordinate transformation .....	72
5.5. Velocity space grid transformation .....	73
5.6. Mapping of the pitch angle distribution.....	77
5.7. Modification of velocity space area .....	81

5.8. Fluctuation or 'noise' level for pitch angle scattering .....	83
5.9. Initial and final distribution .....	84
5.10. The precipitated differential energy spectrum.....	86
5.11 MR whistlers observed on the DE-1 satellite .....	88
5.12. Sample raypath for an MR signal .....	89
5.13. The frequency of the MR whistler wave vs $L$ -shell of settlement .....	90
5.14. Dependence of particle scattering on initial $v_{z_{eq}}$ .....	93
5.15. Dependence of the wave parameters on geomagnetic latitude along the field line .....	94
5.16. The initial and final near-loss-cone distributions for a one-pass interaction with a 0.33 kHz whistler wave at $L=4$ .....	97
5.17. Precipitated differential electron spectra .....	98
5.18. Electron lifetimes .....	99
5.19. Electron lifetimes compared with previous work .....	100
5.20. Test trajectories for electrons interacting with incoherent signals .....	103



# 1.

## Introduction

This thesis constitutes a theoretical investigation of the pitch angle and energy scattering of electrons trapped in the Earth's radiation belts by very low frequency (VLF) whistler-mode waves propagating obliquely with respect to the Earth's magnetic field. The scattering occurs as a result of cyclotron resonant interactions between the waves and the particles. The physical consequences are of significance because a variety of VLF waves propagate in the Earth's radiation belts and may dominantly effect their dynamics. In this chapter, we introduce the terminology, provide a brief background on the phenomena, discuss previous work, and outline the contributions of this dissertation.

### 1.1. Magnetosphere

The Earth's *magnetosphere* is the space surrounding the Earth, filled with relatively low density ionized gas, permeated by the Earth's magnetic field. Its boundaries separate plasmas which are under the influence of interplanetary

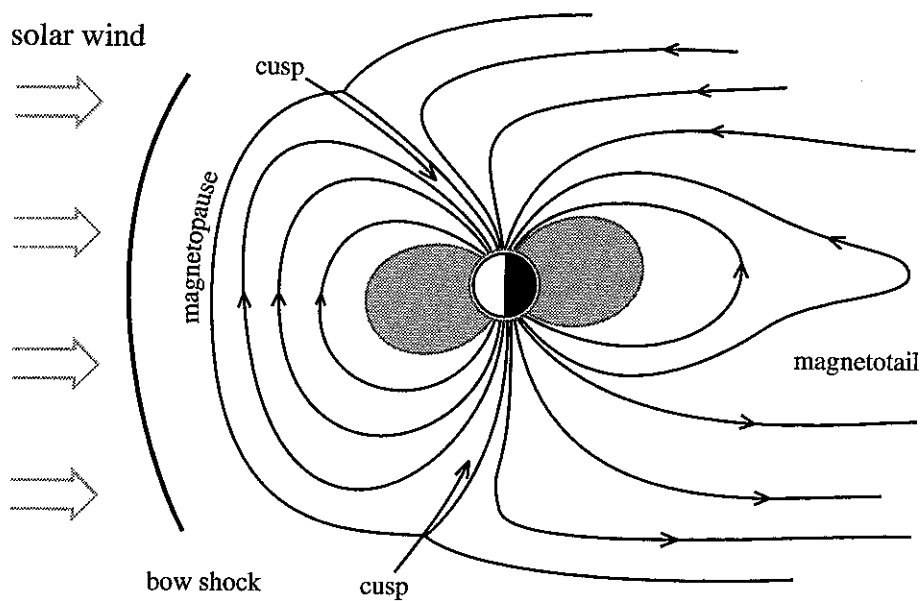


**Figure 1.1. Magnetosphere.** The Earth's dipole-like magnetic field lines are distorted by the solar wind, forming a bow shock where the supersonic solar wind is thermalized and becomes subsonic. The magnetopause separates Earth's and interplanetary magnetic fields and plasmas.

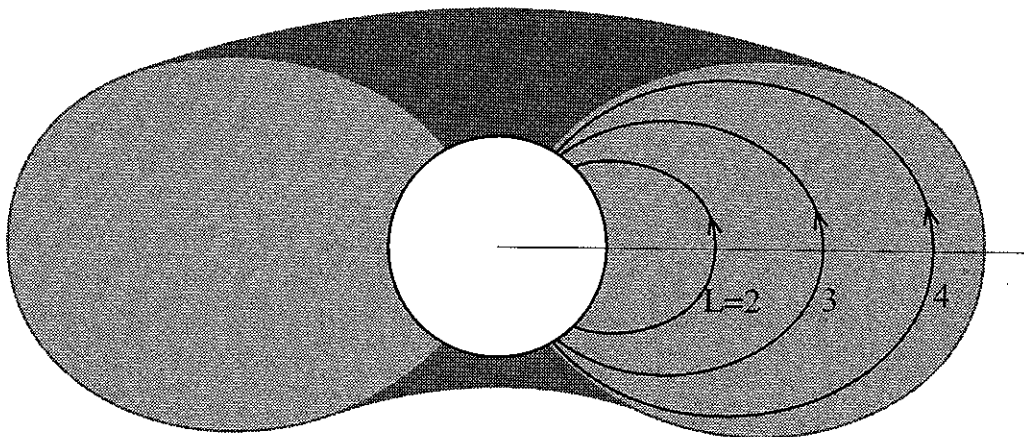


**Figure 1.2. Inner magnetosphere.** The Earth's magnetic field lines in the inner magnetosphere are not significantly distorted by the solar wind. Magnetic field lines crossing the equatorial geomagnetic plane at the same distance from the center of the Earth form an  $L$ -shell. The  $L$ -shell number represents its equatorial radial distance in Earth radii. The shaded surface represents  $L = 4.5$ , whereas  $L = 2, 3$  and  $4$  are each represented only by a single corresponding magnetic field line.



and Earth's magnetic fields, and are defined by the interaction of the supersonic solar wind with the geomagnetic field [Akasofu and Chapman, 1972]. A schematic picture of the magnetosphere is shown in Figure 1.1. In the sunward direction the Earth's dipole-like internal magnetic field, whose axis is inclined at  $\sim 11^\circ$  with respect to the rotational axis, is compressed by the solar wind. A collisionless bow shock is formed where the solar wind, due to its interaction with the magnetosphere, becomes thermalized and subsonic. Further downstream is the first magnetosphere boundary – the **magnetopause**. A rough estimate of its position, determined by balancing the solar wind pressure and the Earth's magnetic field pressure, places the magnetopause at about ten Earth radii under geomagnetically quiet conditions. In the anti-sunward direction, magnetic field lines are dragged away from the Earth to form the **magnetotail** which represents the extension of the magnetosphere beyond the moon to several hundred Earth radii.

The part of the magnetosphere where the Earth's magnetic field lines are not significantly distorted by the solar wind and where the field can be approximated by a centered dipole is referred to in this thesis as the **inner magnetosphere**, as shown in Figure 1.2.

Magnetic field lines crossing the geomagnetic equatorial plane at the same distance from the center of the Earth form a surface that is defined as an **L-shell**. The ambient relatively low density and low energy (cold) ionized gas in the inner magnetosphere is created through ionization of neutrals by solar ultra-violet radiation at the daytime atmosphere – magnetosphere boundary [Banks and Kockarts, 1973], and it consists of electrons and positive ions ( $H^+$ ,  $He^+$  and  $O^+$ ) in diffusive equilibrium [Angerami and Thomas, 1964]. The particle density in this background cold plasma ranges from a few thousands to several particles per cubic centimeter [Park et al., 1978]. The typical variation of the electron concentration at the equatorial plane with radial distance from the Earth in Earth radii (or L-value by above definition) is shown in Figure 1.3. An abrupt boundary at which the electron concentration drops by roughly two orders of magnitude is known as the **plasmopause** [Carpenter, 1963, 1966]. Its position (equatorial distance from the Earth's

center) varies significantly with geomagnetic activity, from two Earth radii following major magnetic substorms up to seven Earth radii after long (several days) quiet periods [Carpenter, 1966]. Electrons and ions in this background ‘cold’ plasma have low energies, typically in the 0.1 eV – 1 eV range.

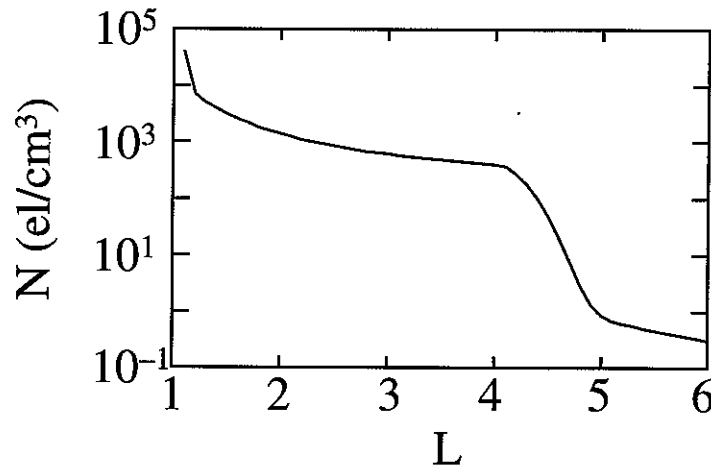


**Figure 1.3. Equatorial electron density.** Typical equatorial ambient cold electron density as a function of  $L$ -shell, with the plasmapause being at  $L \sim 4.5$ .

As a magnetized plasma, the magnetosphere constitutes a dispersive, anisotropic, and inhomogeneous medium that supports a large variety of natural and man-made electromagnetic waves over a very broad frequency range, ranging from fractions of a Hz to few MHz. Amongst the waves supported by the magnetosphere is a special class of extremely low frequency (ELF) and very low frequency (VLF) waves (tens of Hz to tens of kHz) called whistler-mode waves, due to the fact that a particular kind of whistler-mode wave, injected into the magnetosphere by lightning discharges and known as a ‘whistler’, produces a whistling sound when detected in the conjugate hemisphere with the receiver connected to an audio speaker [Helliwell, 1965]. ELF/VLF waves can propagate through the magnetosphere in either ducted or non-ducted modes as shown in Figure 1.4. Ducted waves travel within background density enhancements called *ducts*, formed around particular magnetic field lines [Helliwell, 1965]. As the waves propagate in the duct, much like light traveling in a graded optical fiber, the wave vector

remains approximately parallel (within  $\pm 30^\circ$ ) to the magnetic field line [Helliwell, 1965]. Because of their near normal incidence to the sharp lower ionospheric boundary, ducted waves can penetrate through the narrow transmission cone of the lower ionosphere to reach the Earth's surface where

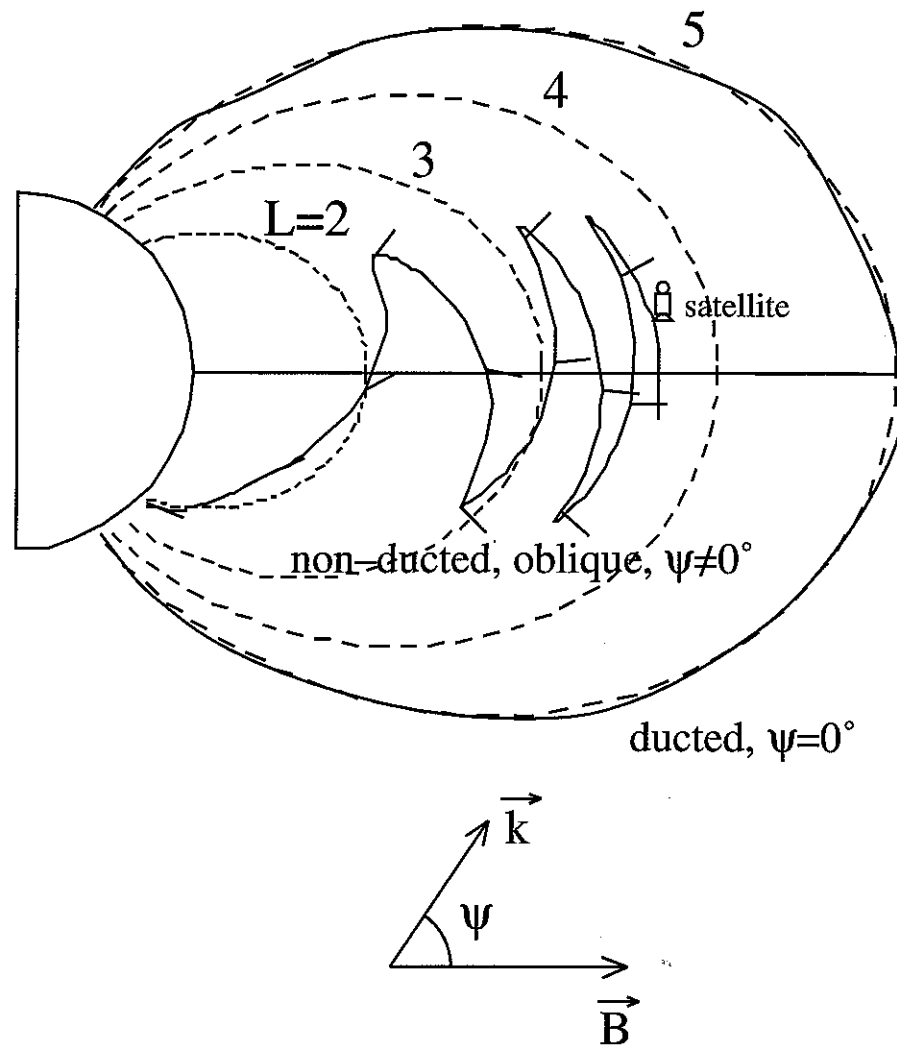


**Figure 1.4. Ducted and non-ducted whistler-mode waves.** Ducted waves travel within background plasma density enhancements called 'ducts'; their wave normal angle is approximately parallel to the magnetic field line, they penetrate through the sharp lower ionospheric boundary and are detected on the ground. Non-ducted waves propagate with their wave normal at a substantial angle with respect to the magnetic field line; they are typically reflected within the magnetosphere before they reach the ionosphere, and they can typically be detected only *in situ*.

they can be detected by ground based receivers. Non-ducted waves propagate obliquely with their wave vectors at a substantial angle with respect to the magnetic field line, and they are either reflected within the magnetosphere before they reach the ionosphere (the reflections occur where the wave frequency is equal to the local lower hybrid resonance frequency [Edgar, 1976]) or are specularly reflected at the sharp lower ionospheric boundary due to their highly oblique incidence. Non-ducted waves can typically be detected only *in situ*, on spacecraft or rockets. Whistler mode waves can be incoherent or coherent signals. Incoherent, broadband noise-like signals, generally with well defined upper and lower cutoff frequencies, are referred to as hiss [Gurnett and Frank, 1972; Thorne *et al.*, 1973; Laaspere and Hoffman, 1976], whereas examples of narrowband coherent VLF waves are natural

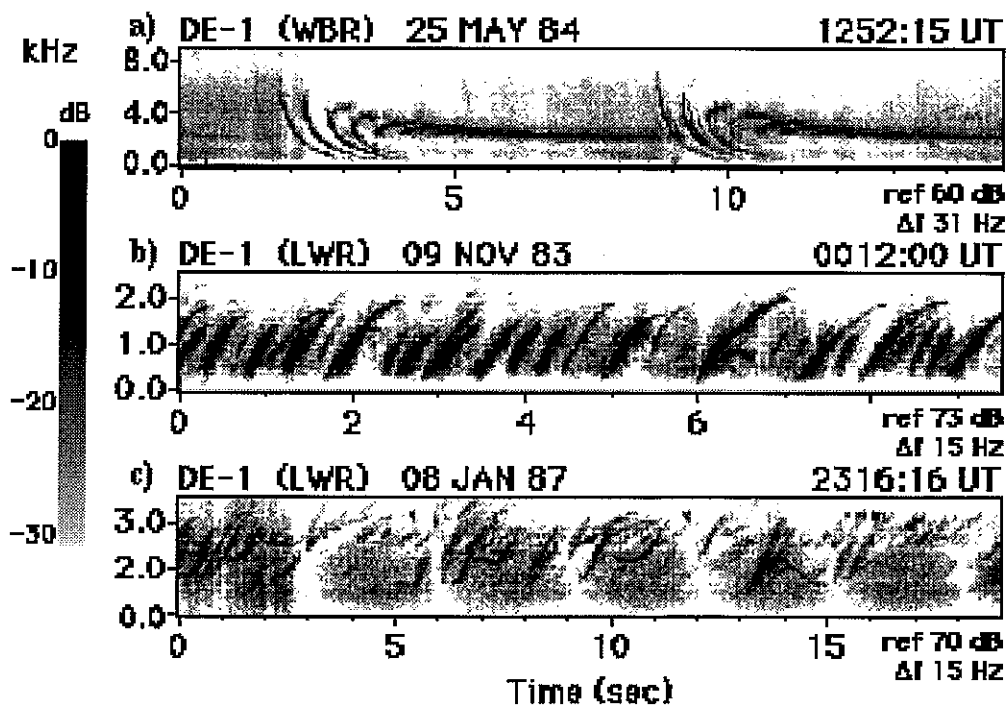


**Figure 1.5. Whistler mode waves.** Frequency vs time spectra of electromagnetic whistler-mode signals observed on the DE-1 satellite [Gurnett and Inan, 1988]. Note that darker shades represents stronger signals. a) 25 May 84, two multihop whistlers with well distinguished first four hops. b) 9 Nov. 83, chorus with strong and clear rising tones. c) 8 Jan. 87, chorus with more complex structure.

whistlers generated by lightning, discrete 'chorus' emissions, harmonic radiation from large scale power grids, signals from ground based transmitters and triggered emissions [Helliwell, 1965; Helliwell and Katsufakis, 1974; Helliwell et al., 1975; Park, 1976]. Whistler mode waves are of special importance because their frequencies and propagation velocities are low enough for resonant interactions with radiation belt electrons. Examples of whistler mode waves recorded on the Dynamics Explorer-1 (DE-1) satellite are shown in Figure 1.5.

### 1.1.1. Radiation Belts

In addition to the cold plasma, the inner magnetosphere is also populated by suprathermal (tens to hundreds of eV) and energetic (few keV to tens of MeV) electrons and ions, which are trapped by the Earth's magnetic field and which constitute the *radiation belts* [Hess, 1968; Roederer, 1970; Akasofu and Chapman, 1972]. These particles execute helical motions around the magnetic field lines, reflect back and forth between the two mirror points in opposite hemispheres and drift around the Earth due to magnetic field gradient and curvature drifts [Roederer, 1970]. Trapping of the particles by the Earth's magnetic field constrains their motion so that the complete trajectory of a given particle along a given magnetic field line can be defined by only two parameters, for example by  $v_{z_{eq}}$  and  $\alpha_{eq}$  (equatorial velocity in the direction of the magnetic field and equatorial pitch angle respectively, where pitch angle is the angle between the particle's velocity vector and the magnetic field), as illustrated in Figure 1.6. Along a given magnetic field line, the mirror points are determined uniquely by the equatorial pitch angle; they are independent of the particle's total velocity (i.e., energy). The scattering of the particles by external forces (such as those due to resonant whistler-mode waves) may lead to changes in their equatorial pitch angle and displacement of their corresponding mirror points along the field line. If its mirror point is lowered into the increasingly denser atmosphere the particle interacts with the atmospheric constituents and can be lost from the radiation belts and be

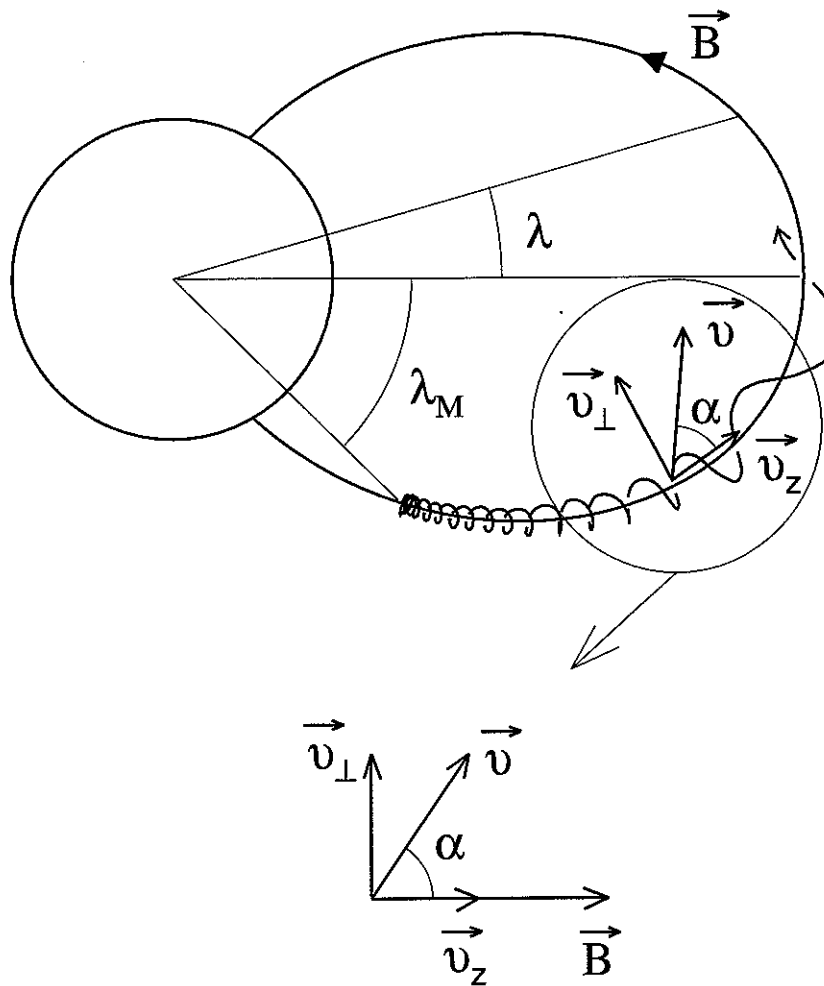


**Figure 1.6. The trajectory of a radiation belt electron.** Radiation belt particles (electrons and ions) execute complex helical motions consisting of a gyration around the magnetic field line, reflection between the two mirror points along the field line, and drift around the Earth across the magnetic field lines. The particle's trajectory and mirror points ( $\lambda_M$ ) are defined by only two parameters, for example by equatorial velocity in the magnetic field direction,  $v_z(\lambda = 0^\circ)$ , and equatorial pitch angle,  $\alpha(\lambda = 0^\circ)$ .

'precipitated' into the atmosphere. The critical equatorial pitch angle which corresponds to the mirror point defined with respect to an 'effective' upper atmospheric boundary is called the *loss cone angle*. All particles that have equatorial pitch angles smaller than the loss cone angle mirror below this boundary and are therefore considered to be lost from the radiation belts. The

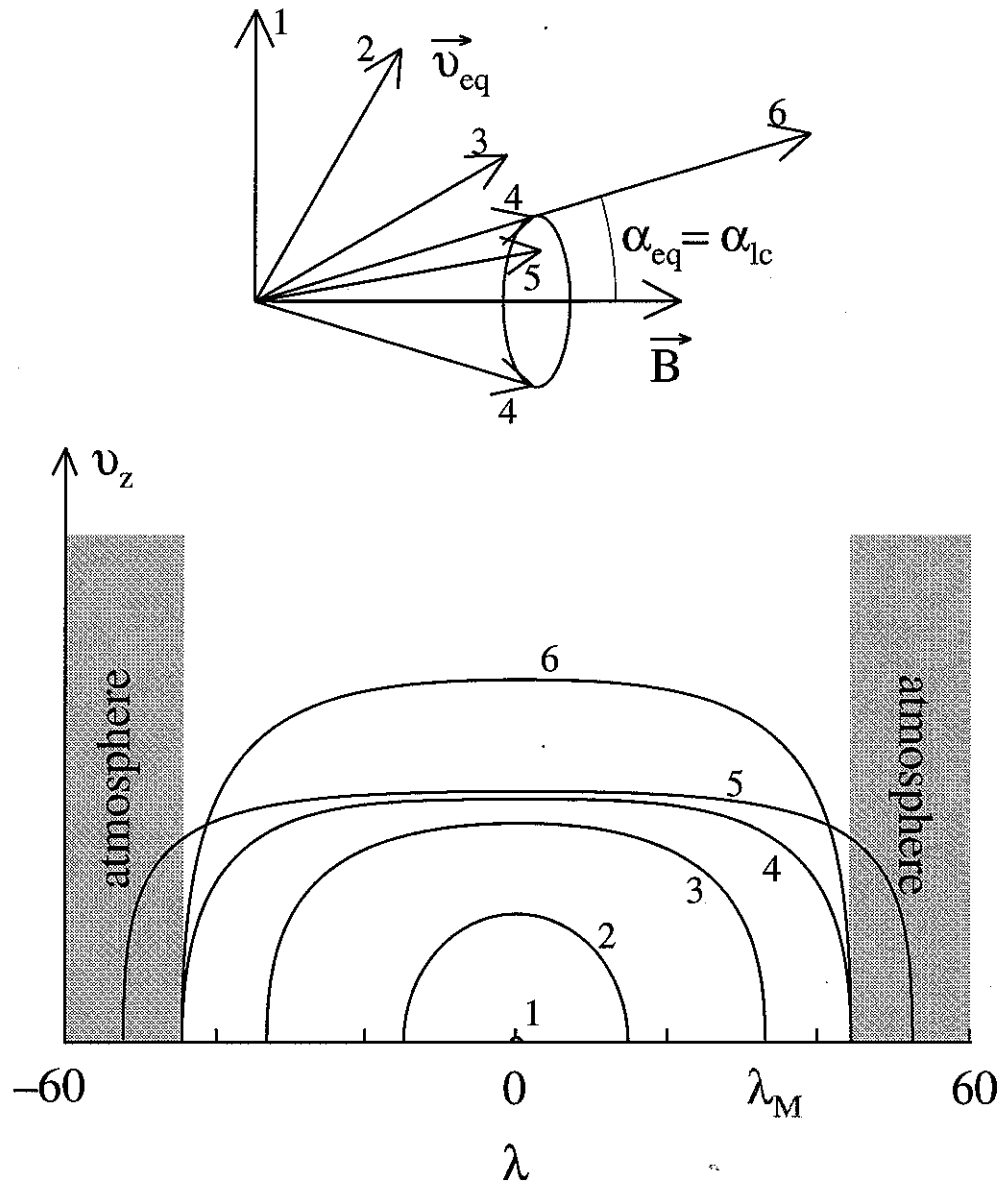


**Figure 1.7. Dependence of electron trajectories on the equatorial pitch angle.** Electron trajectories plotted in the lower panel as  $v_z(\lambda)$  correspond to the equatorial velocity vectors shown in the upper panel. Mirror points do not depend on the magnitude of the particle's velocity; they depend only on the pitch angle. Particles with equatorial pitch angles less than the loss cone angle interact with the atmosphere and are precipitated.

concepts of loss cone, mirror point and the variation of the particle velocity with latitude along a field line are illustrated in Figure 1.7.

The determination of the loss rates of radiation belt electrons as well as the quantitative evaluation of the contributions to this loss of different mechanisms are important both in terms of our understanding of the dynamics of the radiation belts and also because the precipitated energetic particles cause significant disturbances in the upper atmosphere such as heating, ionization, conductivity enhancements, emission of light and X-rays [Rees, 1989]. Although not fully understood, the source and loss processes of radiation belt particles are in a dynamical equilibrium. The solar wind is believed to be one source of energetic particles which enter the magnetosphere through the cusp or magnetotail and drift across the magnetic field lines to form the radiation belts via radial diffusion. Since the boundary between the atmosphere and the magnetosphere is gradual rather than abrupt, physical and chemical processes in the intermediate region, the ionosphere, are also important as sources and losses of radiation belt particles [Walt *et al.*, 1968].

### 1.1.2. Cyclotron resonance

An important loss process for radiation belt particles are resonant wave-particle interactions. During these interactions, wave fields perturb the adiabatic motion of the particle (by primarily changing its pitch angle but also modifying its energy), resulting in lowering of the mirror altitude below the atmospheric boundary and leading to the particle's loss from the radiation belts. Resonance between a particle and a wave is considered to occur when, for some period of time, the particle experiences a relatively slow variation in the phase of the wave's electric and magnetic fields. The Landau (longitudinal) and cyclotron (gyro) resonance are two forms of resonant interactions that are common for whistler-mode waves in the magnetosphere. Landau resonance occurs when the components of the particle's velocity and wave phase velocity in the direction of ambient magnetic field are approximately equal. Cyclotron resonance (gyroresonance) occurs when the Doppler-shifted wave frequency, as observed in the particle's frame of reference, is approximately equal to the particle's gyrofrequency. The geometry of cyclotron resonance between gyrating electrons and elliptically



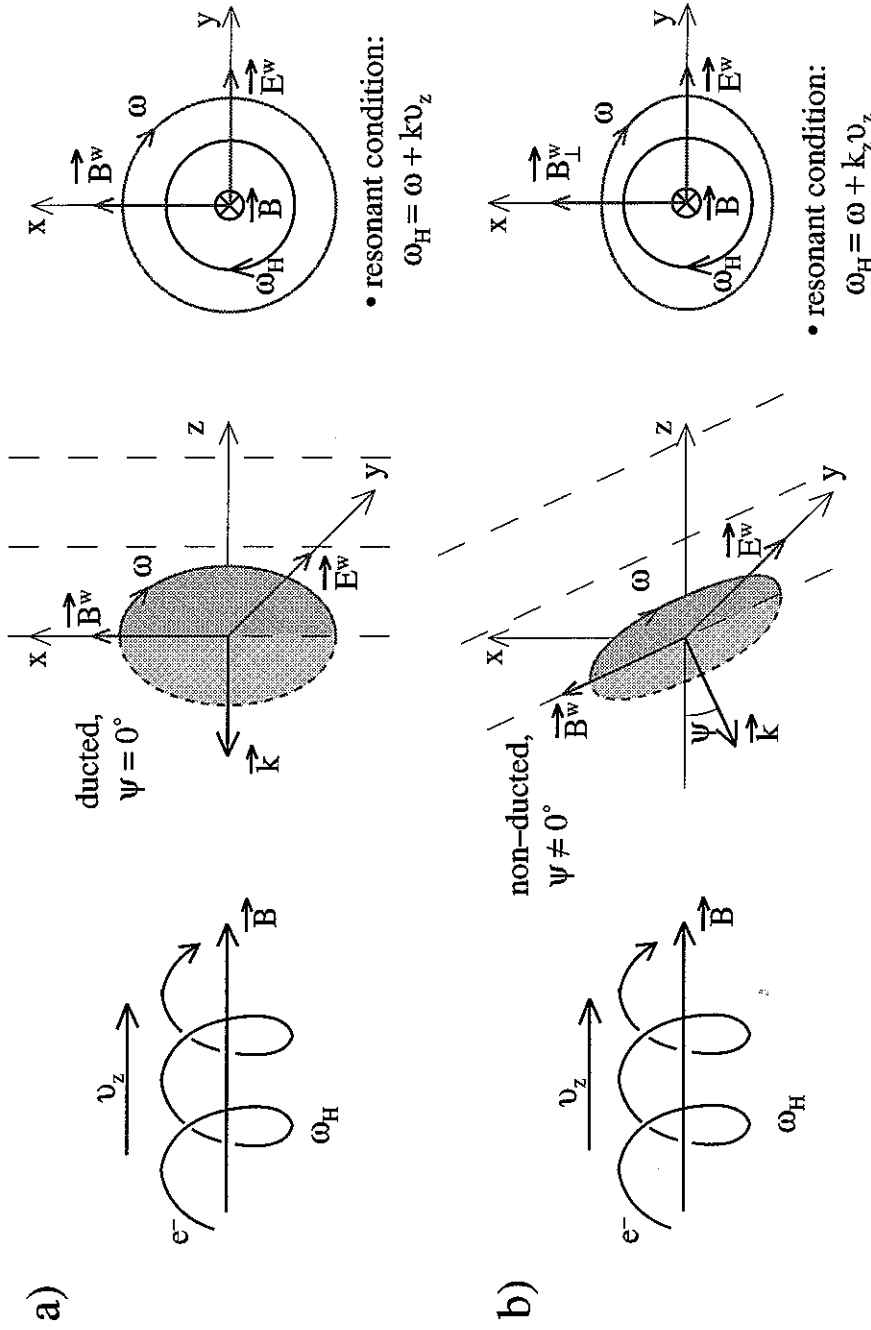


**Figure 1.8. Electron-wave cyclotron resonance.** Cyclotron resonant interactions between gyrating electrons and right hand elliptically polarized waves are schematically shown and resonant conditions given for interactions involving a) a ducted ( $\psi=0^\circ$ ), circularly polarized wave and b) an oblique ( $\psi>0^\circ$ ), elliptically polarized wave.

polarized components of both ducted and non-ducted whistler mode waves are schematically illustrated in Figure 1.8. The electrons rotate in the same direction as the electric and magnetic fields of the right hand elliptically polarized waves (in general an oblique whistler-mode wave is elliptically polarized, but for the special case of ducted waves ( $\psi=0^\circ$ ) the polarization is circular). If the rate of rotation of the electron and wave are matched, the wave fields appear to have stationary phase in the reference frame of the electron. For the same electric and magnetic field intensities the electron-wave interaction is more effective for the case of a circularly polarized (ducted) wave than for an elliptically polarized (non-ducted) wave. However, we should note that the wave polarization as well as the ratio of electric and magnetic field intensities are determined by the propagation medium and also depend on the wave normal angle  $\psi$  in a complex manner, as shown later (Chapter 3).

## 1.2. Review of Previous Work

Past investigations of resonant whistler-mode wave-particle interactions have recognized their importance in the loss of radiation belt electrons [e.g., *Dungey*, 1963] and have evolved in essentially two directions depending on the coherence of the wave. When interacting with broadband and incoherent whistler mode waves through cyclotron resonance, individual particles are subjected to a series of random pitch angle scatterings so that for a population of particles the interaction can be viewed as a diffusion process. The cyclotron resonant interaction of a distribution of particles with an incoherent whistler mode wave can thus be studied via diffusion coefficients formulated in the particle's equatorial pitch angle space [*Roberts*, 1966]. This approach was used by *Kennel and Petschek* [1966], *Lyons et al.* [1972], *Lyons and Thorne* [1973], *Spjeldvik and Thorne* [1975] and others to study interactions of

radiation belt particles with a class of incoherent magnetospheric signals known as plasmaspheric hiss. Note that past studies based on the diffusion coefficient approach have included interactions between radiation belt electrons and oblique whistler mode waves [Roberts, 1969; Lyons *et al.*, 1971].

The physics of particle-wave interactions for the case of coherent and narrowband whistler mode waves is fundamentally different. During the interaction with a coherent wave individual particles are not scattered randomly; instead, they stay in resonance with the wave long enough for the particle's pitch angle to be substantially changed. This non-linear interaction has been extensively studied for ducted whistlers by the means of a test particle simulation model [Inan, 1977; Inan *et al.*, 1978; Inan *et al.*, 1982; Chang, 1983; Chang and Inan, 1983a; Chang and Inan, 1983b; Chang *et al.*, 1983] including direct comparisons with experimental data [Inan *et al.*, 1985a; 1989]. A good review of this approach and a comparison between interactions with coherent versus incoherent waves is given by Inan [1987].

Experimental observations have shown that ionospheric effects of precipitated electrons, such as sub-ionospheric VLF perturbations, X-ray emissions, or photoemissions can often be correlated with natural ducted VLF waves (whistlers, chorus emissions, noise bursts, etc.) [Rosenberg *et al.*, 1971; Helliwell *et al.*, 1973; Foster and Rosenberg, 1976; Lohrey and Kaiser, 1979; Helliwell *et al.*, 1980; Mende *et al.*, 1980; Rosenberg *et al.*, 1981; Dingle and Carpenter, 1981; Carpenter and LaBelle, 1982]. In particular, the ionospheric signatures of the scattering of energetic electrons out of the radiation belts in cyclotron resonant interactions with lightning-generated ducted (i.e., parallel propagating) whistlers have been both theoretically studied in detail [e.g. Chang and Inan, 1985] and are now commonly observed [Inan *et al.*, 1990; Burgess and Inan, 1990, and references therein]. As a measure of the effectiveness of this interaction, precipitated energetic electron fluxes have been theoretically estimated and compared with experimental data [Inan *et al.*, 1985b; Inan and Carpenter, 1987; Inan *et al.*, 1989].

However, the bulk of the wave energy injected into the magnetosphere by lightning discharges propagates in the non-ducted mode. Although non-ducted waves may be less efficient than ducted waves in pitch angle scattering and precipitation of electrons in a single encounter cyclotron resonant interaction (due to elliptical polarization of non-ducted waves versus circular polarization of ducted waves, as described in Figure 1.8.), their overall effect on radiation belt electron precipitation is yet to be ascertained. Quantitative consideration of the interactions between non-ducted whistler-mode waves and radiation belt electrons is the subject of this thesis, in which we provide a first estimate of the effectiveness of non-ducted whistlers in precipitating particles.

In this thesis we consider resonant particle interactions with coherent, monochromatic whistler mode waves propagating obliquely with respect to the ambient magnetic field. Further, we only consider the resultant modification of the electron distribution in a single encounter with the wave. Such a 'one-pass' solution essentially integrates over temporal variations that would occur as the wave packet propagates along the field line and interacts with particles of different energy at different locations [*Inan et al.*, 1982]. When applying our model to the Earth's magnetosphere, the first assumption of the coherence of the wave is justified since both signals from VLF transmitters and lightning generated whistler mode waves are narrow-band and coherent (see section 5.4). However, natural whistlers launched by lightning discharges exhibit slowly varying frequencies (Figure 1.5) and are discrete finite duration wave packets; both of these features are not included in our present model. In this sense, our model results are more directly representative of the effects of each Fourier component of lightning generated whistlers or signals which are monochromatic (e.g., VLF transmitter signals) and constitute the first step in a more general model that might also be applicable for slowly varying frequencies and discrete wave packets.

### **1.3. Contributions of the Present Work**

The main contributions of this Ph.D. dissertation can be listed as follows:

**1) Development of a test particle simulation model of resonant interactions between oblique whistler waves and charged particles.** The first step in this development was to extend the existing formulation of test particle equations of motion to include relativistic particles. The first part of the computer model is the simulation of the test particle trajectories. In the second part, the individual test particle simulation results are combined with the initial particle distribution function to infer the changes in the full distribution function. Results are expressed in terms of measurable quantities such as precipitated differential energy flux, total precipitated energy flux and particle lifetimes.

One important feature of this model is its generality. With minor modifications, the model can be used to study interactions occurring in different media (magnetic field, background plasma density) such as at other magnetized planets, interactions involving protons and other ions or other types of resonant interactions (e.g., Landau resonance, higher order gyroresonance). The model provides a good basis for future development of the test particle simulation method (see suggestions for future work in Chapter 7.)

**2) Application of the model to the parameters of the inner magnetosphere ( $L \leq 4$ ) revealed that oblique wave energy injected into the magnetosphere by thunderstorms or transmitters may substantially contribute to the establishment of radiation belt equilibrium as well as cause significant perturbations (secondary ionization, light emission) in the ionosphere via particle precipitation.**

3) In particular, we show, for the first time, that oblique whistlers can efficiently scatter significant energy fluxes of suprathermal (10–100 eV) electrons. Suprathermal  $E=100$  eV electron energy fluxes are calculated to be  $\sim 6$  times higher than those of energetic  $E=100$  keV electrons precipitated by ducted whistlers whose peak values are measured to be of the order of  $10^{-3}$ – $10^{-2}$  erg/cm<sup>2</sup>-s. It is estimated that suprathermal electrons precipitated by oblique whistlers can cause secondary ionization of  $\sim 30$ – $40$  ion pairs/cm<sup>3</sup>-s at relatively high altitudes of 300–400 km.

4) We have shown that **MR whistlers originating in lightning can resonantly interact with radiation belt electrons over a broad range of  $L$ -shells and precipitate higher energy electrons from lower  $L$ -shells.** Electrons in the energy range of 1–2.6 MeV are precipitated from  $L = 2$ , whereas from  $L = 4$  the precipitated electron energy range is 150–220 keV. The precipitated differential electron flux, due to this interaction, is higher for higher  $L$ -shells, and the maximum value ranges from  $\Phi_{E_{prec}}(1.11 \text{ MeV}) = 5.2 \times 10^{-4}$  el/cm<sup>2</sup>-s-keV at  $L = 2$  to  $\Phi_{E_{prec}}(173 \text{ keV}) = 4.6 \times 10^{-1}$  el/cm<sup>2</sup>-s-keV at  $L = 4$ . **The lifetimes of radiation belt electrons in a given magnetic flux tube around the  $L$ -shell on which the interaction takes place are found to be of the order of several days, comparable to lifetimes corresponding to electron loss induced by hiss, which was heretofore assumed to be the dominant loss mechanism [Lyons *et al.*, 1972].** The minimum electron lifetimes vary from 2.47 days for  $E = 1.11$  MeV electrons at  $L = 2$  to 4.64 days for  $E = 173$  keV electrons at  $L = 4$ .

## 2.

# **Preliminary Assessment of the Efficiency of Cyclotron Resonant Interactions Between Electrons and Oblique Whistlers**

In this chapter, we describe results of our preliminary evaluation of the possible role of oblique whistler mode waves in the scattering of radiation belt electrons via cyclotron resonant interactions. Part of the results reported in this chapter were published in Geophysical Research Letters [*Jasna et al.*, 1990]. Specifically, we consider (i) the equatorial gyroresonance conditions as dictated by the propagation of VLF waves along a raypath in a model magnetosphere and (ii) the equatorial pitch angle scattering coefficients. For the first part of our study the Stanford two-dimensional raytracing code was used to determine the parameters of near-loss-cone electrons that would undergo cyclotron resonance with the oblique whistler mode waves, the characteristics of which are determined via raytracing [*Jasna et al.*, 1990].

In the second part of our preliminary work we consider the radiation belt electron pitch angle diffusion coefficients based on pitch angle changes averaged over one electron gyroperiod. For this purpose, we consider the interaction between near-loss-cone electrons and narrow band oblique whistler mode waves and evaluate the diffusion coefficients as a measure of the effectiveness of electron scattering. Scatterings by ducted and non-ducted

waves are compared, based on the dependence of the magnitude of the diffusion coefficient on wave normal angle.

The combined results of the two preliminary analyses indicate that cyclotron resonant interactions between electrons and oblique whistler mode waves can potentially be an important mechanism of radiation belt electron loss and that this type of interaction needs to be studied in more detail.

## 2.1. Equatorial Gyroresonance With the Raytraced Whistlers

A large fraction of the wave energy injected into the magnetosphere by lightning discharges propagates in the non-ducted (oblique) mode and is often found to undergo multiple (up to 8–10 bounces) reflections back and

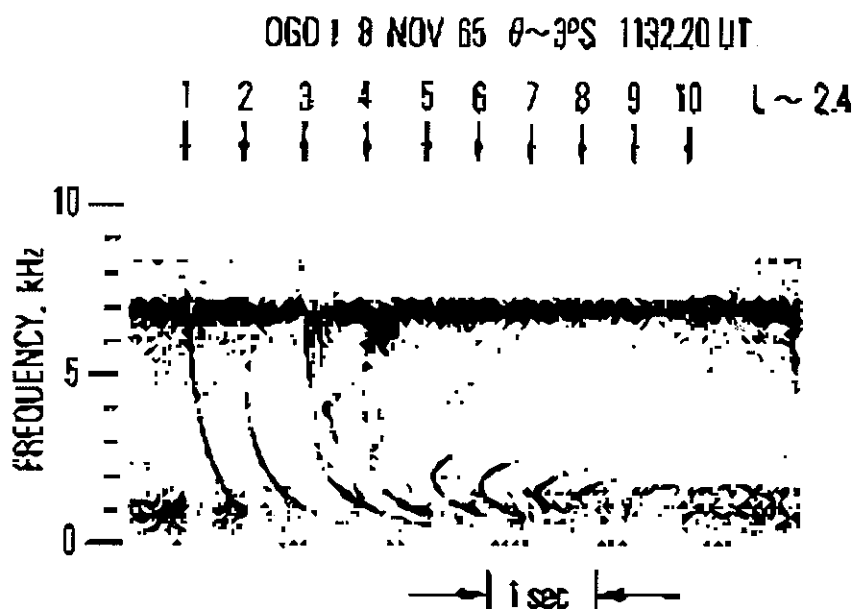


**Figure 2.1. Example of an MR whistler.** Frequency-time spectrogram of an MR whistler with 10 components and with well defined upper- and lower-frequency cutoff patterns. Taken from *Edgar* [1976].



forth between hemispheres [Edgar, 1976]. The reflections typically occur at locations where the wave frequency matches the local lower hybrid resonance frequency, leading to the so-called Magnetospherically Reflected (MR) whistlers as observed on spacecraft (Figure 2.1.).

Little attention has been paid so far to the interaction of MR whistlers with energetic particles and their contribution to the loss of these particles from the radiation belts. Recent satellite- and ground-based data indicate that whistlers originating in lightning discharges regularly precipitate energetic electrons out of their trapped orbits [Voss *et al.*, 1984, Inan *et al.*, 1988]. While individual events are commonly associated with ducted whistlers [Inan and Carpenter, 1986, Burgess and Inan, 1992] and/or lightning discharges [Inan *et al.*, 1988], the relative role of non-ducted whistlers is not known. In this section, we investigate energies of the electrons that would undergo cyclotron resonance with MR whistlers near the geomagnetic equator during multiple crossings (Figure 2.2.). We find that the resonant energy for electrons remains roughly constant as the equatorial crossings for typical rays move inward over the range  $1.5 < L < 4$ . This result indicates that wave energy entering the magnetosphere from a single location can resonantly interact with electrons of the same energy over such a wide range of  $L$ -shells. Thus, VLF wave energy produced by lightning may play an important part in the precipitation of energetic electrons on magnetic field lines far removed from that of the lightning discharges.

### 2.1.1. Method of Calculation

The basis for theoretical calculations to determine the wave normal angle and refractive index was the Stanford VLF Raytracing program [Burtis, 1974; Inan and Bell, 1977]. Rays at selected frequencies in the range of 1–32 kHz were injected into the magnetosphere at 1000 km altitude and at  $L = 1.5 - 4$ , and the output parameters of  $\psi$ ,  $\omega/\omega_H$ ,  $n \cos \psi$  at each step along the ray path were computed, where  $\psi$  is the wave normal angle (the angle between the wave vector and Earth's magnetic field),  $\omega$  is the wave frequency,  $\omega_H$

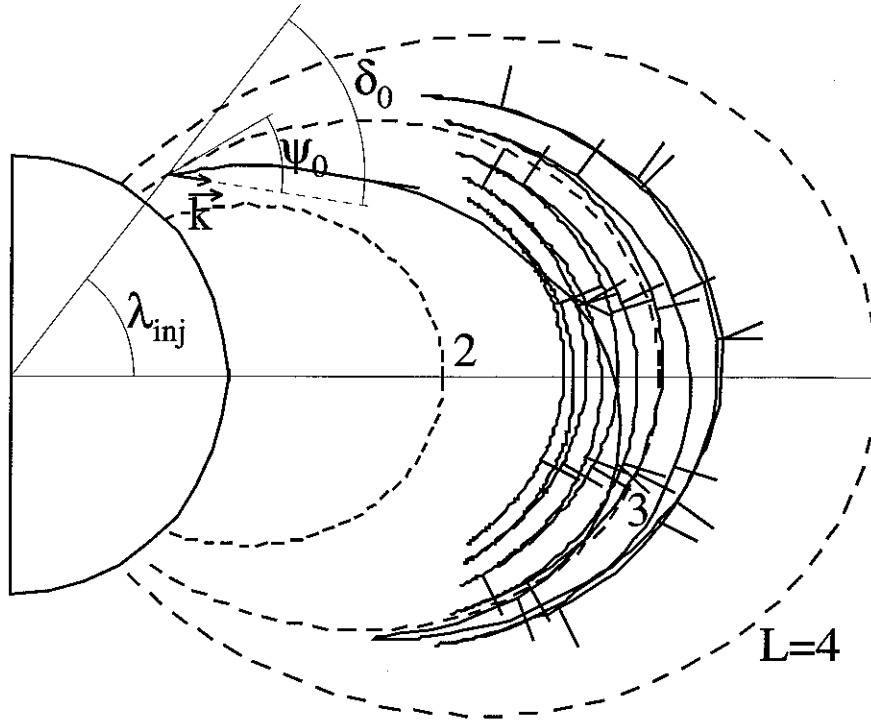


**Figure 2.2. Sample raypath.** Schematic illustration of a sample raypath in a magnetic meridional plane for a  $f = 2$  kHz wave injected at 1000 km altitude at  $L = 3$ . The wave normal direction is shown at intervals along the raypath as a short line segment, and its angle with respect to the magnetic field line and the upward vertical are defined at the point of injection as  $\psi_0$  and  $\delta_0$  respectively.

is the electron gyrofrequency and  $n$  is the refractive index. Typical plasmaspheric conditions as represented by the equatorial electron density profile shown in Figure 2.3. were assumed. A sample raypath is shown in Figure 2.2. to establish the coordinate system for all the calculations.

For oblique whistler waves, an important characterizing parameter is the difference between the wave normal angle ( $\psi$ ) and the resonance cone angle ( $\psi_r$ ), i.e.,  $Y = |\psi - \psi_r|$ . The quasi-electrostatic versus electromagnetic nature of the wave as well as the pitch angle scattering coefficient for electrons in transverse resonance with an oblique whistler depend strongly on this parameter [Inan and Bell, 1991]. Dependence of  $Y$  on  $L$ -shell along the raypath is given in Jasna *et al.* [1990].

With  $\psi$  and the refractive index ( $n$ ) obtained from the raytracing program, the relativistic resonant electron energy for electrons in the vicinity of the loss cone (pitch angle  $\alpha = \alpha_{lc}$ ) was computed from

$$E = m_o c^2 (\gamma - 1) ; \quad v_z \equiv \frac{c}{\omega n \cos \psi} (\omega_H \gamma^{-1} - \omega)$$

where  $\gamma^{-1} = \sqrt{1 - \beta^2}$ , with  $\beta = (v/c) = (v_z/c)(\cos \alpha_{lc})^{-1}$ ,  $v$  is the magnitude of the electron velocity and  $v_z$  is the electron velocity in the direction of the magnetic field.

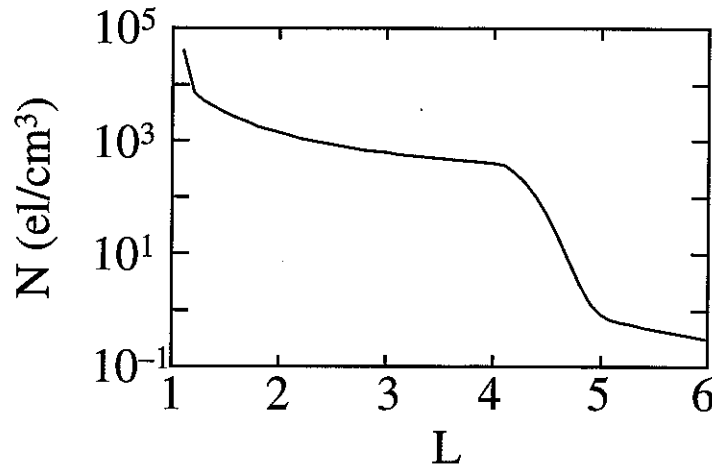


**Figure 2.3. Equatorial electron density profile.** The variation of the density along the field line is assumed to follow a diffusive equilibrium model [e.g., see *Inan and Bell, 1977*]. The equatorial electron density values were assumed to be as shown.

### 2.1.2. Results

In this section, we first illustrate the parameter variations along the raypath and then concentrate on the resonant interactions near the geomagnetic equator. While oblique resonance can occur with electrons encountered anywhere along the raypath, for typical rays the longest and most effective gyroresonance is expected to occur close to the equatorial plane, where the

variations in  $\omega_H$ , wave vector ( $k$ ) and  $\psi$  along the field line (in the frame of the particles) are the slowest [Bell, 1986].

The equatorial plane crossings of different rays are investigated in terms of the value of resonant electron energy  $E$  (i.e.  $E_{eq}$ ) and its dependence on  $L$  along the raypath. We consider waves in the frequency range 1–32 kHz, injected at a 1000 km altitude along the field lines in the  $L = 1.5 - 4$  latitude range and with the initial wave-normal directions at the injection point of  $\psi_0 = -80^\circ$  to  $+80^\circ$ .

### *Parameter variations along the raypath*

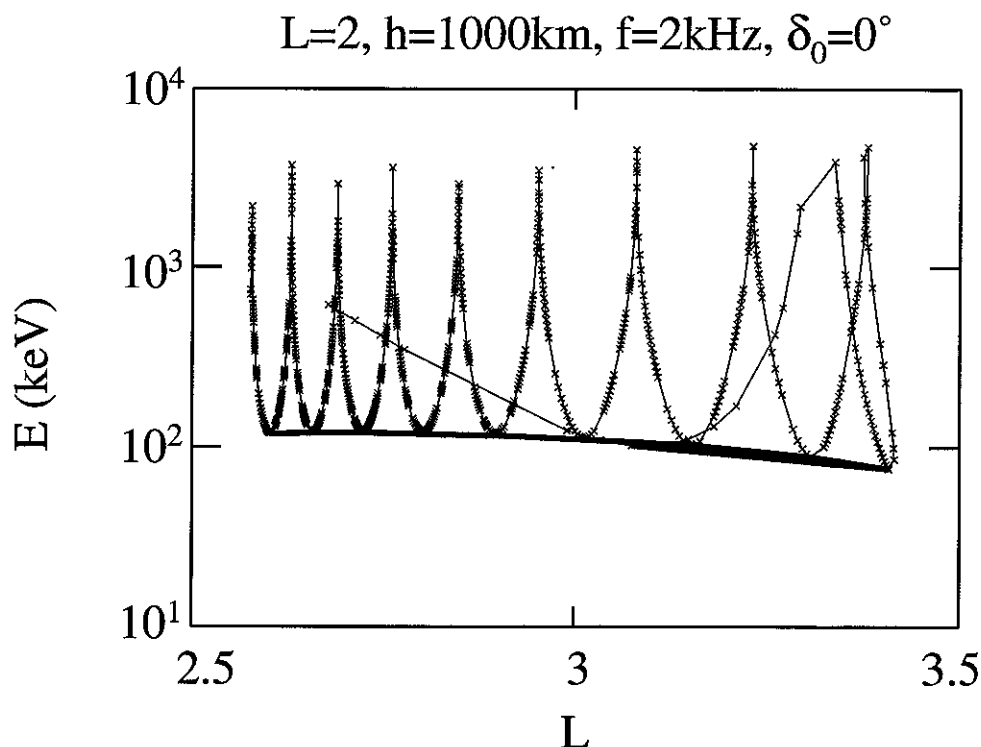
A typical raypath for an MR whistler is shown in Figure 2.2. Initially the ray moves toward higher  $L$ -shells, but after one complete bounce it begins to move toward lower  $L$  values. The ray moves inward (toward lower  $L$ -shells) if, at the magnetic equator, its frequency is higher than the local lower hybrid resonance frequency ( $f > f_{LHR}$ ) [Edgar, 1976]. On the other hand, if  $f < f_{LHR}$  at the magnetic equator, the ray moves outward, so the surface  $f_{LHR} = \text{const.}$  is a 'strange' attractor for all rays with  $f = f_{LHR}$ .

Figure 2.4. shows  $E$  for a single selected ray at 2 kHz injected at  $L = 2$ , vertically upwards. The '+'s represent points along the raypath at regular intervals and are connected by a thin line. The thick curve connects just the equatorial crossings ( $E_{eq}$ ). The variation of  $E_{eq}$  as a function of frequency is shown in Figure 2.5.

The resonant electron energy oscillates between lower and upper limits, represented respectively by the energy curve associated with the equatorial crossings and by  $E = m_o c^2 (\omega_H / \omega - 1)$  (at the reflection points where  $k_z \rightarrow 0$ ). Our values are somewhat lower than the upper limit due to the use of a discrete set of output values.

Assuming that significant interactions can occur all along the ray path, the results shown in Figure 2.4 indicate that wave energy at 2 kHz entering the

magnetosphere at a fixed location (e.g.,  $L = 2$ ) can resonantly interact with electrons in the 100–1000 keV range as it bounces back and forth between hemispheres.



**Figure 2.4. Resonant electron energy along the raypath.** The variation of resonant energy  $E$  along a sample raypath shown as a function of  $L$ -shell for a  $f = 2$  kHz ray injected vertically upward ( $\delta_0 = 0^\circ$ ) at  $L = 2$ . The parameter values at sample points are connected with a thin solid line in the order of their appearance along the ray propagation path. The thick curve connects the equatorial crossings.

### *Dependence on injection latitude*

The dependence of  $E_{eq}$  on injection latitude ( $L$ -shell) is shown in Figure 2.5. The rays injected at the lower latitudes ( $L = 1.5$  and  $2$ ) do not encounter the plasmapause (at  $L = 4$ ) and exhibit relatively well defined features. The raypaths initially move towards higher  $L$ -shells and then gradually descend toward lower  $L$ -shells. Frequency dependence is such that raypaths for higher

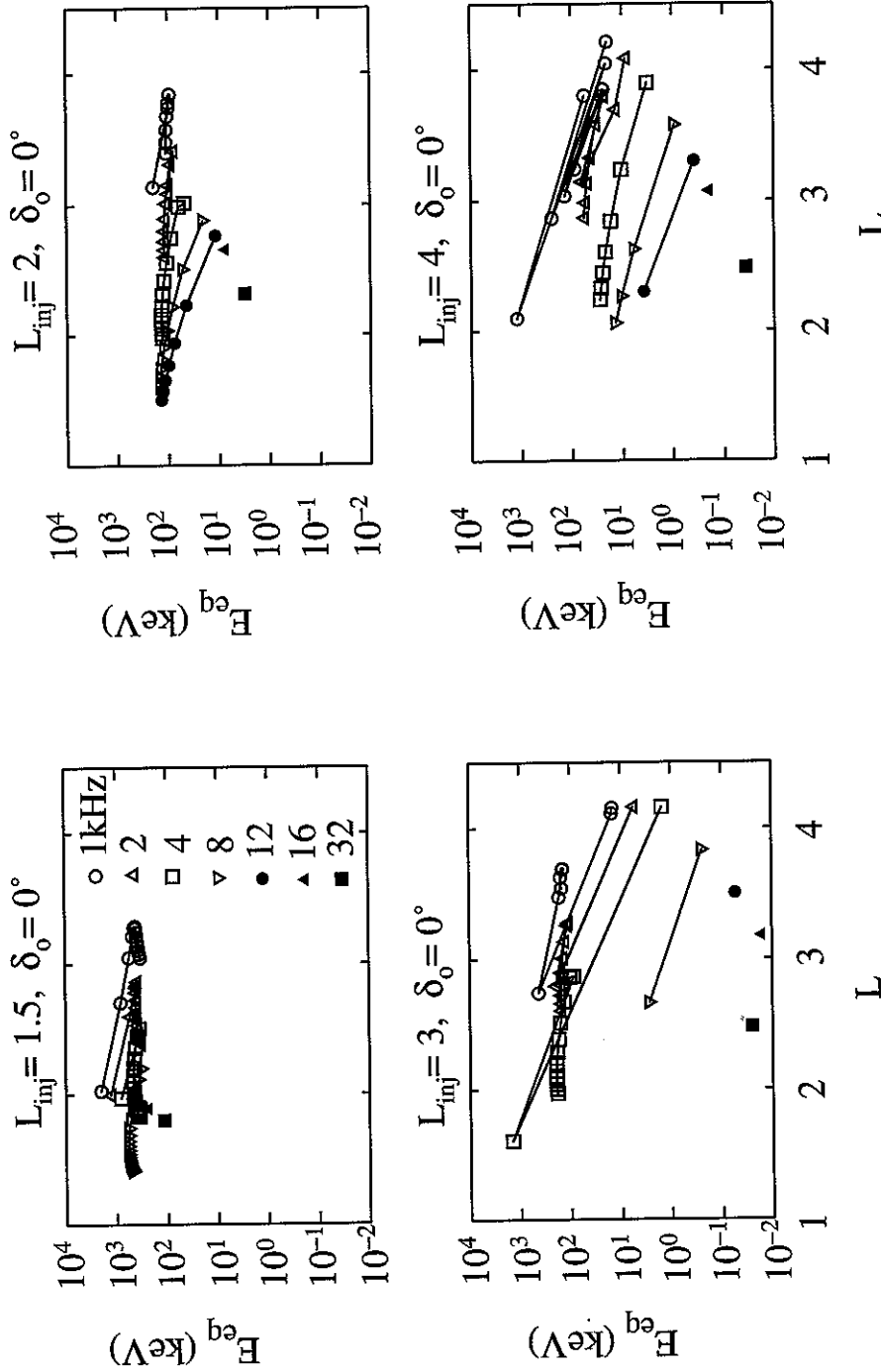
frequency rays are shifted towards lower  $L$ -shells. We note that for wave frequencies of 16 and 32 kHz there is only one equatorial crossing since the lower hybrid resonance frequency ( $f_{LHR}$ ) is always less than the wave frequency ( $f$ ), and magnetospheric reflection does not occur. For 12 kHz, whether or not reflection occurs depends on the disposition of the raypath; for example the 12 kHz ray injected at  $L = 1.5$  arrives at the other hemisphere at latitudes where  $f_{LHR} < f$  and does not undergo MR reflection, whereas that injected at  $L = 2$  does.

The variation of the equatorial resonant energy ( $E_{eq}$ ) shows that this quantity is relatively independent of frequency, especially after the first few equatorial crossings. For example, for injection at  $L = 2$  with  $f = 2$  kHz, the equatorial resonant electron energy is in the range  $78 \text{ keV} < E_{eq} < 122 \text{ keV}$  while for all other frequencies injected at  $L = 2$  we have  $78 \text{ keV} < E_{eq} < 148 \text{ keV}$ . Furthermore we note that this resonant energy range is not a very strong function of injection latitude ( $L$ ). For injection at  $L = 1.5$  the energy range is  $319 \text{ keV} < E_{eq} < 579 \text{ keV}$ , and for  $L = 3$  it is  $85 \text{ keV} < E_{eq} < 191 \text{ keV}$ .

The rays injected at the higher latitudes ( $L = 3$  and 4) initially move towards the plasmapause and in that region exhibit irregular behavior. After they reflect from the plasmapause and propagate inward, well defined features explained earlier are exhibited. Raytracing with a plasmapause located at higher  $L$ -shells (e.g.,  $L = 7$ ) shows that rays injected at  $L = 3$  also exhibit well defined behavior. Rays injected at higher latitudes inevitably encounter the plasmapause and exhibit irregular behavior, although this also depends on the wave normal at the point of entry. The general effect of the plasmapause is thus well illustrated in Figure 2.5.

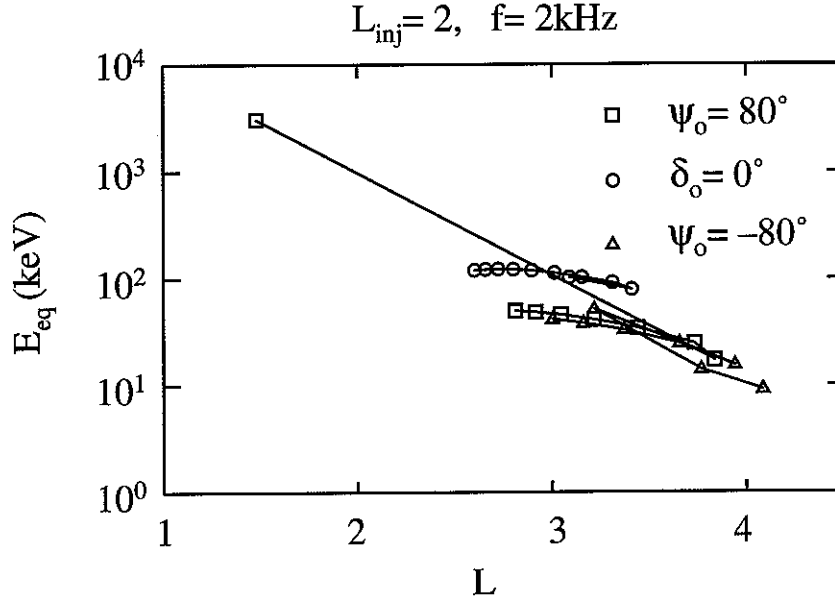
#### *Dependence on wave normal angle at injection*

Figure 2.6 shows the dependence of  $E_{eq}$  on  $\psi_0$  for 2 kHz rays injected at 1000 km altitude at  $L = 2$ . Similar results are also found for other frequencies and injection latitudes.



**Figure 2.5. Equatorial resonant electron energy dependence on the ray parameters. Dependence on injection latitude and wave frequency of the equatorial resonant energy of electrons,  $E_{eq}$ , for rays injected vertically upward ( $\delta_0 = 0^\circ$ ) from  $L = 1.5, 2, 3, 4$ , with frequencies  $f = 1, 2, 4, 8, 12, 16, 32$  kHz that are denoted by different symbols. Each point represents the equatorial plane crossing of a single ray and for each frequency the successive crossings are connected. The  $L$ -shell at which the rays were injected is given at the top of the each panel.**

The general behavior of  $E_{eq}$  from Figure 2.6 is fairly independent of  $\psi_0$ . The ray with  $\psi_0 = +80^\circ$  tends to propagate on lower  $L$ -shells, is far away from the plasmapause, and therefore exhibits well defined characteristics similar to the vertically injected ( $\delta_0 = 0^\circ$ ) case. The ray with  $\psi_0 = -80^\circ$  initially moves toward the plasmapause and exhibits irregular behavior until it moves to lower  $L$ -shells in a manner similar to the case of vertical injection at higher  $L$ -shells. After the fourth equatorial crossing the  $E_{eq}$  for this ray varies in the same way as that for  $\psi_0 = +80^\circ$  and is shifted somewhat towards higher  $L$ -shells compared to the  $\delta_0 = 0^\circ$  case. Figure 2.6 shows that although the equatorial resonant electron energy level is higher for  $\delta_0 = 0^\circ$ , dependence of  $E_{eq}$  on  $\psi_0$  is rather weak.



**Figure 2.6. The dependence of equatorial resonant electron energy on the wave normal angle at the injection point.** Dependence on the wave normal angle at the point of injection of the equatorial resonant energy  $E_{eq}$ , versus  $L$ -shell value for rays injected at  $L = 2$  with frequency  $f = 2$  kHz in three directions  $\psi_0 = +80^\circ$ ,  $\delta_0 = 0^\circ$ ,  $\psi_0 = -80^\circ$ , represented respectively with a square, a circle and a triangle.



### 2.1.3. Conclusions

Whistlers originating in lightning discharges, while they bounce back and forth between hemispheres due to magnetospheric reflections, undergo gyroresonance with electrons in well defined energy ranges near the geomagnetic equator. As the wave reflects back and forth, the equatorial resonant electron energy ( $E_{eq}$ ) remains roughly constant even though the raypaths move inward with the equatorial crossing varying over a wide range of  $L$ -shells ( $1.5 < L < 4$ ). Typical  $E_{eq}$  are of the order of 100 keV, depending on the point of entry of the whistler into the magnetosphere. For example, for whistlers entering the medium at  $L = 2$ , equatorial electron resonant energy remains in the range  $78 \text{ keV} < E_{eq} < 148 \text{ keV}$ .

It thus appears that MR whistlers originating from a single location, initiated, for example, by isolated thunderstorm centers, could resonantly interact with and induce precipitation of electrons in relatively small energy ranges over a wide range of  $L$ -shells. The importance of this effect in terms of the loss of the particles from the radiation belts needs to be evaluated. However, we can expect the contribution of MR whistlers to this loss to be substantial, since pitch angle diffusion coefficients for oblique wave-particle interactions have been shown to be comparable to that for  $\psi = 0^\circ$  [Inan and Bell, 1991].

## 2.2 Gyro-averaged Pitch Angle Diffusion

In this subsection we evaluate pitch angle diffusion coefficients to quantitatively assess the magnitude of electron scattering by oblique whistler mode waves and to compare results with scattering due to interactions with ducted whistler mode waves. We note here that a diffusion formulation is only appropriate for interactions involving incoherent waves [Inan, 1987] so

that, for the case of interactions with coherent signals (such as whistlers from lightning or VLF transmitter signals), the magnitude of scattering as evaluated in this section only constitutes a first approximation. Our results indicate that the pitch angle scattering resulting from interactions with non-ducted waves are at least as large as those due to interactions with ducted waves.

### 2.2.1. Gyro-averaged Diffusion Coefficient

A given radiation belt electron is considered to be in resonance with a narrow band oblique whistler mode wave if  $v_z \cong v_R = (\gamma^{-1} \omega_H - \omega) k_z^{-1}$ , where  $v_z$  is the component of the particle velocity  $\vec{v}$  along  $\vec{B}_0$ ,  $\gamma^{-1} = \sqrt{1 - (v/c)^2}$ ,  $k_z = (\omega/c)n \cos \psi$  is the component of the wave vector along the magnetic field line,  $\omega_H$  is the electron gyrofrequency,  $\omega$  is the wave frequency,  $n$  is the refractive index and  $\psi$  is the wave normal angle with respect to the magnetic field line. The pitch angle diffusion coefficient,  $D_\alpha$ , is defined as  $D_\alpha = \overline{(\Delta\alpha)^2} / \Delta t$  [e.g., *Kennel and Petschek*, 1966; *Roberts*, 1968], where  $\Delta t = (2\pi)^{-1} \Delta\omega (1 + v_R/v_{gz})$  is the average time particles stay in resonance,  $\Delta\omega$  is the wave bandwidth,  $v_{gz} = (\partial\omega/\partial k_z)$  is the component of the wave group velocity along  $\vec{B}_0$ ,  $\Delta\alpha$  is determined by the equations of motion [*Bell*, 1986], and the bar represents averaging over the particle ensemble, assuming uniform distribution in initial gyrophase. The rate of change of pitch angle for resonant electrons averaged over one gyroperiod is given by [*Bell*, 1986]

$$\frac{d\alpha}{dt} = - \frac{\omega_\tau^2}{k_z v_\perp} \left( 1 + \frac{\omega \cos^2 \alpha}{\gamma \omega_H - \omega} \right) \sin \eta + \frac{v_\perp}{2\omega_H} \frac{\partial \omega_H}{\partial z}$$

where  $\omega_\tau^2 = \kappa \omega_{\tau 0}^2 [J_0(\beta) - \alpha_1 J_2(\beta) + \alpha_2 J_1(\beta)]$ ,  $\kappa = [1 + \omega^2/(ck_z)^2]$ ,  $\omega_{\tau 0}^2 = (q/2\gamma m_0)(B_x^w + B_y^w)k_z v_\perp$ ,  $\beta = [1 - \omega/(\gamma^{-1}\omega_H)] \tan \alpha \tan \psi$ ,  $\alpha_1 = (B_x^w - B_y^w)/(B_x^w + B_y^w)$  and  $\alpha_2 = v_\perp^{-1} E_z^w/(B_x^w + B_y^w)$ , with  $J_i(\cdot)$  being the Bessel function of the first kind and  $i$ th order, and  $m_0$  and  $q$  being particle rest

mass and charge respectively. The conditions for the validity of the gyro-averaged equations of motion are discussed in Chapter 3.

We now consider electrons of a given energy with pitch angles in the vicinity of the loss cone at a given  $L$ -shell in the equatorial plane and investigate their cyclotron resonant interaction with whistler mode waves of different wave normal angles. The cyclotron resonance condition,  $v_z \equiv v_R = (\gamma^{-1} \omega_H - \omega) k_z^{-1}$ , determines the frequency of the wave for a given wave normal angle  $\psi$  ( $\psi$  is the angle between the wave vector  $\vec{k}$  and the magnetic field  $\vec{B}_0$  as discussed further in Chapter 3) that can resonantly interact with an electron with  $v_z \equiv v_R$ . The pitch angle scattering coefficient is calculated assuming that the waves have a power density (Poynting flux) of  $S = 9.7$  pW/m<sup>2</sup> corresponding to that of a ducted ( $\psi = 0^\circ$ ) wave at  $L = 3$  with the frequency of  $f = 16.2$  kHz ( $f/f_H = 0.5$ ) and magnetic field intensity of  $B_w = 1$  pT. The bandwidth of the wave ( $\Delta\omega/2\pi$ ) is assumed to be 200 Hz for all the waves considered in this section.

**Table 2.1. Equatorial electron density and pitch angles.** Ambient equatorial electron densities and energetic electron equatorial pitch angles used as input parameters for pitch angle diffusion coefficient calculations.

$L$	$N_e$ (e1/cc)	$\alpha_{eq}$ (deg)
2	1500	17
3	600	9
4	400	6

We consider electron energies of 1 keV, 10 keV and 100 keV at  $L = 2, 3$ , and 4. The equatorial electron densities and the equatorial pitch angles (close to the loss cone angle) at the  $L$ -shells considered are summarized in Table 2.1. The

values of equatorial electron densities given in Table 2.1 are used throughout this thesis.

### 2.2.2. Results

We use a formulation similar to that described in *Inan and Bell* [1991] to determine the wave frequency required for cyclotron resonance with  $E = 1, 10$  and  $100$  keV electrons at  $L = 2, 3$ , and  $4$  in the equatorial plane as a function of the wave normal angle, (i.e.,  $f(\psi)$ ), and the corresponding values of  $D_\alpha(\psi)$ . Results are presented in Figure 2.7.

The frequencies of the waves that would undergo cyclotron resonance with an electron of a given energy in the equatorial plane is higher for lower  $L$ -shells, ranging for example, for  $E = 1$  keV electrons, from  $5$  kHz at  $L = 4$  to  $\sim 80$  kHz at  $L = 2$  for ducted ( $\psi = 0^\circ$ ) waves. At a given  $L$ -shell, higher energy electrons resonantly interact with lower frequency waves; for example, at  $L = 2$ ,  $E = 1$  keV electrons resonate with  $\sim 80$  kHz waves with  $\psi = 0^\circ$ , while a wave with  $\psi = 0^\circ$  at  $\sim 15$  kHz resonantly interacts with  $E = 100$  keV electrons. Wave frequencies required for resonance for waves with  $0^\circ < \psi < 50^\circ$  at a given  $L$ -shell are weakly dependent on  $\psi$  ( $f(\psi) \cong \text{constant}$ ). For  $1$  keV electrons, the frequency of the resonant wave decreases with the wave normal angle for all  $L$ -shells as  $\psi \rightarrow \psi_r$  where  $\psi_r$  is the resonance cone angle at which the refractive index is infinite, as further discussed in Chapter 3. At high  $\psi$ 's, the  $f(\psi)$  curves for  $E = 100$  keV electrons exhibit a maximum which is more pronounced and occurs at higher  $\psi$ 's for higher  $L$ -shells. For example, the highest wave frequency for resonant interaction with  $100$  keV electrons at  $L = 4$  is  $f \sim 0.8$  kHz for  $\psi \sim 85^\circ$ , whereas that for a ducted wave ( $\psi = 0^\circ$ ) interacting with the same energy electrons is  $f \sim 0.2$  kHz. For  $10$  keV electrons  $f(\psi)$  decreases with  $\psi$  at high  $\psi$ 's for  $L = 2$ , whereas at  $L = 3$  and  $4$  it exhibits maxima similar to those for  $E = 100$  keV.

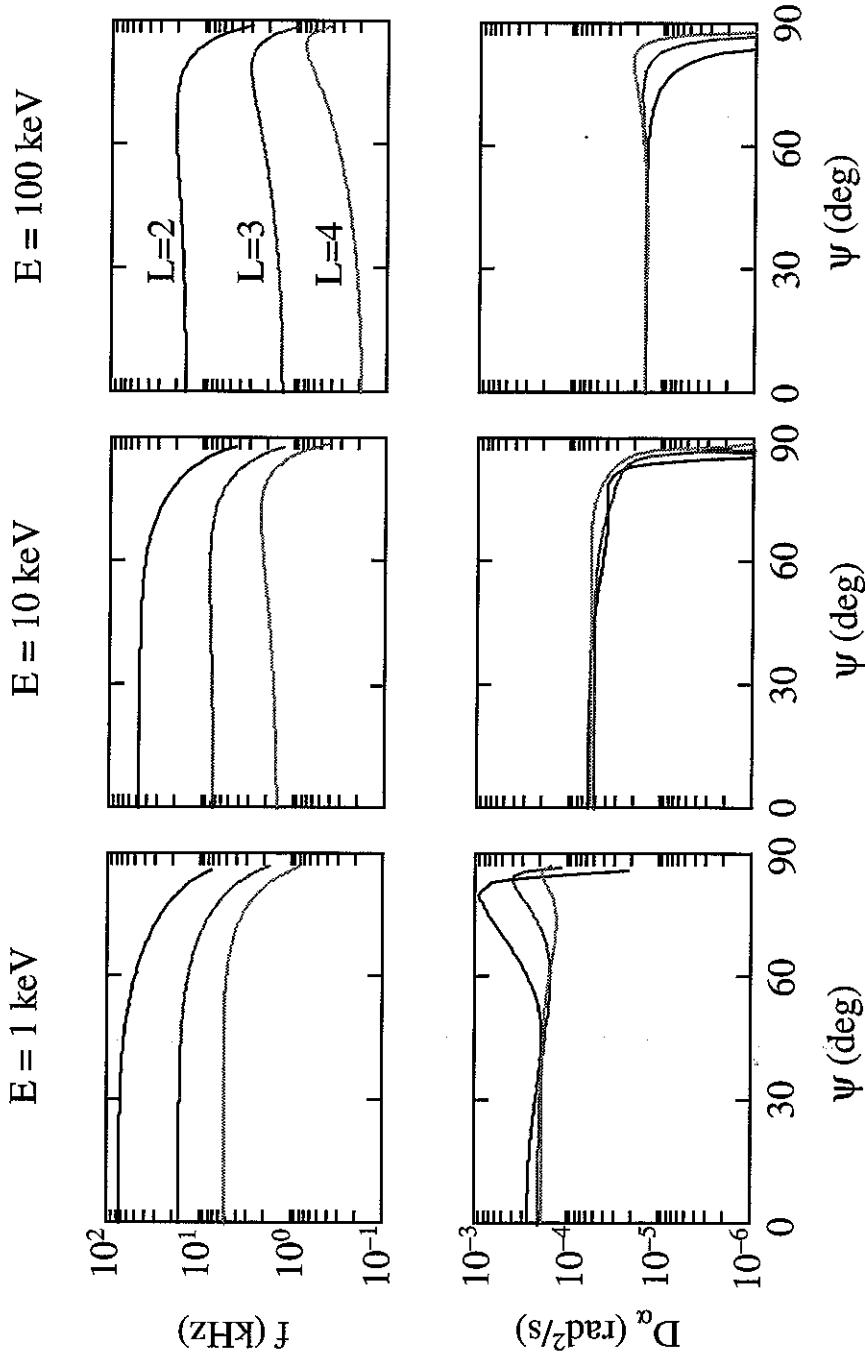


**Figure 2.7. Wave frequencies and diffusion coefficients.** Top panels show frequency vs wave normal angle for whistler mode waves cyclotron resonant with  $E = 1, 10$ , and  $100$  keV electrons at the equator at  $L = 2, 3$ , and  $4$ . Bottom panels show pitch angle diffusion coefficient vs wave normal angle for  $E = 1, 10$ , and  $100$  keV electrons resonantly interacting with waves of corresponding frequencies (from top panel) at the equator at  $L = 2, 3$ , and  $4$ .

We see from the lower panels of Figure 2.7 that, for electrons of a given energy, the pitch angle scattering coefficient  $D_\alpha(\psi)$  does not depend strongly on  $\psi$  for  $0^\circ < \psi < 50^\circ$ . Furthermore, for 10 keV and 100 keV electrons  $D_\alpha(\psi)$  appears to approximately have the same value for different  $L$ -shells. For 10 keV and 100 keV electrons at high  $\psi$ 's,  $D_\alpha(\psi)$  decreases rapidly with increasing  $\psi$ , whereas  $D_\alpha(\psi)$  at high  $\psi$ 's for 1 keV electrons exhibits interesting behavior. Before a rapid decrease for  $\psi$ 's close to  $90^\circ$ ,  $D_\alpha(\psi)$  exhibits pronounced maxima. For example, at  $L = 2$ ,  $D_\alpha(\psi = 0^\circ) \cong 3 \times 10^{-4} \text{ rad}^2/\text{s}$ . As  $\psi$  increases,  $D_\alpha(\psi)$  decreases slightly until it reaches local minimum of  $D_\alpha \sim 2 \times 10^{-4} \text{ rad}^2/\text{s}$  at  $\psi \sim 45^\circ$  and subsequently increases to the maximum of  $D_\alpha \sim 10^{-3} \text{ rad}^2/\text{s}$  at  $\psi \sim 80^\circ$  and rapidly decreases for higher  $\psi$ 's as  $\psi$  approaches the resonance cone. The rapid decrease  $D_\alpha(\psi) \rightarrow 0$  for  $\psi \rightarrow \psi_r$  has a fine structure with minima  $D_\alpha = 0$  due to  $\omega_\tau = 0$  as opposing effects of the different wave components cancel [Bell, 1986; Inan and Bell, 1991]. Comparing the curves for different electron energies,  $D_\alpha(\psi)$  is higher for lower energy electrons. For example  $D_\alpha(\psi = 0^\circ)$  has the value of  $\sim 2.5 \times 10^{-4} \text{ rad}^2/\text{s}$ ,  $\sim 6 \times 10^{-5} \text{ rad}^2/\text{s}$ , and  $\sim 1.5 \times 10^{-5} \text{ rad}^2/\text{s}$  for  $E = 1, 10$ , and 100 keV electrons respectively. The importance of these results arises from the fact that a large fraction of the waves in the magnetosphere propagate in the non-ducted (oblique) mode [Edgar, 1976].

### 2.2.3. Conclusions

Cyclotron resonant pitch angle scattering of electrons by oblique whistler mode waves appears to be at least as efficient as that due to parallel propagating (i.e., ducted) waves. For lower energy electrons (i.e., 1 keV), oblique whistler mode waves can be even more efficient in electron scattering than ducted whistlers. The precipitated energy fluxes caused by resonant interactions between radiation belt electrons and oblique whistlers would depend on various parameters such as whistler intensity, radiation belt electron distribution, and the distribution of the effective interaction region along the magnetic field line. To determine the resulting precipitation fluxes, we undertake a more detailed study based on a test particle formulation as

discussed in Chapter 4. Based on the pitch angle diffusion coefficients calculated here, we can expect cyclotron resonant interactions between relatively low energy electrons (1 keV) and oblique whistler mode waves to lead to significant precipitation energy fluxes. The scattering coefficients can often be higher than those for parallel propagating waves as shown earlier, and, also, trapped particle fluxes at the lower energies are typically higher for most magnetospheric particle distributions. Observed lightning induced precipitation events involving  $> 40$  keV electrons caused by whistler components propagating along the magnetic field lines [e.g., *Inan et al.*, 1990; *Burgess and Inan*, 1992] should thus be accompanied by substantial fluxes of lower energy electrons scattered by oblique whistler components caused by the same lightning discharges. A quantitative evaluation of the oblique whistler contribution to the precipitation of the radiation belt electrons is the subject of the following chapters.





# 3.

## Theoretical Formulation

Test particle equations of motion form the basis for the simulation method developed here for quantitative investigation of cyclotron resonance interactions between radiation belt electrons and oblique whistler mode waves in the magnetosphere. These equations of motion incorporate the effects on the particles' motion of the gradients of the Earth's magnetic field and within which interaction takes place and the wave electric and magnetic field forces that act on the radiation belt electrons. The equations of motion in the absence of the electromagnetic wave define the unperturbed electron trajectories and allow us to establish a suitable coordinate system for modeling the electron-wave interaction. The waves are assumed to be given, with their properties determined by the cold magnetosplasma and its gradients along the field line.

### 3.1. Mathematical Model of the Cold Magnetoplasma Medium

In the inner magnetosphere ( $L \leq 6$ ), the Earth's magnetic field lines are not significantly distorted by the solar wind and for our purposes can be modeled using a centered dipole tilted with respect to the rotational axis by  $\sim 11^\circ$ . The magnetic field intensity is then given by

$$B(L, \lambda) = \frac{B_0}{L^3} \frac{\sqrt{1 + 3 \sin^2 \lambda}}{\cos^6 \lambda}$$

where  $L$  is the  $L$ -shell value,  $\lambda$  is the geomagnetic latitude and  $B_0 = 3.12 \times 10^{-5} \text{ T}$ .

A dipole field line ( $L$ -shell) is defined as

$$r(L, \lambda) = r_{eq} \cos^2 \lambda = LR_e \cos^2 \lambda$$

where  $R_e = 6370 \text{ km}$  is the Earth's radius. Note that, as was defined before,  $r(L, \lambda = 0^\circ) = r_{eq} = LR_e$ , so that the  $L$  value corresponds to the geocentric distance at which a given magnetic field line crosses the geomagnetic equator (Figure 3.1).

In the inner magnetosphere, the background 'cold' plasma consists of particles with typically less than a few eV energy, with the electron gyroradii being of the order of a few meters. Under such conditions, centrifugal forces and the Earth's gravity act upon the electrically neutral isothermal mixture of electrons and positive ions ( $\text{H}^+$ ,  $\text{He}^+$  and  $\text{O}^+$ ) to form a diffusive equilibrium along the magnetic field lines [Angerami and Thomas, 1964]. The variation along the magnetic field lines of the electron density for the diffusive equilibrium model of the cold plasma density is given by [Park, 1972]

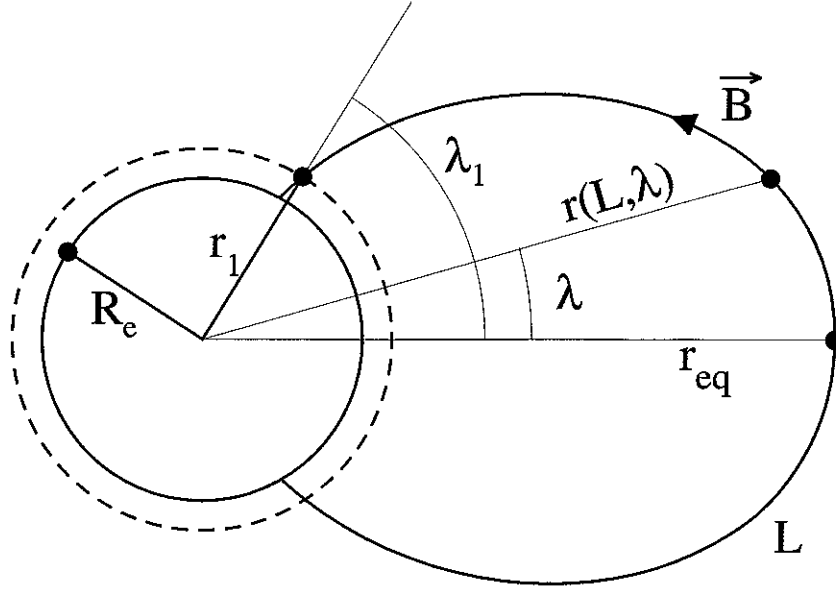


**Figure 3.1. Dipole magnetic field geometry.** Coordinate system for dipole magnetic field geometry.

$$N_e(L, \lambda) = N_1 \sqrt{\sum_i \xi_{il} \exp\left(-\frac{z}{H_i}\right)},$$

where

$$z = r_1 - \frac{r_1^2}{r} - \frac{\Omega^2}{2g_1} (r^2 \cos^2 \lambda - r_1^2 \cos^2 \lambda_1)$$

$$H_i = \frac{kT}{m_i g_1}$$

and  $\xi$  is the fractional abundance of ionic species,  $r$  is the geocentric distance depending on both  $L$  and  $\lambda$ ,  $\Omega$  is the angular rotational speed of the Earth,  $g$  is the gravitational acceleration,  $\lambda$  is the dipole latitude,  $k$  is Boltzmann's constant,  $T$  is the temperature and  $m$  is the particle mass. The subscript  $i$  refers to the  $i$ th ionic species ( $H^+$ ,  $He^+$  and  $O^+$ ), and the subscript 1 refers to the reference level at 1000 km altitude. Figure 3.1. illustrates the coordinates and the symbols used.

### 3.2. Oblique Whistler-Mode Waves

The properties (dispersion relation, polarization of the wave fields, group velocity) of the electromagnetic waves that are supported by the cold, infinite, homogeneous, collisionless plasma in the presence of the external homogeneous, static magnetic field  $B_0$  are derived from Maxwell's equations

$$\begin{aligned}\nabla \times \vec{E} &= -\frac{\partial \vec{B}}{\partial t} \\ \nabla \times \vec{B} &= \mu \vec{j} + \frac{1}{c^2} \frac{\partial \vec{E}}{\partial t} \quad ,\end{aligned}$$

where the plasma current is given by

$$\vec{j} = \sum_k n_k q_k \vec{v}_k \quad ,$$

and the motion of the charged particles constituting the plasma is governed by the Lorentz's force equation

$$m_k \frac{d\vec{v}_k}{dt} = q_k (\vec{E} + \vec{v}_k \times \vec{B})$$

where  $\vec{E}$  and  $\vec{B}$  are the total electric and magnetic fields, and  $n_k$ ,  $m_k$ ,  $q_k$  and  $\vec{v}_k$  are the density, mass, charge and velocity respectively of the  $k$ th species of particles in the plasma [Stix, 1962]. To represent the variation of the wave characteristics along its propagation path due to the variation of the ambient cold plasma, we use the slowly varying (WKB) plane wave approximation (the first order quantities are assumed to vary as  $e^{i(\omega t - \vec{k} \cdot \vec{r})}$ ) which is valid here since the electrical characteristics of the propagation medium do not change substantially over the distance of the order of a wavelength. For a wave that propagates at an angle  $\psi$  with respect to the direction opposite to that of the

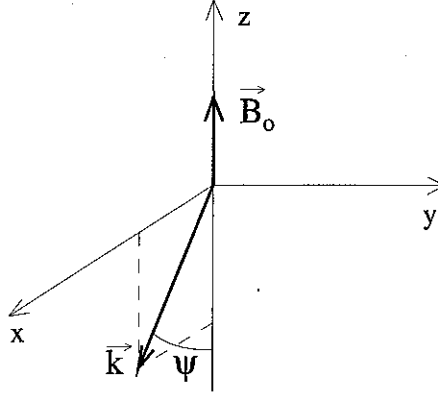


**Figure 3.2. Wave vector orientation.** Coordinate system for an electromagnetic wave with wave vector  $\vec{k}$  in the presence of an ambient magnetic field  $\vec{B}_0$ . The wave vector lies in the  $x$ - $z$  plane.

ambient magnetic field (Figure 3.2), the condition for a non-trivial solution of the above equations gives the dispersion relation which can be solved for the square of the refractive index

$$n^2 = \frac{B_S \pm F_S}{2A_S}$$

where

$$A_S = S_S \sin^2 \psi + P_S \cos^2 \psi$$

$$B_S = R_S L_S \sin^2 \psi + P_S S_S (1 + \cos^2 \psi)$$

$$F_S^2 = (R_S L_S - P_S S_S)^2 \sin^4 \psi + 4P_S^2 D_S^2 \cos^2 \psi$$

$$S_S = (R_S + L_S)/2$$

$$D_S = (R_S - L_S)/2$$

and

$$P_S = 1 - \sum_k \frac{\omega_{pk}^2}{\omega^2}, \quad R_S = 1 - \sum_k \frac{\omega_{pk}^2}{\omega^2} \left( \frac{\omega}{\omega + \omega_{Hk}} \right), \quad L_S = 1 - \sum_k \frac{\omega_{pk}^2}{\omega^2} \left( \frac{\omega}{\omega - \omega_{Hk}} \right)$$

$$\omega_{pk}^2 = \frac{n_k q_k^2}{\epsilon_o m_k}, \quad \omega_{Hk} = \frac{q_k B_o}{m_k}$$

with  $\omega_{pk}$  and  $\omega_{Hk}$  being the plasma and cyclotron frequencies of the  $k$ th species respectively. Note that theoretically there are two branches of  $n^2$  that satisfy the dispersion relation, each representing elliptically polarized waves but with the opposite sense of rotation around the ambient magnetic field. However, the typical parameters of the Earth's magnetosphere (i.e., plasma and cyclotron frequencies) are such that for frequencies between the electron and proton gyrofrequencies only those waves whose fields rotate in the same sense around the ambient magnetic field as the electrons can propagate [Helliwell, 1965]. The dispersion relation shows that the refractive index of the wave as well as its phase velocity ( $V_{ph} = \omega/k$ , where  $k = n\omega/c$  is the wave vector and  $c$  is the speed of light) and group velocity ( $\vec{V}_g = d\omega/d\vec{k}$ ) vary with both the wave frequency,  $\omega$ , and the direction of propagation,  $\psi$ . These features are characteristic of electromagnetic wave propagation in a dispersive and anisotropic medium, which the Earth's magnetosphere is in this frequency range.

The wave electric and magnetic fields are given as

$$\begin{aligned}\vec{E}^w &= -\hat{e}_x E_x^w \sin \Phi + \hat{e}_y E_y^w \cos \Phi - \hat{e}_z E_z^w \sin \Phi \\ \vec{B}^w &= \hat{e}_x B_x^w \cos \Phi + \hat{e}_y B_y^w \sin \Phi - \hat{e}_z B_z^w \cos \Phi\end{aligned}\tag{3.1}$$

where  $\Phi = \omega t - \vec{k} \cdot \vec{r}$  is the wave phase, and the polarization ratios are

$$\begin{aligned}\rho_1 &= \frac{E_z^w}{E_y^w} = \frac{(n^2 - S_S)n^2 \sin \psi \cos \psi}{D_S(n^2 \sin^2 \psi - P_S)} \\ \rho_2 &= \frac{E_x^w}{E_y^w} = \frac{(n^2 - S_S)}{D_S} \\ \rho_{m1} &= \frac{B_z^w}{B_y^w} = \tan \psi \frac{B_x^w}{B_y^w} \\ \rho_{m2} &= \frac{B_x^w}{B_y^w} = -\frac{D_S(n^2 \sin^2 \psi - P_S)}{P_S(n^2 - S_S)}\end{aligned}$$

It is useful to express the wave intensity in terms of the wave power density or the Poynting flux  $\vec{S}$ , which is defined as

$$\vec{S} = \vec{E}^w \times \vec{H}^w$$

From this, one has for the time averaged Poynting flux value

$$S = \frac{c}{2\mu_o} |B_y^w|^2 (\rho_2^2 X^2 n \cos \psi)^{-1} \sqrt{(\tan \psi - \rho_1 \rho_2 X)^2 + (1 + \rho_2^2 X)^2} \quad 3.2.$$

where

$$\mu_o = 4\pi \times 10^{-7} \frac{H}{m},$$

$$X = \frac{P}{(P - n^2 \sin^2 \psi)}.$$

All equations in this section are derived for a homogeneous medium. The magnetosphere is not a homogeneous medium since both the plasma density and magnetic field (and therefore  $\omega_{pk}$  and  $\omega_{Hk}$ ) vary in space. Fortunately, these spatial variations are generally small over the distance of the order of the wavelength, so that at any given point, the wave propagation can be represented using the slowly varying approximation (WKB) in which the wave is assumed to have the same characteristics as those of a wave traveling in a homogeneous medium having the same refractive index. Therefore the equations derived above are valid for electromagnetic waves propagating through the Earth's magnetosphere, and are used in Figures 3.3 through 3.6 to show the dependence on wave frequency and direction of propagation (wave normal angle,  $\psi$ ) of the wave refractive index,  $n$ , polarizations,  $\rho_1$ ,  $\rho_2$ ,  $\rho_{m1}$ ,  $\rho_{m2}$  and phase and group velocity,  $V_{ph}$  and  $V_g$ . Note that the scaling on these figures is not fine enough for the lower cutoff frequency (equatorial proton gyrofrequency of 17.5 Hz at  $L = 3$ ) to be discernible.

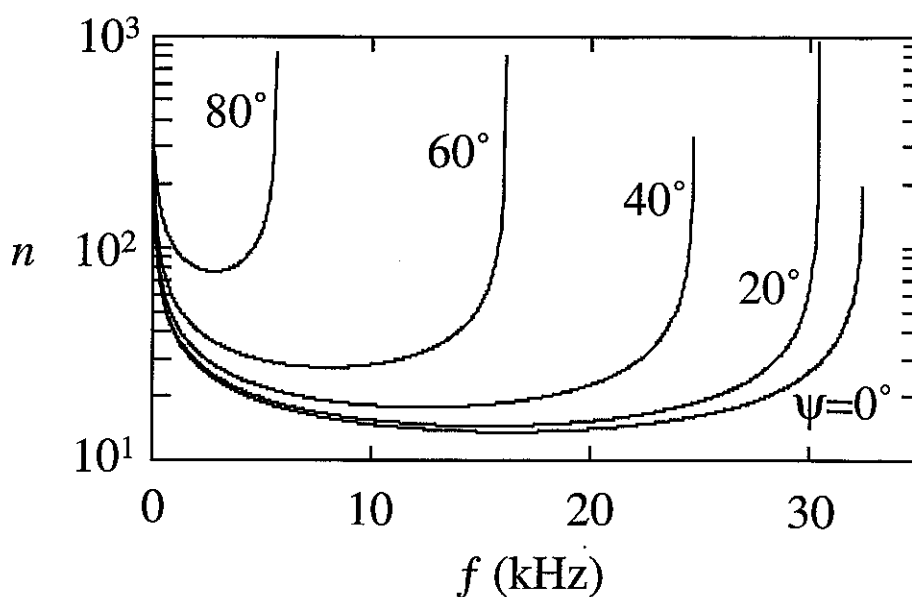


**Figure 3.3. Wave refractive index.** Dependence of the wave refractive index  $n$  on wave frequency  $f$  for the various wave normal angles  $\psi$  at the equator at  $L=3$ . The equatorial electron density at  $L=3$  was taken to be 600 el/cm<sup>3</sup>, as given in Figure 2.3.

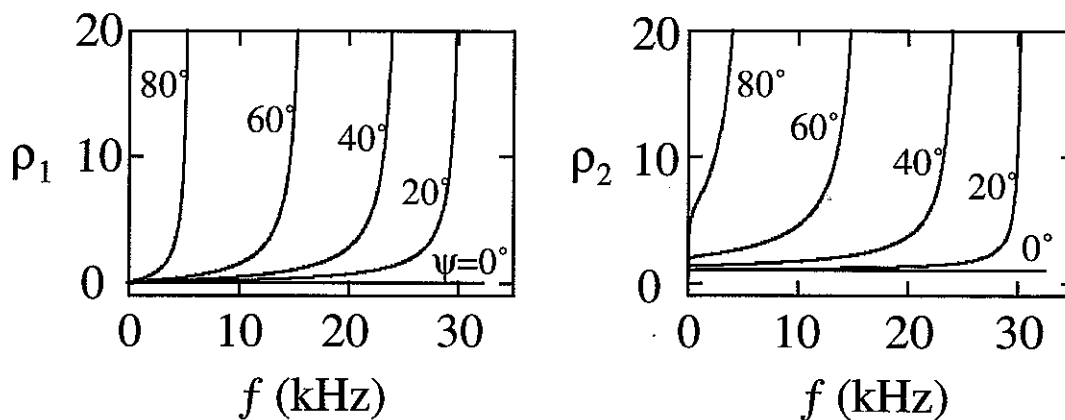


**Figure 3.4. Wave polarization: electric field.** The polarization of the wave electric field  $\rho_1 = E_z^w/E_y^w$  and  $\rho_2 = E_x^w/E_y^w$  as a function of wave frequency  $f$  and wave normal angle  $\psi$  at the equator at  $L=3$ .



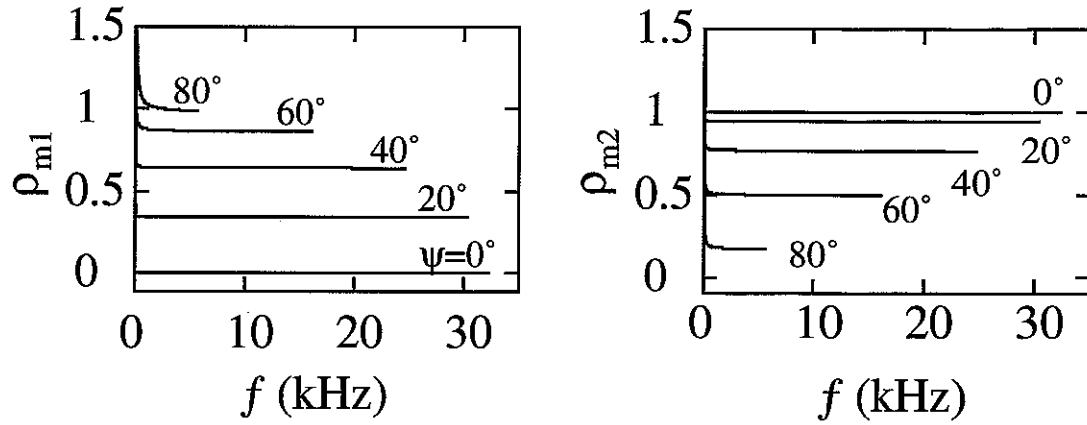


**Figure 3.5. Wave polarization: magnetic field.** The polarization of the wave magnetic field  $\rho_{m1} = B_z^w/B_y^w$  and  $\rho_{m2} = B_x^w/B_y^w$  as a function of wave frequency  $f$  and wave normal angle  $\psi$  at the equator at  $L=3$ .

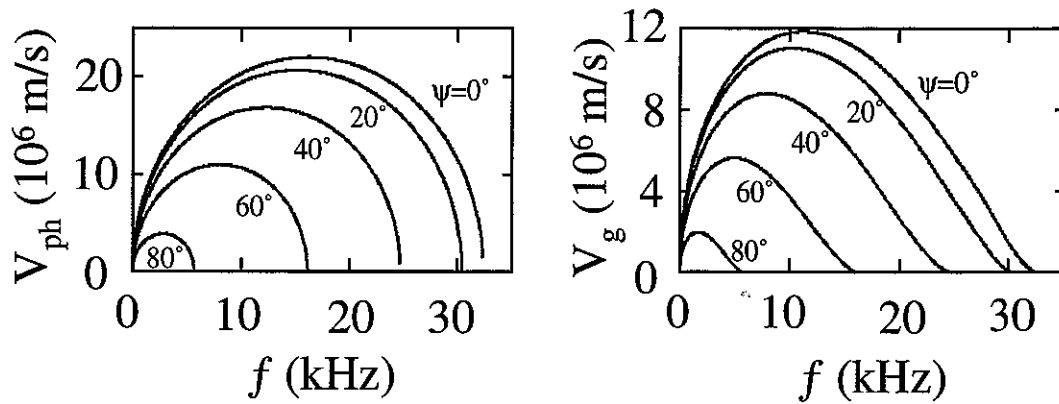


**Figure 3.6. Wave phase and group velocities.** The dependence on the wave frequency  $f$  of the wave phase and group velocities  $V_{ph}$  and  $V_g$  for waves with different directions of propagation ( $\psi$ ) at the equator at  $L=3$ .

### 3.3. Unperturbed Electron Trajectories

The complex trajectories of radiation belt electrons can be decomposed into three components, gyration around the magnetic field line, reflection back and forth along the magnetic field line between the two mirror points, and drift around the Earth in the eastward direction [Roederer, 1970].

Gyration around the magnetic field line is governed by the Lorentz's force,  $F_L = -ev_{\perp}B$ , balanced with the centrifugal force,  $F_{CF} = mv_{\perp}^2/r$ , where  $e$  and  $m$  are the electron charge and mass respectively,  $B$  is the Earth's magnetic field intensity,  $v_{\perp}$  is the electron velocity perpendicular to the magnetic field and  $r$  is the radius of the electron orbit. Since the electron gyroradius is  $r = mv_{\perp}/eB = v_{\perp}/\omega_H$ , where  $\omega_H = eB/m$  is electron cyclotron frequency, for a fixed location along the field line ( $\omega_H = \text{const.}$ )  $r$  depends linearly on  $v_{\perp}$ , and is of the order of 1–100 m.

The motion along the magnetic field line stretches the gyration circle into a helix. The bounce motion of the electrons along the magnetic field line reflecting between the two mirror points in the opposite hemispheres is governed by the so called first adiabatic invariant [Chen, 1984]

$$\mu = \frac{p_{\perp}^2}{B} = \text{const}$$

The first adiabatic invariant determines the dependence of the electron gyroradius along the field line on geomagnetic latitude

$$r = \frac{m \sqrt{\mu}}{e \sqrt{B}} = \frac{\text{const}}{\sqrt{B}} .$$

The electron gyroradius  $r$  is larger for weaker magnetic fields (close to the equator) and smaller for stronger fields (close to the mirror points).

The first adiabatic invariant also determines the relationship between the equatorial pitch angle,  $\alpha_{eq}$ , and mirror latitude,  $\lambda_m$ . Using  $\mu_{eq} = \mu_m$  and the conservation of energy (at the mirror point  $v_z = 0$  and  $v_{\perp} = v$ , where  $v_z, v_{\perp}$  and  $v$  are the electron velocities parallel and perpendicular to the magnetic field, and total electron velocity respectively) we find

$$\alpha_{eq}(\lambda_m) = \arcsin \sqrt{\frac{\cos^6 \lambda_m}{\sqrt{1 + 3 \sin^2 \lambda_m}}}$$

Note that  $\alpha_{eq}(\lambda_m)$  does not depend on electron velocity (energy), as was discussed earlier in connection with Figure 1.7 in Chapter 1.

The expressions for radiation belt electron trajectories in velocity space also follow from the first adiabatic invariant and conservation of energy, in both explicit form

$$v_{\perp}(\lambda) = \sqrt{\frac{B(\lambda, L)}{B_{eq}(L)}} v_{zeq} \tan \alpha_{eq} = \sqrt{\frac{\sqrt{1 + 3 \sin^2 \lambda}}{\cos^6 \lambda}} v_{zeq} \tan \alpha_{eq}$$

$$v_z(\lambda) = \frac{v_{zeq}}{\cos \alpha_{eq}} \sqrt{1 - \frac{\sqrt{1 + 3 \sin^2 \lambda}}{\cos^6 \lambda} \sin^2 \alpha_{eq}}$$

and as coupled equations of motion in the time domain (using the time derivative of  $\mu = \text{const}$  and  $E = \text{const}$ )

$$\begin{aligned} \dot{v}_{\perp} &= v_{\perp} v_z \frac{1}{2B} \frac{\partial B}{\partial z} \\ \dot{v}_z &= -\frac{v_{\perp}}{v_z} \dot{v}_{\perp} = -v_{\perp}^2 \frac{1}{2B} \frac{\partial B}{\partial z} \end{aligned} \tag{3.3}$$

The third component of the radiation belt electron motion is the eastward drift around the Earth due to the gradient and curvature of the magnetic field [Chen, 1984]. The frequency of this periodic motion is of the order of  $10^{-4}$  Hz [Schultz and Lanzerotti, 1974] and is much smaller than the gyrofrequency (of the order of  $10^6$  Hz) and the frequency of the reflection between the mirror points (of the order of  $10^{-1}$  Hz) so that the particle drift around the Earth can be neglected during the course of the interactions simulated here and we only need to consider the cyclotron rotation and bounce motion along the field lines for our investigation of resonant electron-wave interactions.

### 3.4. Test Particle Equations of Motion

In this section, the equations of motion for relativistic electrons interacting with an oblique whistler mode wave are derived following the same procedure used by Bell [1984] for non-relativistic electrons.

The charged particle motion under the influence of an electromagnetic field is governed by the Lorentz's force equation

$$\frac{d\vec{p}}{dt} = q(\vec{E} + \frac{\vec{p}}{m\gamma} \times \vec{B}) \quad 3.4.$$

where  $\vec{E}$  and  $\vec{B}$  are the electric and magnetic field,  $\vec{p}$ ,  $q$  and  $m$  are the particle's momentum, charge and mass respectively, and

$$\gamma = \frac{1}{\sqrt{1 - \frac{v^2}{c^2}}} = \sqrt{\frac{p^2}{m^2 c^2} + 1}$$

For the special case of an electron interacting with an oblique whistler mode wave in the presence of the Earth's magnetic field, Eq. 3.4 becomes

$$\frac{d\vec{p}}{dt} \equiv \dot{\vec{p}} = -e \left[ \vec{E}^w + \frac{\vec{p}}{m_e \gamma} \times (\vec{B}^w + \vec{B}_o(\vec{r})) \right] \quad 3.5.$$

The oblique whistler mode wave electric and magnetic fields are (see Eq. 3.1 in the section 3.2)

$$\begin{aligned} \vec{E}^w &= -\hat{e}_x E_x^w \sin \Phi + \hat{e}_y E_y^w \cos \Phi - \hat{e}_z E_z^w \sin \Phi \\ \vec{B}^w &= \hat{e}_x B_x^w \cos \Phi + \hat{e}_y B_y^w \sin \Phi - \hat{e}_z B_z^w \cos \Phi \end{aligned}$$

Note that these can be expressed as a sum of right and left hand circularly polarized waves, for example

$$\vec{B}^w = \vec{B}_R + \vec{B}_L - \hat{e}_z B_z^w \cos \Phi$$

where

$$\begin{aligned} \vec{B}_R &= \frac{B_x^w + B_y^w}{2} (\hat{e}_x \cos \Phi + \hat{e}_y \sin \Phi) \\ \vec{B}_L &= \frac{B_x^w - B_y^w}{2} (\hat{e}_x \cos \Phi - \hat{e}_y \sin \Phi) \end{aligned}$$

The Earth's magnetic field is assumed to be slowly varying along the field line ( $z$  axis) and locally parallel to the  $z$  axis (the geometry of the interaction is given in the Figure 3.7), namely

$$\vec{B}_o(\vec{r}) = \vec{B}_{oz}(z) + \vec{B}_{o\perp}(x, y, z)$$

For a dipole model,  $\vec{B}_{o\perp}$  can be evaluated using a Taylor expansion in  $x$  and  $y$

$$\vec{B}_{o\perp} \approx -(\hat{e}_x \cos \xi_o + \hat{e}_y \sin \xi_o)(x \cos \xi_o + y \sin \xi_o) \frac{\partial B_{oz}}{\partial z}$$

where  $\xi_o$  is the angle between the magnetic meridional plane and the  $x$ - $z$  plane.

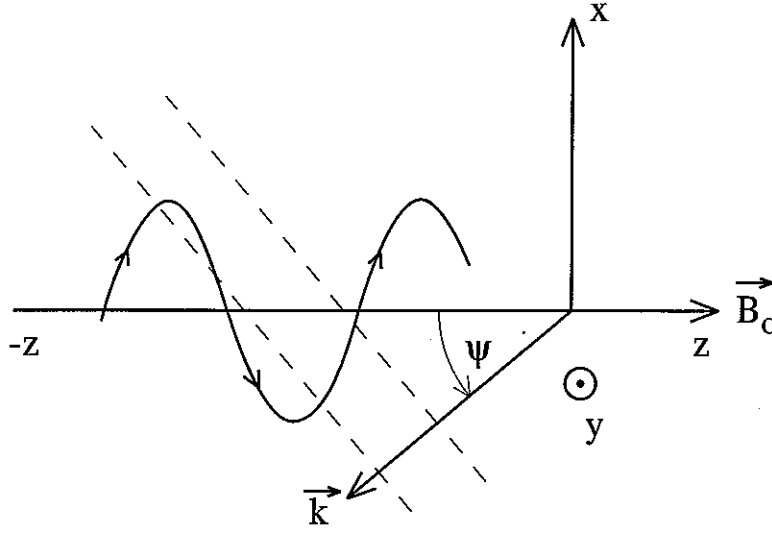


**Figure 3.7. Wave-particle interaction geometry.** Geometry of the interaction between a gyrating electron and a non-ducted coherent wave propagating at an angle  $\psi$  with respect to the negative  $z$  axis. The coordinate system is chosen such that the wave vector  $\vec{k}$  is in the  $x$ - $z$  plane. The Earth's magnetic field  $B_0$  is assumed to be locally parallel to the  $z$  axis. The planes of constant wave phase are shown as dashed lines.

Substitution of the expressions for the Earth's magnetic field and wave electric and magnetic fields into the vector equation of motion (Eq. 3.5) gives three scalar equations of motion

$$\dot{p}_x = eE_x^w \sin \Phi - \frac{e}{m_e \gamma} [p_y (-B_z^w \cos \Phi + B_{oz}) - p_z (B_y^w \sin \Phi + B_{oLy})]$$

$$\dot{p}_y = -eE_y^w \cos \Phi - \frac{e}{m_e \gamma} [-p_x (-B_z^w \cos \Phi + B_{oz}) + p_z (B_x^w \cos \Phi + B_{oLx})]$$

$$\dot{p}_z = eE_z^w \sin \Phi - \frac{e}{m_e \gamma} [p_x (B_y^w \sin \Phi + B_{oLy}) - p_y (B_x^w \cos \Phi + B_{oLx})]$$

However, in the presence of an external magnetic field (Earth's magnetic field) the equations of motion are expected to be simpler if expressed in terms of electron momenta (velocities) parallel and perpendicular to the magnetic field line,  $p_z$  and  $p_\perp$  respectively. Since resonant electron-wave interaction occurs when the gyration of the electron is in phase with the right hand

elliptically polarized component of the oblique whistler mode wave, the angle between the magnetic field of the right hand elliptically polarized wave component ( $\vec{B}_R$ ) and the perpendicular component of electron's momentum ( $\vec{p}_\perp$ )(i.e., the angle  $\varphi$  in Figure 3.8.) arises as the most appropriate third coordinate for describing the electron trajectory.

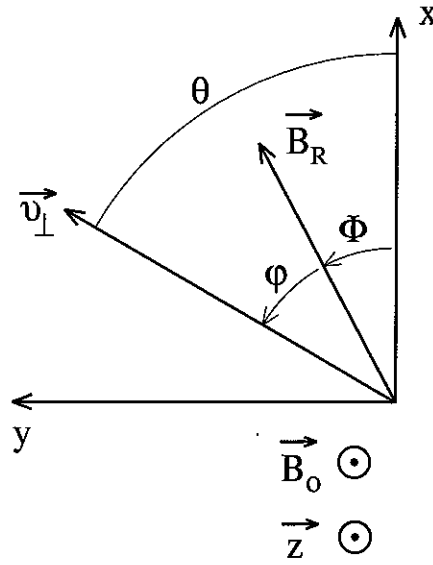


**Figure 3.8. Electron phase with respect to the wave.** Angle  $\varphi$  is that between  $\vec{B}_R$ , the right hand circularly polarized component of the wave magnetic field and  $\vec{v}_\perp$ , the component of the electron velocity vector which is perpendicular to  $\vec{B}_0$ . Angle  $\theta = \varphi + \Phi$  represents electron phase with respect to the  $x$  axis whereas  $\Phi$  is the wave phase.

Substituting

$$p_x = p_\perp \cos \theta$$

$$p_y = p_\perp \sin \theta$$

$$\theta = \varphi + \Phi$$

$$\begin{aligned} \dot{\Phi} &= \frac{d\Phi}{dt} = \frac{\partial \Phi}{\partial t} + \frac{d\vec{r}}{dt} \cdot \frac{\partial \Phi}{\partial \vec{r}} = \frac{d}{dt} \left( \int \omega dt - \int \vec{k} d\vec{r} \right) = \\ &= \omega - \vec{v} \cdot \vec{k} = \omega + v_x k_x + v_z k_z \end{aligned}$$

into the rectangular coordinate version of the equations of motion and recognizing

$$\frac{B^w}{B_o} \cong 10^{-4} - 10^{-5}, \quad \frac{p_z}{p_\perp} \leq \frac{1}{\tan \alpha_{lc}} \ll 10^3 - 10^4,$$

$$E^w \sim \frac{c}{n} B^w, \quad \frac{\omega/k}{v_\perp} < 10^4 - 10^5$$

to neglect lower order terms in the equation for  $\dot{\phi}$ , gives

$$\begin{aligned} \dot{\phi} &= \frac{\omega_H}{\gamma} - \omega - \frac{p_x}{m_e \gamma} k_x - \frac{p_z}{m_e \gamma} k_z - \frac{1}{\gamma} A_1 \\ \dot{p}_z &= \frac{1}{\gamma} \omega_2 p_\perp \sin(\phi + 2\Phi) + \frac{1}{\gamma} \omega_1 p_\perp \sin \phi + e E_z^w \sin \Phi - m_e A_2 \\ \dot{p}_\perp &= -\omega_1 \left( \frac{p_z}{\gamma} + m_e R_1 \right) \sin \phi - \omega_2 \left( \frac{p_z}{\gamma} - m_e R_2 \right) \sin(\phi + 2\Phi) + m_e A_3 \end{aligned} \quad 3.6.$$

where

$$\begin{aligned} \omega_1 &= \frac{e}{m_e} \frac{B_x^w + B_y^w}{2}, \quad \omega_2 = \frac{e}{m_e} \frac{B_x^w - B_y^w}{2} \\ R_1 &= \frac{E_x^w + E_y^w}{B_x^w + B_y^w}, \quad R_2 = \frac{E_x^w - E_y^w}{B_x^w - B_y^w} \\ A_1 &= \frac{e}{m_e} v_z (\vec{v}_\perp \cdot \vec{B}_{o\perp}) v_\perp^{-2} = \frac{e}{m_e} \frac{p_z}{p_\perp} (B_{o\perp x} \cos(\phi + \Phi) + B_{o\perp y} \sin(\phi + \Phi)) \\ A_2 &= \frac{e}{m_e} (\vec{v}_\perp \times \vec{B}_{o\perp}) \cdot \hat{e}_z = \frac{e}{m_e} \frac{p_\perp}{m_e \gamma} (B_{o\perp y} \cos(\phi + \Phi) - B_{o\perp x} \sin(\phi + \Phi)) \\ A_3 &= \frac{e}{m_e} \frac{v_z}{v_\perp} (\vec{v}_\perp \times \vec{B}_{o\perp}) \cdot \hat{e}_z = \frac{e}{m_e} \frac{p_z}{m_e \gamma} (B_{o\perp y} \cos(\phi + \Phi) - B_{o\perp x} \sin(\phi + \Phi)) \end{aligned}$$

Equations 3.6 determine the detailed electron motion under the influence of the wave forces including its gyration around the Earth's magnetic field line. However, for our investigation of resonant electrons' pitch angle scattering



and their precipitation, the gyro-averaged version of these equations is sufficient. This is because the period of the electron circular motion around the field line is short ( $\sim 10^{-6}$  s) compared to the time scale of the wave-particle interaction ( $10^{-3}$ – $10^{-2}$  s) [Bell, 1984]. To compactly express the gyro-averaged form of the equations, it is useful to introduce three new variables  $\chi$ ,  $\eta$  and  $\sigma$

$$\chi: \quad \chi = \int k_x dx \Rightarrow \dot{\chi} = k_x v_x$$

$$\eta: \quad \varphi = \eta - \chi \Rightarrow \dot{\varphi} = \dot{\eta} - \dot{\chi}$$

$$\sigma: \quad \dot{\varphi} = \frac{\omega_H}{\gamma} - \omega - k_x v_x - k_z v_z \Rightarrow \varphi = \frac{\omega_H}{\gamma} t - \Phi + \varphi_o + \Phi_o$$

$$\Phi = \frac{\omega_H}{\gamma} t + \theta_o - \varphi = \sigma - \varphi = \sigma - \eta - \chi$$

$$\sigma = \frac{\omega_H}{\gamma} t + \theta_o, \quad \theta_o = \varphi_o + \Phi_o$$

The usefulness of  $\eta$  arises from the relation

$$\eta \equiv \underline{\eta} = \underline{\varphi}$$

where the bar under the symbol indicates an average over one gyroperiod. As shown in [Bell, 1984], physically the phase angle  $\eta$  can be conceived as the value of  $\varphi$  (electron gyration phase with respect to the right hand circularly polarized component of the wave magnetic field) averaged over one gyroperiod.

Using these new variables the equations of motion can be rewritten as

$$\dot{\eta} = \frac{\omega_H}{\gamma} - \omega - k_z v_z - \frac{1}{\gamma} A_1$$

$$\dot{p}_z = \omega_{\tau o}^2 k_z^{-1} [\sin(\eta - \chi) + \alpha_1 \sin(2\sigma + \chi - \eta) + \gamma \alpha_2 \sin(\sigma + \chi - \eta)] - m_e A_2$$

$$\dot{p}_\perp = - \left[ \omega_1 \left( \frac{p_z}{\gamma} + m_e R_1 \right) \sin(\eta - \chi) + \omega_2 \left( \frac{p_z}{\gamma} - m_e R_2 \right) \sin(2\sigma + \chi - \eta) \right] + m_e A_3$$

where

$$\omega_{\tau o}^2 = \frac{\omega_1 k_z p_{\perp}}{\gamma}, \quad \alpha_1 = \frac{\omega_2}{\omega_1}, \quad \alpha_2 = \frac{eE_z^w}{\omega_1 p_{\perp}}$$

These equations can now be averaged over one cyclotron period using

$$\begin{aligned} \chi &= \int k_x dx = k_x v_{\perp} \int \cos(\varphi + \Phi) dt = \\ &= k_x v_{\perp} \int \cos(\omega_H t + \theta_o) dt = \frac{k_x v_{\perp}}{\omega_H} \sin \sigma = \beta \sin \sigma \end{aligned}$$

and

$$e^{i\beta \sin \sigma} = \sum_{m=-\infty}^{\infty} J_m(\beta) e^{im\sigma} \Rightarrow \begin{cases} \cos(\beta \sin \sigma) = \sum_{m=-\infty}^{\infty} J_m(\beta) \cos(m\sigma) \\ \sin(\beta \sin \sigma) = \sum_{m=-\infty}^{\infty} J_m(\beta) \sin(m\sigma) \end{cases}$$

where  $J_m$  are Bessel functions of the first kind and  $m$ th order and

$$\beta = \frac{k_x p_{\perp}}{\omega_H \gamma m_e} = \frac{p_{\perp} k \sin \psi}{\omega_H \gamma m_e}.$$

We find

$$\begin{aligned} \dot{\eta} &= \frac{\omega_H}{\gamma} - \omega - \frac{p_z k \cos \psi}{m_e \gamma} - \frac{1}{\gamma} \underline{A}_1 \\ \dot{p}_z &= \omega_{\tau}^2 k_z^{-1} \sin \eta - m_e \underline{A}_2 \\ \dot{p}_{\perp} &= - \left[ \omega_1 \left( \frac{p_z}{\gamma} + m_e R_1 \right) J_o(\beta) - \omega_2 \left( \frac{p_z}{\gamma} - m_e R_2 \right) J_2(\beta) \right] \sin \eta + m_e \underline{A}_3 \end{aligned} \tag{3.7}$$

with  $\omega_{\tau}^2 = \omega_{\tau o}^2 [J_o(\beta) - \alpha_1 J_2(\beta) + \gamma \alpha_2 J_1(\beta)]$ .

The expressions for  $\underline{A}_1$ ,  $\underline{A}_2$  and  $\underline{A}_3$  are derived using the approximation for  $B_{o\perp}$  given earlier

$$\begin{aligned}\underline{A}_1 &= 0 \\ \underline{A}_2 &= \frac{1}{\gamma m_e^2} \frac{p_\perp^2}{2\omega_H} \frac{\partial \omega_H}{\partial z} \\ \underline{A}_3 &= \frac{1}{\gamma m_e^2} \frac{p_\perp p_z}{2\omega_H} \frac{\partial \omega_H}{\partial z}\end{aligned}$$

Note that these terms represent the adiabatic part of the electron motion, which occurs in the absence of the wave when all other terms in the gyro-averaged equations vanish and we have

$$\begin{aligned}\dot{p}_z &= -\frac{1}{\gamma m_e} \frac{p_\perp^2}{2\omega_H} \frac{\partial \omega_H}{\partial z} \\ \dot{p}_\perp &= \frac{1}{\gamma m_e} \frac{p_\perp p_z}{2\omega_H} \frac{\partial \omega_H}{\partial z}\end{aligned}$$

which resembles the equations for the unperturbed electron trajectory (Eq. 3.3), derived in section 3.3.

The first gyro-averaged electron equation of motion in 3.7 gives the rate of change of the average electron gyration phase  $\eta$  with respect to the right hand circularly polarized component of the wave's magnetic field. The condition for resonant electron-wave interaction is thus

$$\dot{\eta} = \frac{\omega_H}{\gamma} - \omega - k_z v_z = 0$$

This condition can be used to derive a more convenient variable for establishing the resonant condition, namely, the velocity  $v_R$  in the  $z$  direction that an electron must have in order to be in the resonance with the wave

$$v_R = \frac{\sqrt{\omega^2 k_z^2 + (\omega_H^2 - \omega^2) \left( k_z^2 + \frac{\omega_H^2}{c^2 \cos^2 \alpha} \right)} - \omega k_z}{k_z^2 + \frac{\omega_H^2}{c^2 \cos^2 \alpha}}$$

where  $k_z = k \cos \psi$  is the component of the wave vector in the  $-z$  direction,  $k$  and  $\psi$  are the wave vector and wave normal angle with respect to the  $-z$  axis respectively,  $\omega_H$  is the electron gyrofrequency,  $c$  is the speed of light and  $\alpha$  is the electron pitch angle. With  $v_R$  defined as above in terms of the properties of the medium and the wave, the cyclotron resonant condition can now be expressed simply as

$$v_z \cong v_R .$$

# 4.

## Test Electron Trajectories

When integrated over time the equations of motion derived in the previous chapter determine the velocity space trajectories of individual test electrons interacting with an oblique whistler mode wave. These trajectories and their deviations from the corresponding unperturbed electron trajectories (in the absence of the wave) are the basis of our investigation of the resultant pitch angle scattering and electron precipitation induced by oblique whistler waves. Part of the results reported in this chapter were published in Geophysical Research Letters [*Jasna et al.*, 1992].

### 4.1. Problem Formulation

The interaction between radiation belt electrons and magnetospherically reflected (MR) whistler waves is schematically illustrated in Figure 4.1. We first consider interactions at  $L = 3$ , between electrons with initial equatorial pitch angle in the vicinity of the equatorial loss cone angle ( $\alpha_{eqic} \cong 9^\circ$ ) and a whistler wave propagating at an angle  $\psi$  (assumed constant along the field line) to  $\vec{B}_o$ . The Poynting flux of the wave is assumed to remain constant

during the interaction and is taken to be  $S=8.1 \text{ pW/m}^2$ , corresponding to that of a 10 kHz wave with  $\psi=0^\circ$  and an intensity at the equator at  $L=3$  of  $B_w = 1 \text{ pT}$ . Equatorial electron density at  $L=3$  is assumed to be  $600 \text{ cm}^{-3}$  (see Table 2.1).

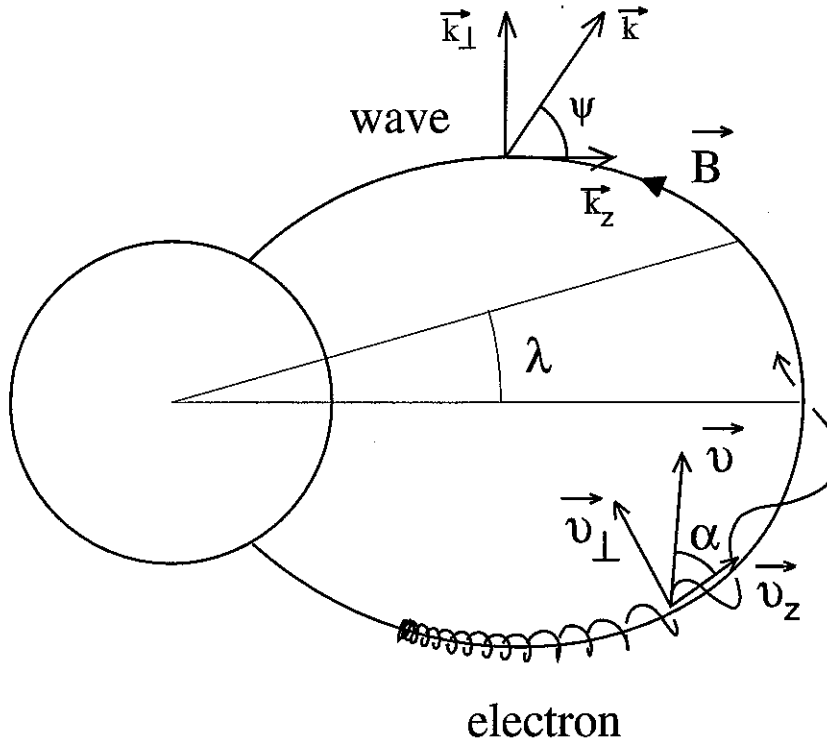


**Figure 4.1. Schematic illustration of the electron-oblique wave interaction.** The motion of radiation belt electrons is fully described by any three independent coordinates that can be derived from the electron velocity  $\vec{v}$ . We use the equatorial pitch angle  $\alpha_{eq}$  and energy  $E$  to initially identify the test particle. The equations of motion are expressed in terms of the velocity  $v_z$  parallel to  $B$ , equatorial pitch angle  $\alpha_{eq}$  and gyrophase  $\eta$ . The position in space is defined by specifying the field line ( $L$ -shell) and geomagnetic latitude  $\lambda$ . The electromagnetic wave is specified by its frequency, wave normal angle  $\psi$  with respect to the  $B$  (which for a given electron density determines the wave vector  $k$ ), and power flux  $S$  (Poynting flux).

Figure 4.2 indicates that gyroresonance with 100 eV electrons can occur at  $L=3$  for wave frequencies up to  $\sim 25 \text{ kHz}$ , although we only consider waves for which  $f < f_{Heq}/2$  or  $f < 16.17 \text{ kHz}$ . Raytracing in typical model

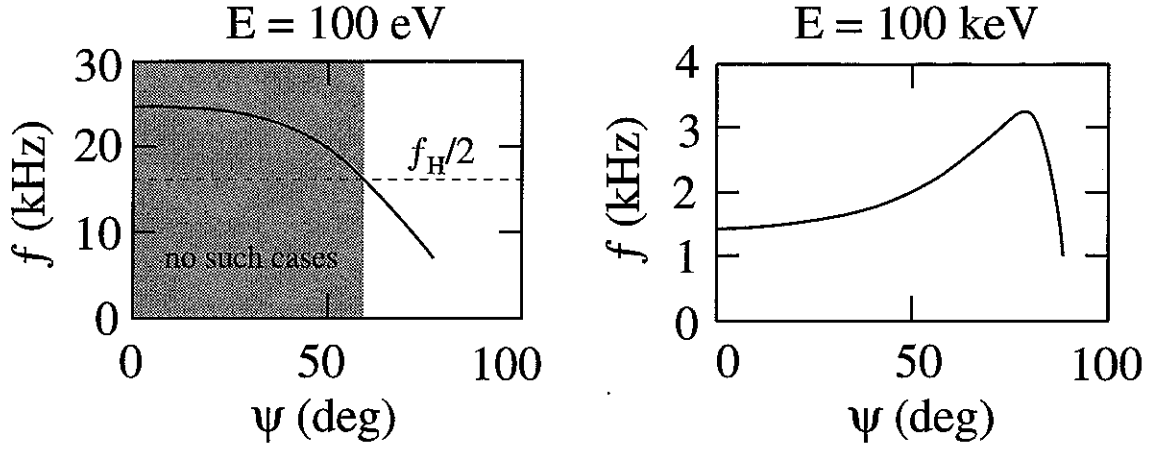


**Figure 4.2.** Dependence of wave frequency on wave normal angle  $\psi$  for equatorial gyroresonance. At  $L = 3$ , in the equatorial plane, the cyclotron resonance condition of  $\dot{\eta} = 0$  requires the dependence of  $f$  on  $\psi$  for 100 eV and 100 keV electrons as shown for electrons with pitch angle of  $\alpha_{eq} = 9^\circ$  (edge of the loss cone).

magnetospheres, such as that shown in Figure 4.3, indicates that for signals originating on the ground (such as VLF transmitter signals and lightning-generated whistlers), which upon entry into the ionosphere have nearly vertical  $\psi$ , the equatorial plane crossings occur at  $L$  such that  $f < f_{H_{eq}}/2$  [Inan and Bell, 1991]. This fact is also consistent with experimental data which indicates that signals from ground-based sources are confined to  $L$ -shells corresponding to  $f < f_{H_{eq}}$  [Bell et al., 1981]. Thus, our analysis here is particularly applicable to interactions involving waves generated on the ground. Note that for 100 keV electrons the frequency of gyroresonant waves for all  $\psi$  is less than 3.25 kHz ( $0.1 f_{H_{eq}}$ ).

The results of Figure 4.2 are used below to determine the wave  $f$  and  $\psi$  for gyroresonance with 100 eV or 100 keV test electrons at the geomagnetic equator at  $L = 3$ .

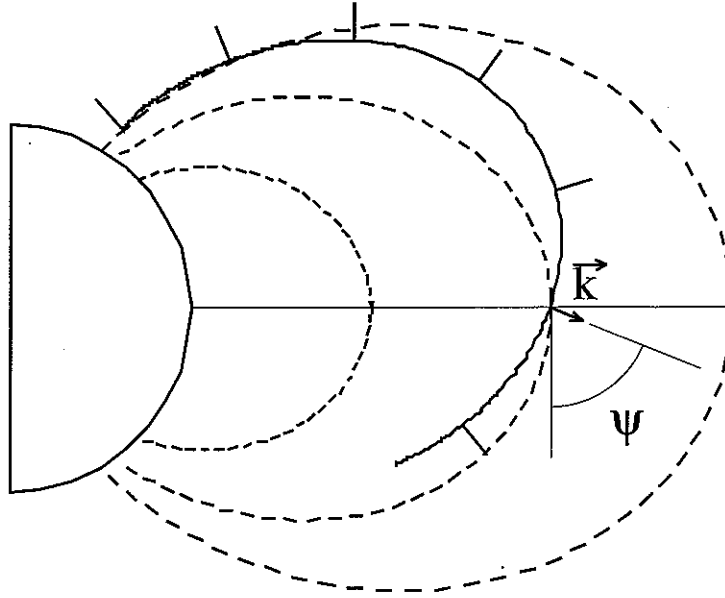


**Figure 4.3. Sample raypath.** A sample raypath in the magnetic meridional plane for a  $f=10.93$  kHz wave injected at 1000 km altitude at  $L=4$ . The wave normal direction is shown along the raypath, and its angle with respect to the magnetic field line is defined at the equatorial crossing as  $\psi$ . In this example,  $\psi \cong 60^\circ$  at the point where the ray crosses the equator.

## 4.2. Test Particle Trajectories

Trajectories of sample equatorially resonant 100 eV and 100 keV test electrons calculated under the conditions described above are shown in Figures 4.4 and 4.5, respectively.

For each  $\alpha_{eq}$  and  $v_{zeq}$  12 different test electrons initially distributed uniformly in Larmor phase are used since we see from Figures 4.4 and 4.5 that the net scattering is strongly dependent on initial phase [Inan *et al.*, 1978].



The variation of the resonant velocity  $v_R$  (see section 3.4) with geomagnetic latitude  $\lambda$  illustrates the inhomogeneity of the medium which ultimately restricts the duration of the interaction. As is evident from Figures 4.4 and 4.5, significant interaction (i.e., significant pitch angle scattering) occurs only when  $v_z \equiv v_R$ . We note that the length of the available interaction region rapidly decreases with increasing  $\psi$ , which is why the net scattering is roughly the same for different  $\psi$ , although the scattering efficiency itself rapidly increases with  $\psi$  for  $\psi \rightarrow \psi_r$ , where  $\psi_r$  is the resonance cone angle [Inan and Bell, 1991].

We use  $\overline{\Delta\alpha_{eqf}}$  to denote the root-mean-square (rms) value of the final pitch angle change at the end of the resonant interaction, namely  $\overline{\Delta\alpha_{eqf}} = \sqrt{\langle \Delta\alpha_{eq}^2(\lambda_f) \rangle}$ , where the ensemble averaging ( $\langle \rangle$ ) is over the 12 test particles.

For 100 eV electrons (Figure 4.4)  $\overline{\Delta\alpha_{eqf}}$  slightly decreases with increasing  $\psi$  being  $\overline{\Delta\alpha_{eqf}} = 0.2797^\circ$  for  $\psi = 60^\circ$  and  $0.1997^\circ$  for  $\psi = 80^\circ$ . For 100 keV electrons (Figure 4.5) we see a more rapid dependence on  $\psi$  with  $\overline{\Delta\alpha_{eqf}} = 0.0107^\circ$  for  $\psi = 0^\circ$  (parallel propagation), while  $\overline{\Delta\alpha_{eqf}} = 0.0039^\circ$  for  $\psi = 80^\circ$  (highly oblique propagation).

Comparison of  $\overline{\Delta\alpha_{eqf}}$  for 100 eV and 100 keV electrons shows that, for the parameters considered here, equatorial pitch angle scattering of suprathermal electrons by oblique waves produces higher scattering than even the most efficient scattering of 100 keV electrons by a wave with  $\psi = 0^\circ$  and the same Poynting flux. We note that the scattering of energetic electrons by parallel propagating waves at  $L \equiv 3$  has been extensively studied [e.g., Chang and Inan, 1985] and that electron fluxes have been measured on satellites [Voss *et al.*, 1984], and rockets [Goldberg *et al.*, 1986]. Thus, a preliminary estimate of precipitation fluxes of suprathermal electrons can be obtained by means of comparisons of scattering of 100 eV and 100 keV electrons as shown in Figures 4.4 and 4.5. We undertake such a comparison in the next section.

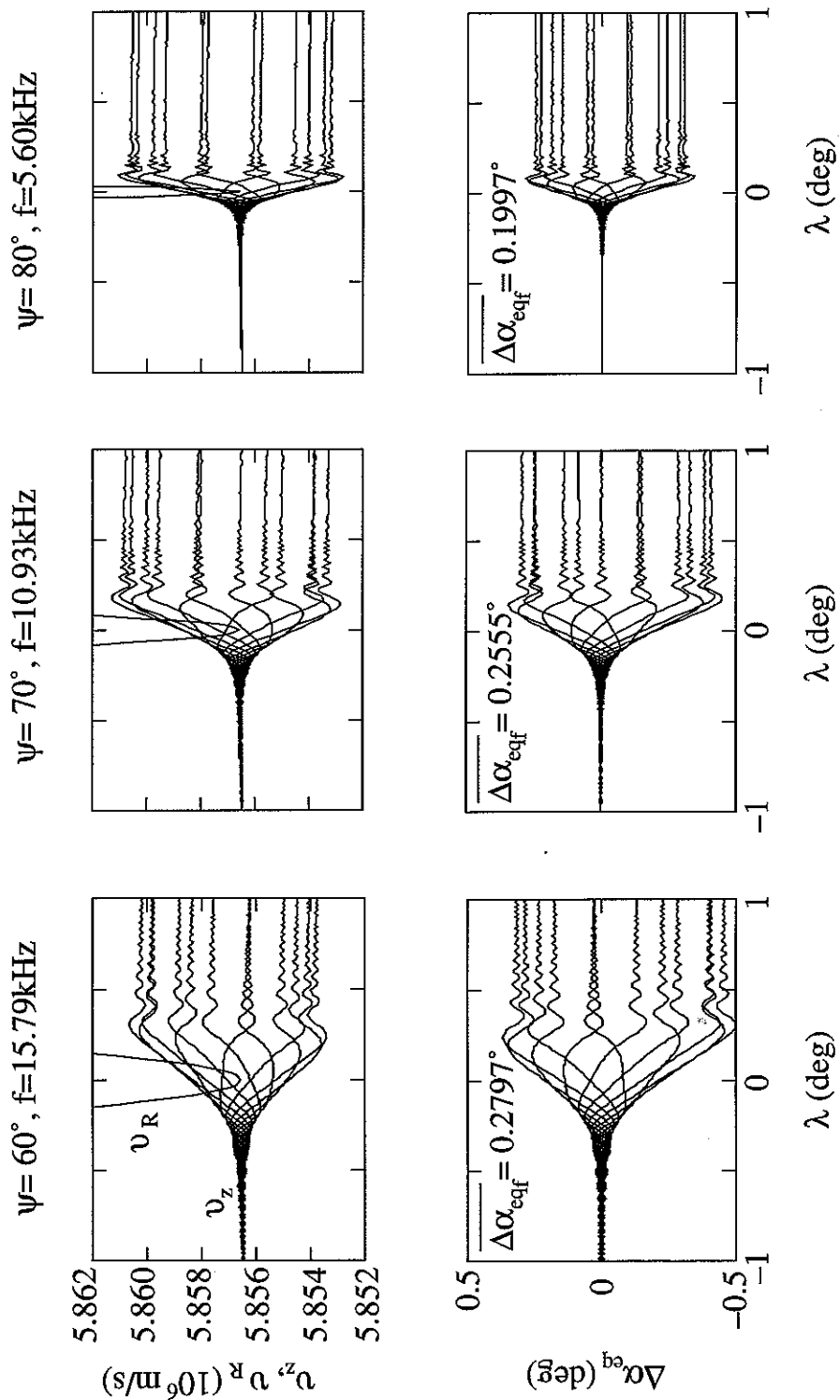


**Figure 4.4. (Previous page) Sample trajectories of suprathermal ( $E=100$  eV) electrons.** Trajectories of  $E=100$  eV electrons interacting at  $L=3$  with waves having a power density of  $S=8.1$  pW/cm<sup>2</sup> and three different wave normal angles  $\psi=60^\circ, 70^\circ, 80^\circ$  with the corresponding equatorial resonance frequencies  $f=15.79$  kHz, 10.93 kHz, 5.60 kHz (Figure 4.2). The trajectories are shown as plots versus geomagnetic latitude ( $\lambda$ ) of the electron's velocity parallel to the Earth's magnetic field  $v_z$  and equatorial pitch angle change  $\Delta\alpha_{eq}$ , for 12 test electrons with different, equally spaced initial gyrophases  $\eta(\lambda_i) = n\pi/6$ , ( $n=1,2,\dots,12$ ).  $\overline{\Delta\alpha_{eqf}}$  is the root-mean-square value of the final pitch angle change at the end of the resonant interaction, namely  $\overline{\Delta\alpha_{eqf}} = \sqrt{\langle \Delta\alpha_{eq}^2(\lambda_f) \rangle}$ , where the ensemble averaging ( $\langle \rangle$ ) is over the 12 test particles. In the absence of a perturbing wave,  $v_z$  follows an adiabatic variation while  $\Delta\alpha_{eq}$  remains zero.  $v_R$  is the resonant velocity defined by  $v_R = (\omega_H \sqrt{1 - (v/c)^2} - \omega) k_z^{-1}$  and is shown on the same graph with  $v_z(\lambda)$  for easy assessment of the resonant condition  $v_z \equiv v_R$ .

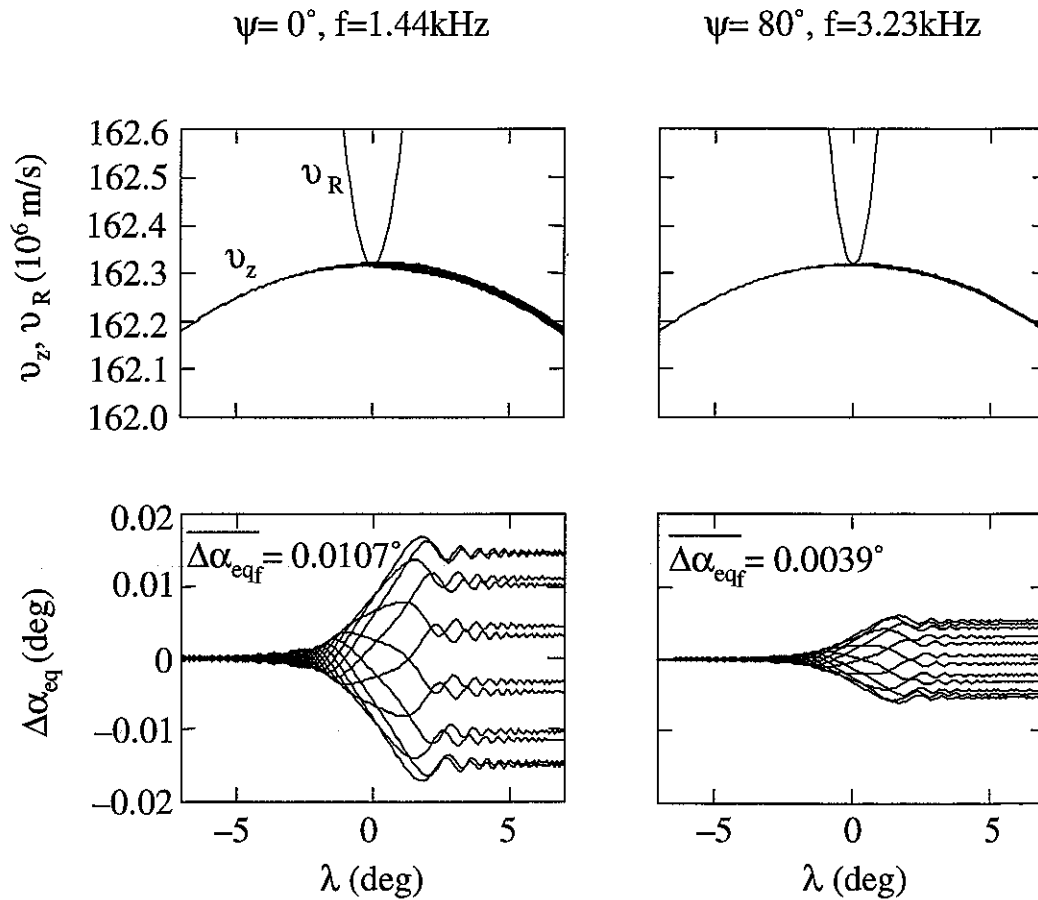


**Figure 4.5. Sample trajectories of energetic ( $E=100$  keV) electrons.** The format is identical to that of Figure 4.4.

### 4.3. Precipitation Energy Flux Estimates

We use the results obtained above to comparatively estimate differential energy fluxes for 100 eV and 100 keV electrons, pitch angle scattered by parallel propagating or oblique waves. The differential scattered energy flux  $dQ$  is proportional to (section 5.1.2)

$$dQ \propto E v_z^3 f(E) dv_z d\alpha_{eq}$$

where  $f(E)$  is the electron distribution function,  $E$  is the electron energy and units of  $dQ$  are ergs/cm<sup>2</sup>-s. Based on experimental data [Schield and Frank, 1970] a typical electron distribution function at  $L = 3$  can be taken to be

$$f(E) \propto E^{-m} \text{ where } 2.5 \leq m \leq 3$$

To compare the ratio of  $dQ$  for 100 eV electrons precipitated by an oblique ( $\psi=60^\circ$ ) wave to that for 100 keV electrons precipitated by a ducted ( $\psi=0^\circ$ ) wave, we use  $\overline{\Delta\alpha_{eqf}}$  for  $d\alpha_{eq}$ . To estimate  $dv_z$ , test particle simulations were used to determine  $\overline{\Delta\alpha_{eqf}}$  for different initial  $v_{zeq}$  as shown in Figures 4.6 and 4.7 respectively for 100 eV and 100 keV. Using the velocities corresponding to peak  $\overline{\Delta\alpha_{eqf}}$  as  $v_z$ , and  $dv_z$  as determined by a 10% reduction in  $\overline{\Delta\alpha_{eqf}}$  on both sides of the peak in the expression for  $dQ$ , we find:

$$1 \leq \frac{dQ(E = 100 \text{ eV}, \psi = 60^\circ)}{dQ(E = 100 \text{ keV}, \psi = 0^\circ)} \leq 34$$

It thus appears that, at  $L=3$ , the differential precipitated energy flux of 100 eV electrons precipitated by an oblique wave would be higher than that of 100 keV electrons precipitated by parallel propagating waves.

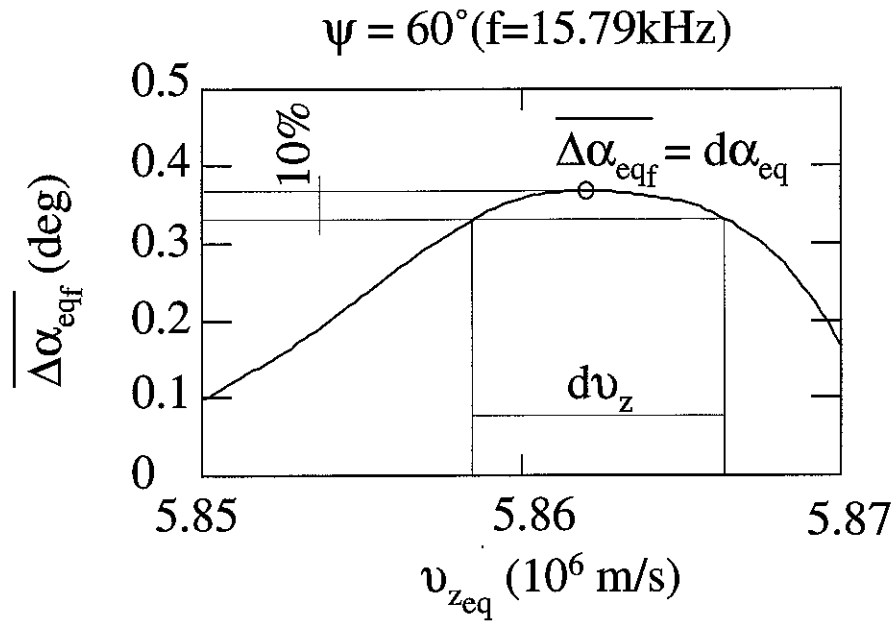


**Figure 4.6. Dependence of electron scattering on initial electron velocity for suprathermal ( $E=100$  eV) electrons.** Ensemble averaged scattering of 12 test particles with the same initial  $v_{zeq}$  as a function of  $v_{zeq}$  for suprathermal (100 eV) electrons. The result shown is for test electrons with initial equatorial pitch angle  $\alpha_{eq}=9^\circ$  and energy  $\sim 100$  eV interacting with a wave with  $\psi=60^\circ$ ,  $f=15.79$  kHz, and  $S=8.1$  pW/cm<sup>2</sup>.

To put this result in perspective, we note that lightning-induced electron precipitation bursts have been measured to have peak flux levels of  $10^{-3}$ – $10^{-2}$  ergs/cm<sup>2</sup>-s [Voss *et al.*, 1984], consistent with the ionospheric disturbances produced by such bursts [Inan *et al.*, 1985a]. On this basis, we can expect lightning-induced whistlers propagating in the oblique mode to precipitate fluxes of  $> 10^{-2}$  ergs/cm<sup>2</sup>-s of  $\sim 100$  eV electrons. Note that the power density in an oblique wave may be expected to be lower, but in terms of the overall contribution to the radiation belt loss, this effect would be compensated by the illumination of much larger spatial regions by non-ducted waves.

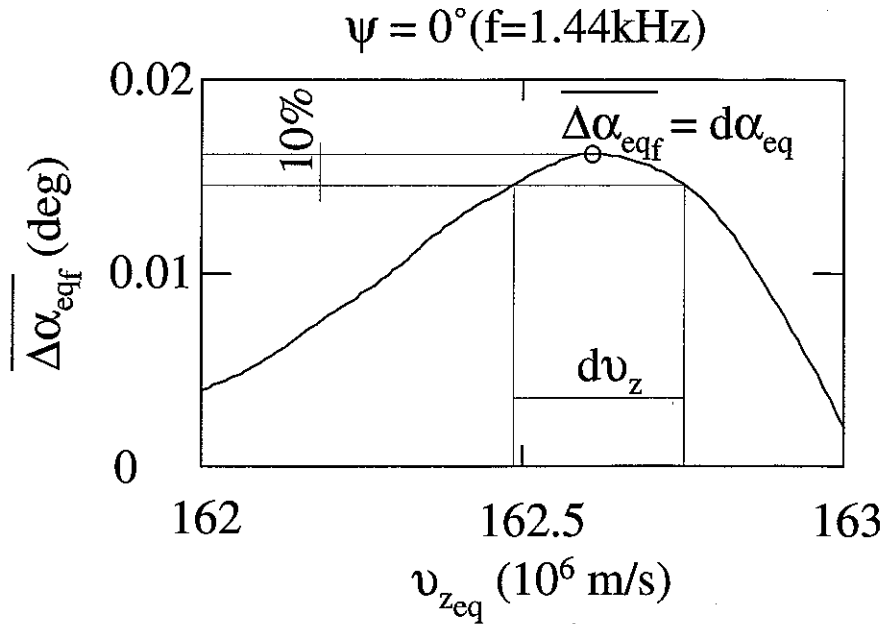


**Figure 4.7. Dependence of electron scattering on initial electron velocity for energetic ( $E=100$  keV) electrons. Same as Figure 4.6 but for energetic (100 keV) electrons.**

## 4.4. Conclusions

Our results indicate that on typical mid-latitude field lines (e.g.,  $L \approx 3$ ), pitch angle changes of 100 eV electrons gyroresonantly scattered by highly oblique whistler-mode waves are generally higher than those of 100 keV electrons scattered by parallel propagating waves having the same power density. Estimates indicate that precipitated energy fluxes resulting from such interactions can be up to 30 times larger than those due to the precipitation of 100 keV electrons, which are commonly observed in ground based experiments by means of their effects in the lower ionosphere. In view of the omnipresence of highly oblique magnetospherically reflected waves at mid

latitudes [*Edgar*, 1976], it appears that lightning-induced whistler wave energy can precipitate substantial fluxes of 100 eV electrons which would be deposited at 200–300 km altitude and produce secondary ionization enhancements. In view of the relatively large scale heights at such altitudes, the upward field-aligned diffusion from such ionization enhancements can contribute to the formation of whistler-mode ‘ducts’ as suggested by *Inan and Bell* [1991].





## **5.**

### **The Interaction Between an Oblique Whistler-Mode Wave and a Full Distribution of Electrons**

The test particle trajectories illustrate the detailed dynamics of the electron-wave interaction and the resultant electron pitch angle and velocity scattering as well as the duration of the interaction and its dependence on electron and wave input parameters (initial electron velocity, wave frequency and wave normal angle). However, full distribution modeling is required to assess the effects of the oblique whistler-electron interactions on the radiation belt electron population and to quantitatively evaluate these resulting effects in terms of measurable quantities such as precipitated electron fluxes and lifetimes. The development and application of a test particle model of the interaction between oblique whistler mode waves and a full distribution of radiation belt electrons is the subject of this chapter.

## 5.1. Theoretical Introduction

### 5.1.1. Electron Velocity Space

In general, electron velocity space is three dimensional. For the special case of electron motion in the Earth's magnetosphere, important features of the unperturbed particle motion can be described by only two velocity space coordinates, for example the equatorial pitch angle  $\alpha_{eq}$  and the component of the particle velocity along the Earth's magnetic field line  $v_{zeq}$ . We represent the full distribution function by a large number of individual test particles and infer the modification of the distribution from the simulated trajectories of each of the test particles in the presence of the wave. Once a new particle distribution is determined, measurable quantities such as differential (per unit particle energy) and total precipitated particle fluxes and radiation belt electron lifetimes\*, are easily derived.

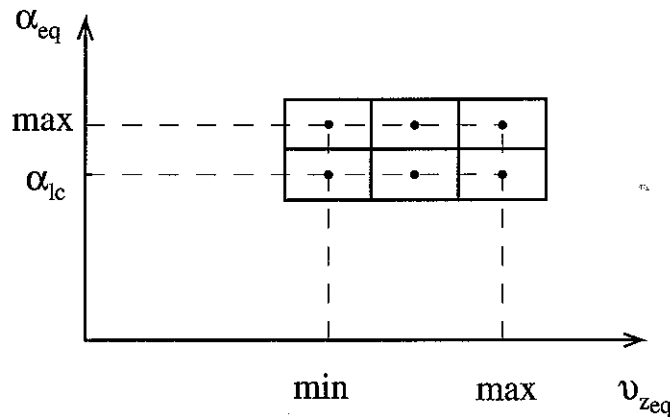


**Figure 5.1. Velocity space cells.** The portion of velocity space that is simulated is divided into cells each of which is to be represented by test particles.

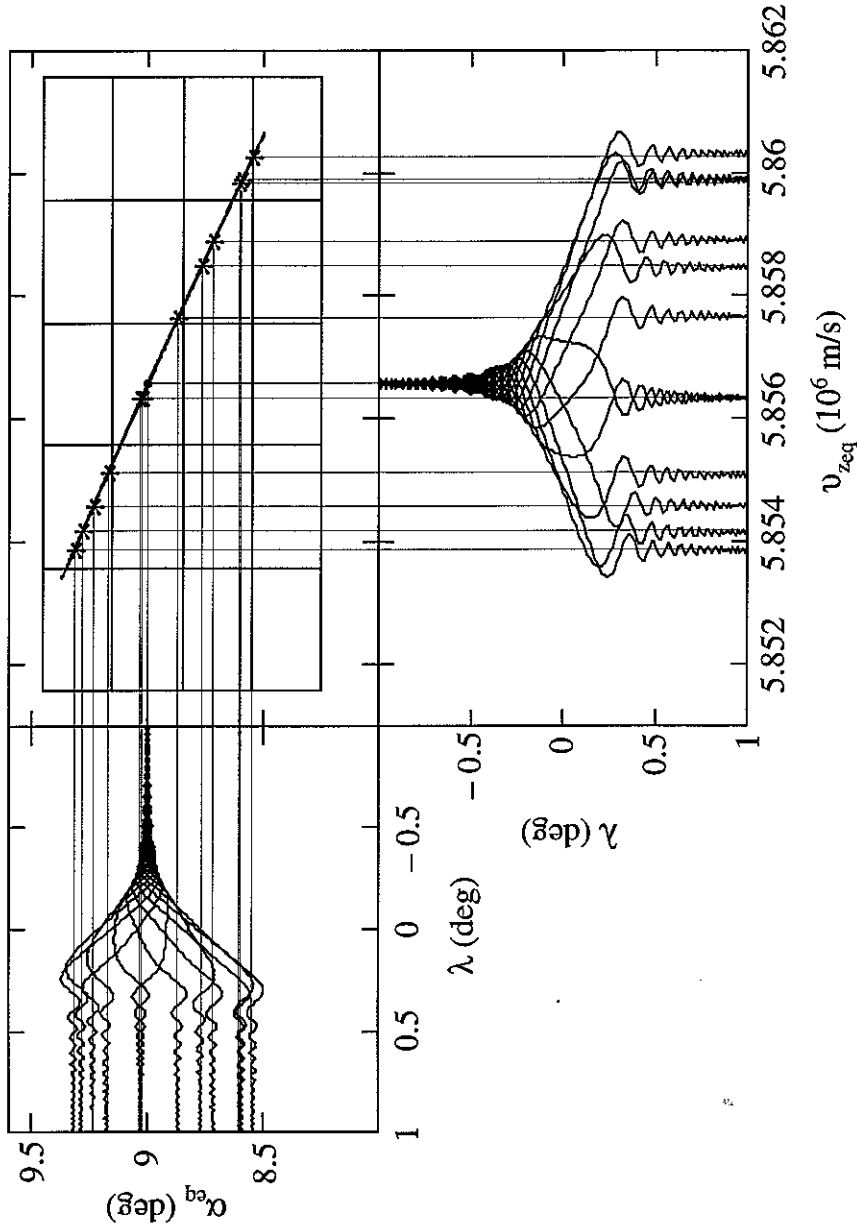
\* Subject to certain assumptions as discussed below

Figure 5.1. shows  $\alpha_{eq} - v_{z_{eq}}$  velocity space divided into cells. Note that in the absence of the wave, the trajectory of a test electron moving in the Earth's magnetic field would be a single point in  $\alpha_{eq} - v_{z_{eq}}$  space. Due to the interaction with the wave, the electron trajectory in velocity space evolves along a curve with initial and final points corresponding to the initial and final velocity space coordinates. Since the wave forces acting on the particle are functions of the initial electron phase  $\eta$  (the third velocity coordinate that determines the direction of the electron velocity perpendicular to the Earth's magnetic field) as shown in Chapter 3, electron trajectories and their final points in velocity space depend on the initial  $\eta$  (Chapter 4). Figure 5.2 shows twelve different electron trajectories corresponding to 12 electrons with different initial phases, originating at the same initial point in velocity space (i.e., having the same initial  $\alpha_{eq}$  and  $v_{z_{eq}}$ ). In view of this dependence of scattering on  $\eta$ , each cell in velocity space needs to be represented by a distribution of several test electrons with different initial phases. We choose 12 test electrons equally spaced in phase to represent a given cell based on the fact that the pitch angle change  $\overline{\Delta\alpha_{eqf}}$  (as introduced in Chapter 4) does not change significantly with further increase of the number of test electrons representing each cell. This choice of 12 test electrons limits the accuracy\* of our calculations to  $10^{-5}^\circ$ , well sufficient for our purposes here.

Since the goal of our study is to determine the modification of the electron distribution function in a single encounter with the wave (i.e., one pass) rather than the evolution of the distribution function with time during the interaction, and since we neglect the effects of the energetic particles on the wave, the initial and final points of the electron trajectory in velocity space determine the pitch angle scattering and the resultant change in the electron distribution function. Figure 5.3. shows the scattering of a single test electron in terms of the initial and final points in  $v_{z_{eq}} - \alpha_{eq}$  space. The initial population of electrons as represented by any such test electron is then distributed into the four adjoining cells in proportion to the overlapping fractional area of the final cell.

---

\* The precision by which we can specify  $\overline{\Delta\alpha_{eqf}}$



**Figure 5.2. Test electron trajectories in the velocity space.** Trajectories of the twelve test electrons with different initial phases, originating at the same initial point in velocity space are represented in velocity space as  $\alpha_{eq}(v_{z,eq})$  and as the velocity space coordinates dependence on geomagnetic latitude namely  $\alpha_{eq}(\lambda)$  and  $v_{z,eq}(\lambda)$ .

In other words, the fraction of the total number of electrons which populated the initial cell but which are scattered into any of the four cells adjoining the final point in  $v_{zeq} - \alpha_{eq}$  space is proportional to the area of the final cell, centered at the final point in  $v_{zeq} - \alpha_{eq}$  space, that overlaps each adjoining cell.

The modified electron distribution after a one-pass interaction with the wave is obtained using the scattering of all test electrons as described by the sample electron in Figure 5.3, weighed by the initial distribution function (electron density per velocity space volume) and its dependence on the velocity space coordinates [i.e.,  $f(v_{zeq}, \alpha_{eq})$ ].

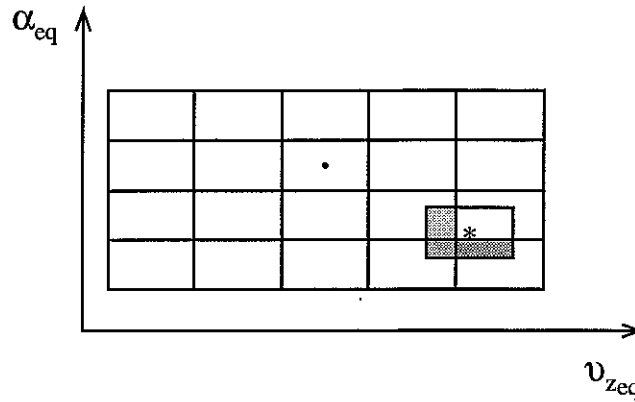


**Figure 5.3. A single test electron scattering in velocity space.** The schematic shows the initial and final points of the test electron trajectory in the velocity space. Electron population from the initial cell represented by the test electron is scattered into the four adjoining cells as represented by the cell corresponding to final point on the electron trajectory. The number of electrons scattered into any of the four adjoining phase cells is proportional to the area of the final cell that overlaps the corresponding cell.

For our formulation, we have found it useful to represent the electron trajectory in terms of velocity space coordinates  $v_{zeq}$  and  $\alpha_{eq}$ . However, because these coordinates (especially  $v_{zeq}$ ) are not as convenient for depicting the electron distribution function, we transform the resulting distribution to express it in terms of total electron energy  $E$  and  $\alpha_{eq}$ . Figure 5.4 shows the

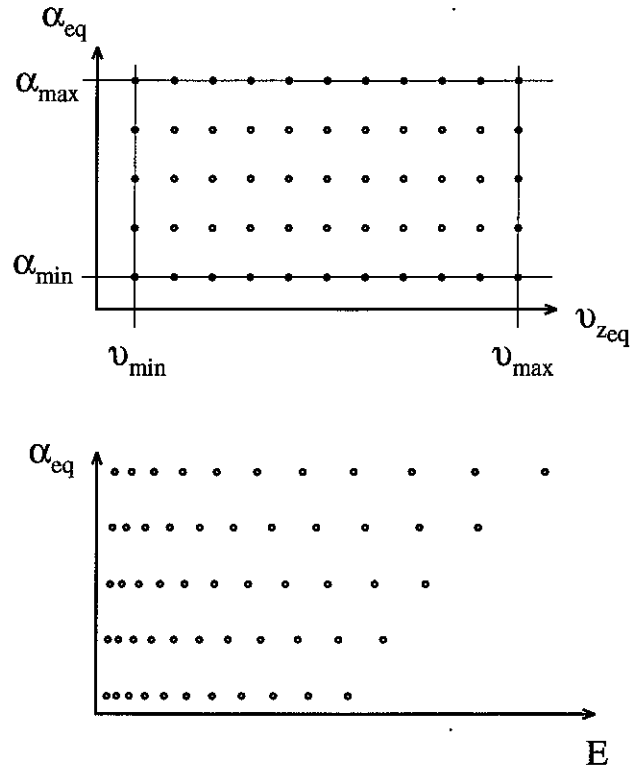


**Figure 5.4. Coordinate transformation.** Transformation of the velocity space distribution from  $v_{zeq} - \alpha_{eq}$  to  $E - \alpha_{eq}$  coordinates.

transformation of a uniform grid in the  $v_{zeq} - \alpha_{eq}$  space into the corresponding  $E - \alpha_{eq}$  grid, whose cell size  $\Delta E$  depends\* on both  $\alpha_{eq}$  and  $E$  (i.e.  $v_{zeq}$ ). The next step, i.e., the transformation to a uniform grid in  $E - \alpha_{eq}$  space is shown in Figure 5.5. The value of the distribution function at each of the uniform grid points was calculated by linear interpolation of the values of the distribution function in the adjacent non-uniform grid points with the same  $\alpha_{eq}$ .

---


$$* \Delta E = m_e \frac{v_{zeq}}{\cos^2 \alpha_{eq}} \left( 1 - \frac{v_{zeq}^2}{c^2 \cos^2 \alpha_{eq}} \right)^{-3/2} \Delta v_{zeq}$$

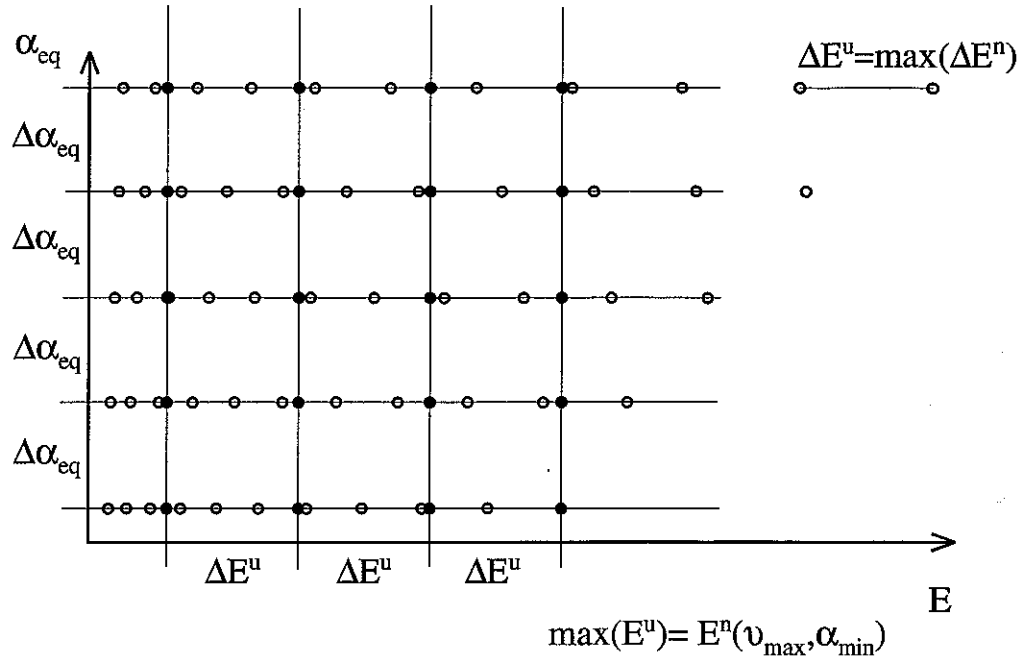


**Figure 5.5. Velocity space grid transformation.** Transformation of velocity space description from a non-uniform (filled circles and superscript n) to uniform (empty circles and superscript u) grid.

### 5.1.2. Particle and Energy Fluxes

The relationship between the particle distribution function  $f(v_z, \alpha)$  and differential energy spectrum  $\Phi_{E_{diff}}(E, \alpha)$  can be written as (see, for example, Chang, [1983], Appendix A)

$$\Phi_{E_{diff}}(E, \alpha) = f(v_z, \alpha) \frac{v_z^2}{\cos^2 \alpha} \frac{1}{m_e} \left( \sqrt{1 - \frac{v_z^2}{c^2 \cos^2 \alpha}} \right)^3 \quad 5.1.$$

To find the differential energy spectrum at pitch angles below the loss cone (i.e., to be precipitated) at the equator we integrate

$$\Phi_{E_{preeq}}(E) = \int_{\theta=0}^{2\pi} \int_{\alpha_{eq}=0}^{\alpha_{lc}} \Phi_{E_{diff}}(E, \alpha_{eq}) \underbrace{\cos \alpha_{eq}}_{\text{adjustment to the area } \perp \text{ to } B_0} \underbrace{\sin \alpha_{eq} d\alpha_{eq} d\theta}_{\text{solid angle } d\Omega}$$

At atmospheric altitudes the reduction of the flux tube volume element needs to be taken into account so that the precipitated differential energy spectrum becomes

$$\Phi_{E_{prec}}(E) = \pi \underbrace{\frac{\sqrt{1+3\sin^2 \lambda_{at}}}{\cos^6 \lambda_{at}}}_{\text{flux tube volume reduction factor for dipole field}} \int_{\alpha_{eq}=0}^{\alpha_{lc}} \Phi_{E_{diff}}(E, \alpha_{eq}) \sin(2\alpha_{eq}) d\alpha_{eq}$$

The precipitated differential energy flux is defined as

$$dQ = E \Phi_{E_{prec}}(E) dE$$

and the total precipitated energy flux can be found

$$Q = \int_E E \Phi_{E_{prec}}(E) dE$$

or as derived in *Chang*, [1983]

$$Q = 2\pi \frac{\sqrt{1+3\sin^2 \lambda_{at}}}{\cos^6 \lambda_{at}} \int_{v_{zeq}} \int_{\alpha_{eq}=0}^{\alpha_{lc}} E f(v_{zeq}, \alpha_{eq}) v_{zeq}^3 \frac{\sin \alpha_{eq}}{\cos^3 \alpha_{eq}} d\alpha_{eq} dv_{zeq}$$

The equations derived above are expressed in SI units and should be multiplied with the appropriate scaling factor for use with variables expressed in different units. For comparison purposes the units of the variables defined and used in both SI units and most commonly used units are given in Table 5.1, together with the conversion factor that the quantity in SI units should be multiplied with to get the corresponding value of the quantity in the more common units.



**Table 5.1. Dimensions of various quantities**

	SI units	common units	conversion factor
$f$	$\frac{el}{\left(\frac{m}{s}\right)^3 m^3}$	$\frac{el}{\left(\frac{m}{s}\right)^3 cm^3}$	$10^{-6}$
$\Phi_{E_{diff}}(E, \alpha)$	$\frac{el}{m^2 s J ster}$	$\frac{el}{cm^2 s keV ster}$	$1.6 \times 10^{-20}$
$\Phi_{E_{prec}}(E)$	$\frac{el}{m^2 s J}$	$\frac{el}{cm^2 s keV}$	$1.6 \times 10^{-20}$
$Q$	$\frac{J}{m^2 s}$	$\frac{erg}{cm^2 s}$	$10^3$

### 5.1.3. Particle Lifetimes

The precipitated differential energy spectrum  $\Phi_{E_{prec}}(E)$  can be used to infer the electron lifetimes in a given magnetic flux tube subject to certain assumptions as discussed below. We note in this context that the precipitated differential energy spectrum may change as a function of time both because of temporal variations of the electron distribution function, and gradient and curvature drifts, or because of variations in the parameters of the wave interacting with the electrons. For the purpose of estimating electron lifetimes  $\tau(E)$ , we assume that the precipitated differential energy spectrum remains constant in time, i.e.,

$$\Phi_{E_{prec}}(E, t) \equiv \Phi_{E_{prec}}(E)$$

We define  $N_f$  as the number of energetic electrons with a given energy per unit energy in a flux tube, per unit area of a tube cross section, at the equator so that the SI unit of the variable  $N_f$  is el/m<sup>2</sup>-J. We assume that  $N_f$  decays exponentially in time as a result of the resonant scattering due to the electron-wave interaction

$$N_f(E, t) = N_f(E) e^{-\frac{t}{\tau(E)}}$$

while

$$\frac{\partial N_f(E, t)}{\partial t} = -\Phi_{E_{prec}}(E, t) = -\Phi_{E_{prec}}(E)$$

so that the lifetime of the electrons in a given tube is

$$\tau(E) = \frac{N_f(E)}{\Phi_{E_{prec}}(E)}$$

The number of energetic electrons of a given energy per unit energy in a tube can be expressed as an integral

$$N_f(E) = \int_{\lambda=-\lambda_{at}}^{\lambda_{at}} \int_{\alpha=\alpha_{lc}(\lambda)}^{\pi/2} \int_{\theta=0}^{2\pi} \frac{dN(\lambda)}{dE dA} = 2 \int_{\lambda=0}^{\lambda_{at}} \int_{\alpha_{eq}=\alpha_{lc}}^{\alpha_{max}(\lambda)} \int_{\theta=0}^{2\pi} \frac{dN_{eq}(\lambda)}{dE dA}$$

Figure 5.6 shows mapping of a distribution of electrons with pitch angles between local loss cone angle  $\alpha_{lc}$  and 90° at any given geomagnetic latitude  $\lambda$  along the field line to the corresponding distribution at the geomagnetic equator. Using

$$dN_{eq}(\lambda) = f(E, \alpha) \underbrace{v^2 \frac{dv}{dE} dE \sin \alpha d\alpha d\theta}_{\text{velocity phase space volume element}} \underbrace{\frac{dz}{d\lambda} d\lambda dA}_{\text{volume element}}$$

where

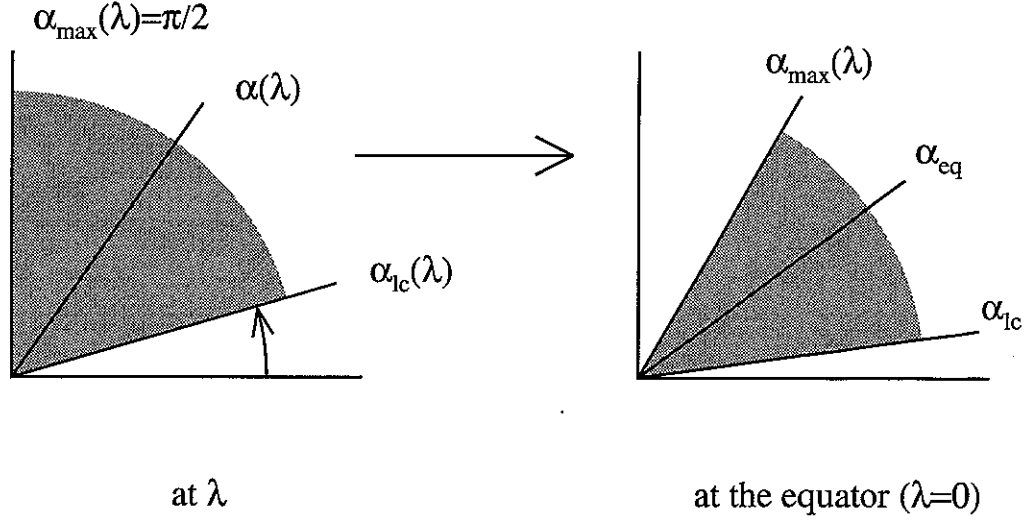


**Figure 5.6. Mapping of the pitch angle distribution.** Mapping of a pitch angle distribution of electrons at any geomagnetic latitude  $\lambda$  to the corresponding distribution at the equator.

$$v^2 \frac{dv}{dE} = \frac{c}{m_e} \sqrt{1 - \frac{1}{\left(1 + \frac{E}{m_e c^2}\right)^2}} \left(1 + \frac{E}{m_e c^2}\right)^{-3}$$

and

$$\frac{dz}{d\lambda} = LR_e \cos \lambda \sqrt{1 + 3 \sin^2 \lambda}$$

the differential energetic electron density in a tube  $N_f$  can be expressed as

$$N_f(E) = C \int_{\lambda=0}^{\lambda_{at}} \cos \lambda \sqrt{1 + 3 \sin^2 \lambda} \left( \int_{\alpha_{eq}=\alpha_{lc}}^{\alpha_{\max}(\lambda)} f(E, \alpha_{eq}) \sin \alpha d\alpha \right) d\lambda$$

where

$$C = \frac{4\pi LR_e c}{m_e} \sqrt{1 - \frac{1}{\left(1 + \frac{E}{m_e c^2}\right)^2}} \left(1 + \frac{E}{m_e c^2}\right)^{-3}$$

Note that the electron lifetimes defined above are derived for the electron population confined to a narrow flux tube around the field line where the interaction takes place. The extent to which this loss process contributes to the electron lifetimes on a global scale depends on the extent of magnetospheric regions illuminated by the waves, since similar scattering processes would be expected in all regions where the oblique waves are present. Experimental data indicates that magnetospheric regions illuminated by whistlers from a given thunderstorm center may extend to many tens of degrees in longitude around that of the storm center [Sonwalkar and Inan, 1993].

## 5.2. Initial Conditions and Assumptions

### 5.2.1. Initial Electron Distribution Function

We describe the initial electron distribution function in a manner similar to that of *Inan et al.* [1978] and *Chang and Inan* [1985]. We assume that radiation belt electrons are uniformly distributed in the electron pitch angle space between  $\alpha_{lc}$  and  $\pi/2$  and with an energy dependence of the form

$$f_E(E) \propto E^{-3}$$

based on the experimental data [Schield and Frank, 1970]. We can alternatively express the distribution in terms of the electron velocity

$$f_v(v) = \frac{A}{v^6}$$

Since the energetic electron population is commonly described and measured in terms of the differential energy spectrum  $\Phi_{E_{diff}}(E)$ , the constant  $A$  in the above expression is chosen such that the corresponding differential energy spectrum at  $E = 1$  keV is

$$\Phi_{E_{diff}}(1\text{keV}) = 10^8 \frac{el}{\text{cm}^2 \text{s keV ster}}$$

Using Equation 5.1 the corresponding value of the constant  $A$  is found to be

$$A = 7.034 \times 10^{26} \frac{el}{\text{s}^3 \text{ster}}$$

### 5.2.2. Assumptions Concerning the Resonant Wave

One of the fundamental assumptions of our test particle formulation is the fact that we neglect the effects on the wave of the distribution of energetic electrons. This means that we are assuming either that the currents stimulated in the particle population do not lead to significant damping or amplification of the wave or that this effect has been included in the model chosen for the wave structure. This approximation was also adopted in the test particle model studies of ducted wave-particle interactions [Inan *et al.*, 1982; Chang and Inan, 1985]. For ducted waves, wave growth is commonly observed to occur [e.g., Helliwell, 1988]; however, experimental and theoretical evidence suggest that the region of temporal growth of the wave is within a few degrees of the geomagnetic equator [Helliwell, 1967; Helliwell and Katsufakis, 1974; Tsurutani and Smith, 1974; Carlson *et al.*, 1990]. Since the change in the wave amplitude structure occurs over a relatively small portion of the field line the effect of such non-uniform amplitude variation on the total precipitated flux is likely to be negligible. In the context of this assumption, it is only necessary to define the wave characteristics as an input

to the test particle code. For non-ducted obliquely propagating waves, taking the wave as a predefined structure and neglecting the effects of the energetic particles on the wave is probably an even better approximation, since growth and emission triggering by non-ducted waves is observed much less often [Bell *et al.*, 1981].

In our modeling, then, we assume the wave to be monochromatic (single frequency), and propagating at a given angle  $\psi$  with respect to the magnetic field. With the wave frequency  $\omega$  and wave normal angle  $\psi$  specified, all properties of the wave are defined in terms of the local cold plasma parameters, as was discussed in section 3.2. The Poynting flux (power density) of the slowly varying wave was also assumed to be constant during its interaction with the radiation belt electrons, although the wave normal angle  $\psi$  was allowed to slowly vary with latitude as dictated by raytracing. The expression for the Poynting flux given in Chapter 3 (Eq. 3.2) was used to calculate the wave field components at different points along the field line.

### 5.3. Comparison of Precipitated Energy Fluxes for Suprathermal and Energetic Electrons

Using the full distribution simulation model described above, it is now possible to refine our first approximation estimates (section 4.3) of the precipitated differential energy fluxes for  $E = 100$  eV and  $E = 100$  keV electrons due to their resonant interaction with the oblique ( $\psi = 60^\circ$ ,  $f = 15.79$  kHz) and ducted ( $\psi = 0^\circ$ ,  $f = 1.44$  kHz) waves respectively at  $L = 3$ . Note that our previous analysis (section 4.3) was based on the scattering of electrons in a very narrow range of  $v_{z_{eq}}$  and thus constitutes a crude first estimate.

The background equatorial cold plasma electron density was taken to be 600 el/cm<sup>3</sup> (Table 2.1). The wave Poynting flux was again taken to be  $S = 8.1$  pW/m<sup>2</sup>, corresponding to that of a parallel propagating ( $\psi = 0^\circ$ )  $f = 10$  kHz wave at  $L = 3$  in the equatorial plane with a magnetic field of  $B_w = 1$  pT.

Figure 5.7 shows a region in velocity space that is divided into  $30 \times 50$  cells each of which is represented by twelve test electrons equally spaced in Larmor phase. As a result of a one-pass (i.e., single encounter) resonant interaction with the wave, these test electrons are scattered in pitch angle and velocity and move to different locations in velocity space (also shown in Figure 5.7). The example shown is for  $E \cong 100$  keV electrons with pitch angles close to the loss cone angle. The initial area in velocity space sampled by the test electrons and the cell sizes are defined as

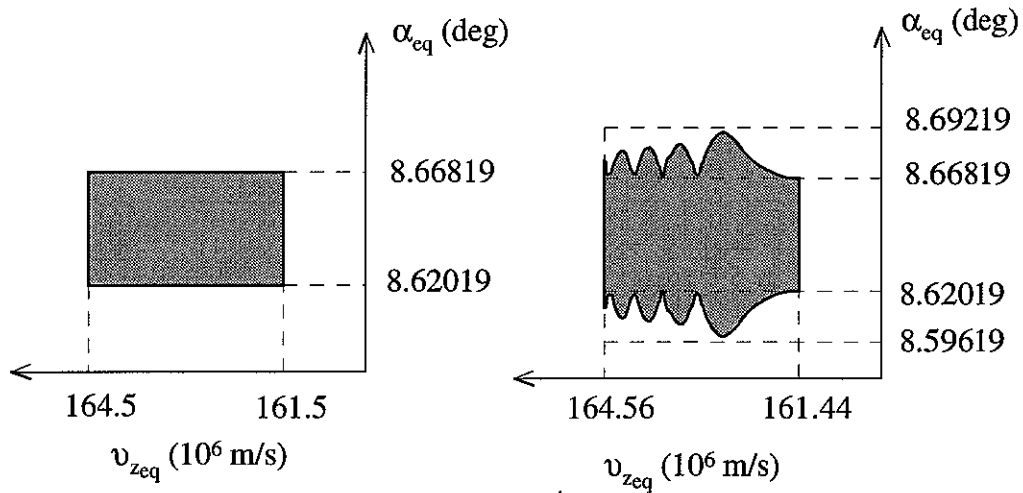


**Figure 5.7. Modification of the velocity space area.** The initial rectangular area of near-loss-cone electrons with  $E \cong 100$  keV represents the ensemble of electrons resonantly interacting with 1.44 kHz ducted ( $\psi = 0^\circ$ ) whistler mode wave. After a one-pass interaction (single encounter) the ensemble occupies a larger area due to electron scattering. The electron scattering into the loss cone ( $\alpha_{eq} < 8.62019^\circ$ ) depends on  $v_{zeq}$  and, for this example, has four maxima and minima as shown. The change in  $\min(v_{zeq})$  and  $\max(v_{zeq})$  is relatively small on the scale shown.

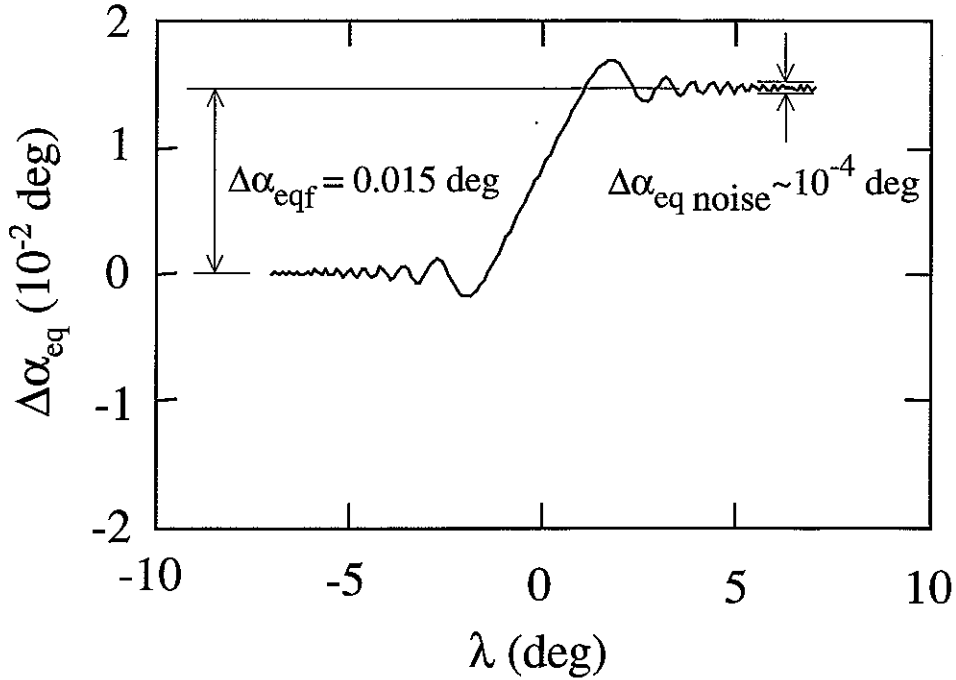
$$v_{z_{eq}} \in [161.5, 164.5] \times 10^6 \frac{m}{s}, \quad \Delta v_{z_{eq}} = 0.06 \times 10^6 \frac{m}{s}$$

$$\alpha_{eq} \in [8.62019^\circ, 8.66819^\circ], \quad \Delta \alpha_{eq} = 0.0016^\circ$$

The range of the velocity space region and the size of the velocity space bins were determined on the basis of test trajectories similar to those given in Chapter 4. The dependence of the rms value of the final pitch angle change  $\overline{\Delta \alpha_{eq_f}} = \sqrt{\langle \Delta \alpha_{eq}^2(\lambda_f) \rangle}$  as defined in Chapter 4, on the initial velocity  $v_{z_{eq}}$  (e.g., Figure 4.6 and 4.7) determines how small the step size in  $v_{z_{eq}}$  needs to be so that the fine structure of electron scattering is brought out. Since we only consider electrons in a relatively narrow energy range (i.e., 100 eV or 100 keV electrons), the lower and upper limits in  $v_{z_{eq}}$  are not crucial and we simply choose them such that there are 50 velocity bins.

The minimum value of the initial equatorial pitch angle is equal to the loss cone angle for  $L = 3$ , i.e.,  $\min(\alpha_{eq_{init}}) = \alpha_{eq_{lc}}(L = 3) = 8.62019^\circ$ . The maximum value of the initial pitch angle and the cell size  $\Delta \alpha_{eq}$  were determined by the maximum pitch angle scattering. Since the maximum pitch angle scattering for the given example is  $\max(\Delta \alpha_{eq_{scatt}}) \sim 0.024^\circ$ , we choose the upper limit of the simulated region such that all the electrons that could possibly have their pitch angles lowered to  $\alpha_{eq} < \alpha_{eq_{lc}}$  in a single encounter with the wave are included, that is,  $\max(\alpha_{eq_{init}}) = \min(\alpha_{eq_{init}}) + 2 \max(\Delta \alpha_{eq_{scatt}}) = 8.66819^\circ$ . The smaller the step size, the better resolution of the fine structure of distribution function dependence on velocity space coordinates. However, the cell size  $\Delta \alpha_{eq}$  can not be smaller than the fluctuation or ‘noise’ level of electron pitch angle change oscillations ( $\Delta \alpha_{eq \text{ noise}} \equiv 10^{-4}^\circ$ , see Figure 5.8). In general, the distribution function after a one-pass interaction does not depend significantly on the pitch angle; instead, the fine structure of this distribution function depends strongly on  $v_{z_{eq}}$  (Figure 5.9). In our example, we choose pitch angle cell size to be  $\Delta \alpha_{eq} = 0.0016^\circ$  so that the population of electrons that is being scattered into the loss cone is represented by 15 cells.

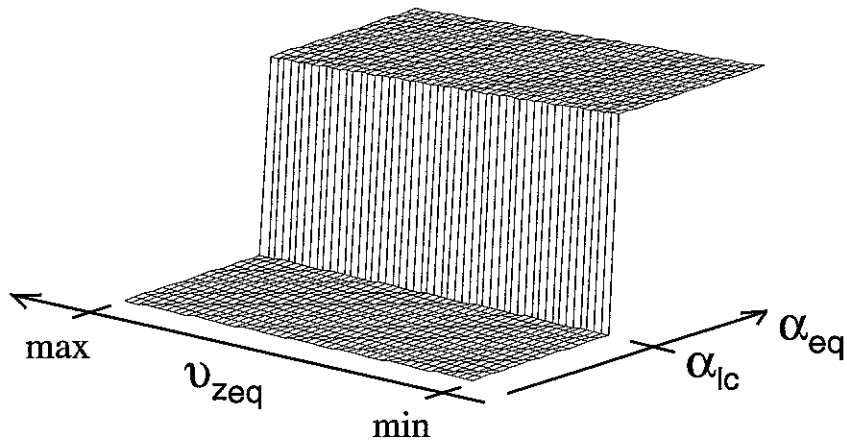
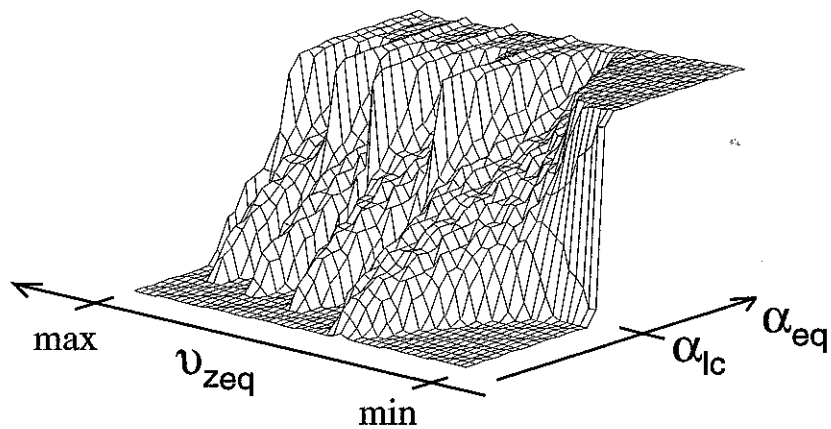




**Figure 5.8. Fluctuation or 'noise' level for pitch angle scattering.** For a sample test electron trajectory, we show resonant pitch angle scattering due to the interaction with the wave ( $\Delta\alpha_{eqf}$ ), and oscillations in pitch angle change far away from the resonant interaction region that we refer to as 'noise' scattering ( $\Delta\alpha_{eq\ noise}$ ). Figure is not in scale.

**Figure 5.9. (Next page) Initial and final distribution.** The initial and final electron distribution functions are shown for a one-pass resonant interaction with the wave of  $E \cong 100$  keV electrons. Note that this figure is a three dimensional version of Figure 5.7. Only half of the areas represented on Figure 5.7 are shown since  $\max(\alpha_{eq})$  was taken to be  $8.64419^\circ$ . The values for  $\min(v_{z_{eq}})$  and  $\max(v_{z_{eq}})$  before and after a one-pass interaction are the same as on Figure 5.7. The lower limits for  $\alpha_{eq}$  are also the same. Local maxima and minima in electron scattering occur due to the constructive and destructive interference between the two resonant encounters of the distribution with the wave.

Initial distribution function

Distribution function after  
a one pass interaction

The picture for  $E = 100$  eV electrons would be similar, with the initial area in the velocity space and cell size given by

$$v_{z_{eq}} \in [5.84, 5.90] \times 10^6 \frac{m}{s}, \quad \Delta v_{z_{eq}} = 0.0012 \times 10^6 \frac{m}{s}$$

$$\alpha_{eq} \in [8.62^\circ, 10.12^\circ], \quad \Delta \alpha_{eq} = 0.05^\circ$$

The resultant scattering of the test electrons from the initial velocity space region as shown on Figure 5.7 is weighed by the initial electron distribution function (see section 5.2.1) to obtain the new electron distribution function after a single encounter between the wave and the distribution (i.e., a one-pass interaction). The initial and final electron distribution functions for a one-pass resonant interaction with the wave of  $E = 100$  keV electrons in the vicinity of the loss cone are shown on Figure 5.9 (for half of the velocity space area shown in Figure 5.7).

The resultant electron distribution function is then used to calculate (as described in section 5.1) the precipitated differential energy spectrum  $\Phi_{E_{prec}}(E)$ . The results for both suprathermal (100 eV) and energetic (100 keV) electrons are shown in Figure 5.10. Since the differential precipitated energy flux is

$$dQ \sim E \Phi_{E_{prec}}(E) dE$$

we can compare the precipitated energy flux at 100 keV and at 100 eV in  $\sim 10\%$  ranges around the maximum of the respective  $\Phi_{E_{prec}}(E)$ . We find the ratio of the differential precipitated energy fluxes for suprathermal electrons precipitated by highly oblique waves and energetic electrons precipitated by ducted ( $\psi=0^\circ$ ) waves to be

$$\frac{dQ_{oblique}(100 \text{ eV})}{dQ_{ducted}(100 \text{ keV})} = 5.9$$

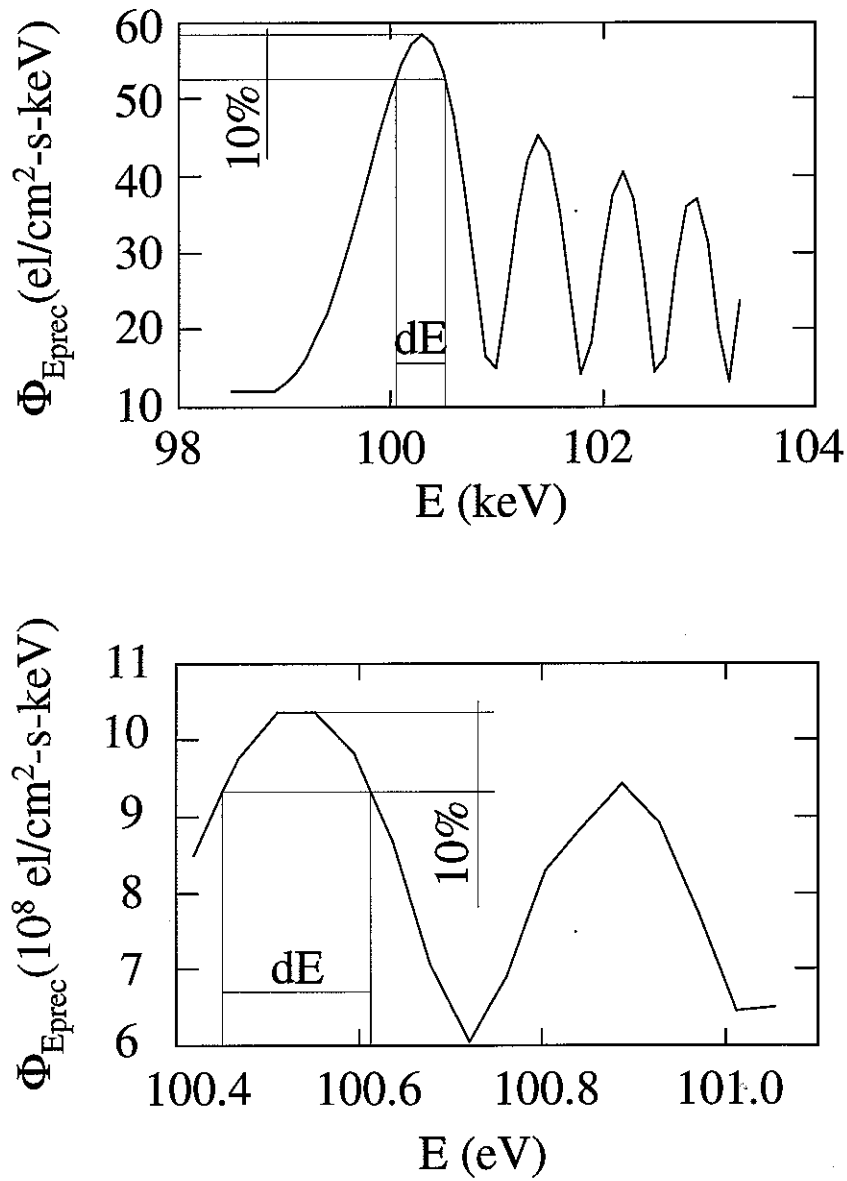


**Figure 5.10. The precipitated differential energy spectrum.** The precipitated differential energy spectrum  $\Phi_{E_{prec}}(E)$  for suprathermal (100 eV) and energetic (100 keV) electrons. The 10% range centered around the first maxima was used to estimate the ratio of the differential energy fluxes of suprathermal electrons precipitated by a highly oblique wave and of energetic electrons precipitated by a ducted wave.

This value is lower than the value of 34 that was evaluated as a first approximation in Chapter 4. Nevertheless, it appears that, on a one-pass interaction basis, the precipitation of suprathermal (100 eV) electrons by non-ducted, oblique whistler mode waves can deposit more energy in the upper ionosphere than the precipitation of energetic (100 keV) electrons by ducted whistler mode waves. Since the latter phenomena is now regularly observed to occur within the plasmasphere both by means of ground-based and *in situ* techniques [Inan *et al.*, 1990; Voss *et al.*, 1984], our results suggest that suprathermal electron precipitation by non-ducted whistlers should also be detectable and that this process possibly constitutes a significant source of loss for the electrons and an important energy input for the upper ionosphere. Estimates of the loss of suprathermal electrons from the radiation belts due to their interaction with oblique whistler mode waves and the perturbations that precipitated energy flux carried by suprathermal electrons might cause in the upper ionosphere are discussed further in Chapter 6.

## 5.4. Magnetospherically Reflected (MR) Whistlers

Non-ducted (oblique) whistler mode waves originating in lightning discharges are often found to undergo multiple reflections between hemispheres. These reflections occur at points where the wave frequency matches the local lower hybrid resonance frequency [Edgar, 1976]. Such multiply reflected whistler waves are called Magnetospherically Reflected (MR) whistlers.

Figure 5.11 shows examples of MR whistlers observed on the DE-1 satellite. The format is one of a typical frequency vs time spectrogram with the density of the shading representing the intensity of the recorded signal. Two whistler events originating in two successive lightning flashes (in this case ~8 s apart)

are shown, each initiating a sequence of MR components. The first few (four) hops of both whistlers show very pronounced dispersion after which the hops begin to merge into each other to form a long enduring relatively narrowband signal. The duration of the narrowband part of the signal for this example is about 2 s. Although the total duration of each MR event is  $\sim 10$  s for the cases shown, MR whistlers are known to last for as long as 100 s [Draganov *et al.*, 1992].

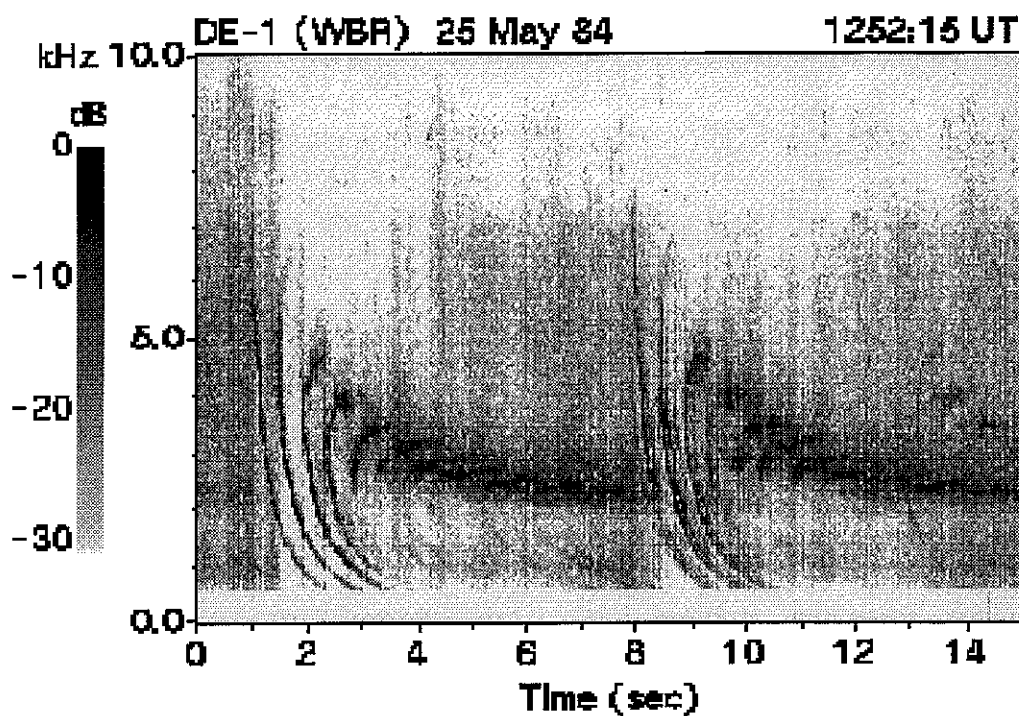


**Figure 5.11. MR whistlers observed on the DE-1 satellite.** The examples are given in the form of a typical frequency vs time spectrogram with the shading representing the intensity of the recorded signal. Two whistler events originating in two successive lightning flashes,  $\sim 8$  s apart, are shown, each initiating a sequence of MR components. After very pronounced dispersion of the first four hops of both whistlers, the hops begin to merge into each other to form a relatively narrow band signal lasting for about 2 s.

Both ducted and MR (oblique) whistlers are generated by lightning discharges. It should be noted that non-ducted whistlers do not require the presence of any specific density structures (e.g., ducts) for their propagation.

They generally occupy larger regions of the magnetosphere [Sonwalkar and Inan, 1993]. On this basis, although the statistics of the occurrence rates of non-ducted whistlers are not well documented, it may safely be assumed that they occur at least as often as ducted whistlers. The ducted whistler rate depends on the time of the year and time of the day and varies from 0.3 whistlers per minute for an average summer day to 22 whistlers per minute for an average winter night [Burgess and Inan, 1992]. For an extremely active day, the ducted whistler rate can be as high as 195 whistlers per minute, but year-round average is 6 whistlers per minute.

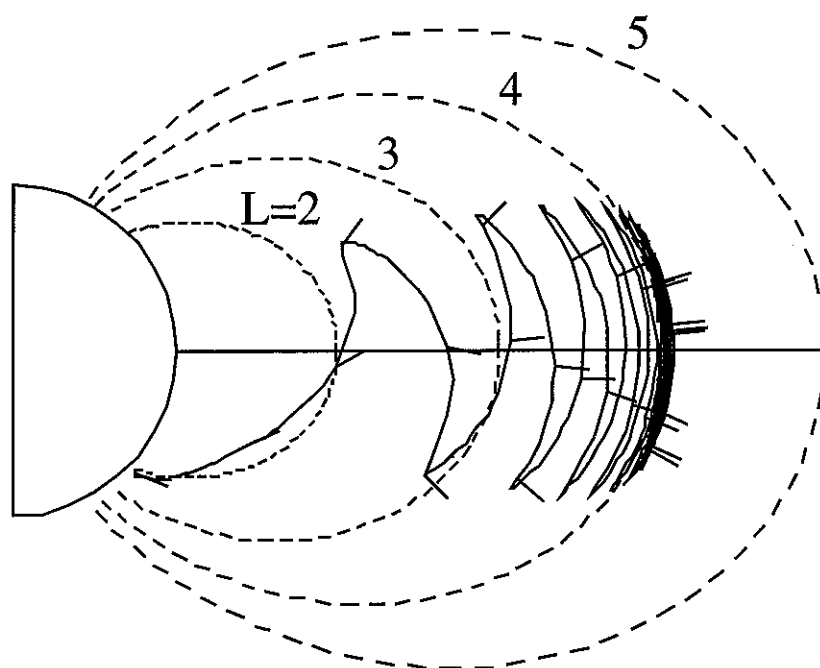


**Figure 5.12. Sample raypath for an MR signal.** The raypath for a  $f=0.33$  kHz wave injected at 400 km altitude, vertically upwards from the southern hemisphere at  $L=2$ , propagating to higher  $L$ -shells by reflecting back and forth between hemispheres and eventually settling down at  $L=4$ .

The magnetospheric reflection of oblique whistler mode waves can be effectively studied by raytracing. Here we utilize the Stanford VLF raytracing code [e.g., see Inan and Bell, 1977]. The example in Figure 5.12 shows a  $f = 0.33$  kHz wave injected vertically upwards from the southern hemisphere at  $L = 2$ . The ray travels vertically upwards reflecting back and forth between the

hemispheres as expected and eventually settles down at  $L \cong 4$ . More extensive raytracing studies [Draganov *et al.*, 1992] show that the  $L$ -shell at which the whistler wave settles down depends strongly on the wave frequency, but is relatively independent of the injection latitude or initial wave propagation direction. The frequency of the whistler wave vs  $L$ -shell of settlement as obtained from raytracing is plotted in Figure 5.13.

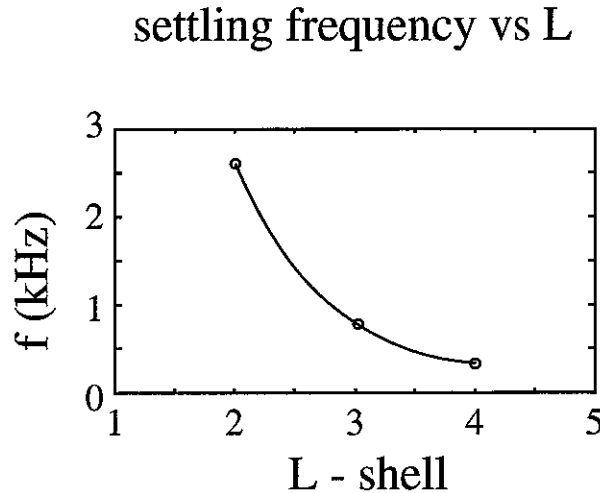


**Figure 5.13. The frequency of the MR whistler wave vs  $L$ -shell of settlement.** This result is derived on the basis of simulated raypaths as shown on Figure 5.12.

To summarize, MR whistlers are oblique whistler mode waves injected into the magnetosphere by lightning, they can endure in the magnetosphere for as long as 100 s each, and after several (5-6) reflections the raypaths settle down into a multiply reflecting pattern at an  $L$ -shell uniquely corresponding ( $f \approx f_{LHR}$ ) to the signal frequency. Thus, at any given  $L$ -shell, we can expect accumulation of oblique whistler mode wave energy at the corresponding frequency. The wave normal angle of the multiply reflecting waves slowly varies with latitude along the field line in a particular manner as dictated by raytracing. As such, these multiply reflecting waves, continuously present along the given  $L$ -shell constitute a narrowband wave which can resonantly interact with the radiation belt electrons. It should be noted that the wave



distribution along the field line consists of a superposition of multiply reflecting waves. In the following, we use a test particle simulation to represent the interactions of a distribution of electrons with these continuously present nearly monochromatic MR whistlers, the wave normal angle of which vary along the field line as described by raytracing. Our assumption of a monochromatic wave with specified phase variation amounts to considering one of the many multiply reflecting wave components, the superposition of which may generate standing wave patterns and slow variations in wave phase.

### 5.5. Electron Precipitation by MR Whistlers

We now investigate the interaction between radiation belt electrons and MR whistlers in the equatorial region at three typical  $L$ -shells. The Poynting flux of the whistler waves was assumed to be  $S = 113 \text{ pW/m}^2$  corresponding to the intensity of a  $f = 6.82 \text{ kHz}$  ducted wave ( $\psi = 0^\circ$ ) with  $B_w = 5 \text{ pT}$  in the equatorial plane at  $L = 4$ . The frequencies of the waves that settle down at the chosen  $L$ -shells and the dependence of their wave normal angle  $\psi$  on the geomagnetic latitude are determined using the Stanford raytracing simulation code, and are given in the Table 5.2. The  $\psi(\lambda)$  represent best-fits to the numerical results obtained from raytracing. The variation of wave normal angle along the field line  $\psi(\lambda)$  is slow enough so that the wave can be considered monochromatic in the WKB sense. The maximum change of wave normal angle  $\psi$  during the course of one electron gyroperiod occurs for the high electron energies for which the resonant interaction occurs in the region of the most rapid change of wave parameters considered (see Table 5.3). Using the expressions for  $\psi(\lambda)$  from Table 5.2, the value of maximum

change of wave normal angle during the course of one electron gyroperiod is calculated to be of the order of  $10^{-3}^\circ$ .

**Table 5.2. Parameters of non-ducted waves.** The dependence of the wave normal angle on geomagnetic latitude and the frequency of oblique whistler mode waves which settle down on the corresponding L-shell. Also given are the equatorial cold electron densities assumed for each of the corresponding L-shells.

L	$N_e$ in $\frac{el}{cm^3}$	$f$ (kHz)	$\psi(\lambda)$ , both in degrees
2	1500	2.6	$\psi = 90 - 0.0684\sqrt{8^2 - (\lambda - 0.15)^2}$
3	600	0.78	$\psi = 90 - 0.07\sqrt{6^2 - (\lambda - 0.1)^2}$
4	400	0.33	$\psi = 90 - 0.0727\sqrt{5.5^2 - (\lambda - 0.1)^2}$

**Table 5.3. Simulation parameters.** Limits for the simulated region in velocity space, cell sizes and constraints on the position of the resonant interaction along the L-shell for the resonant interaction with the MR whistler mode waves settling down at  $L = 2, 3, 4$ .

$L$	$v_{z_{eq}} \left(10^6 \frac{m}{s}\right)$	$\Delta v_{z_{eq}}$	$\alpha_{eq}$ (deg)	$\Delta \alpha_{eq}$	$\lambda$ (deg)
2	270.0–283.1	0.05	16.76813–16.76827	$1 \times 10^{-5}$	-7 – +7
3	220.8–261.1	0.1	8.62019–8.62043	$2 \times 10^{-5}$	-5 – +4
4	186.6–215.0	0.1	5.4735–5.4747	$6 \times 10^{-5}$	-4.5 – +5

We now study the resonant interaction between these monochromatic MR signals and radiation belt electrons represented by the distribution function as defined in section 5.2.1, using the test particle simulation model described in previous chapters.

Table 5.3 defines the boundaries of the regions in the velocity space, the cell sizes and the region along the field line included in our model for all three  $L$ -shells considered.

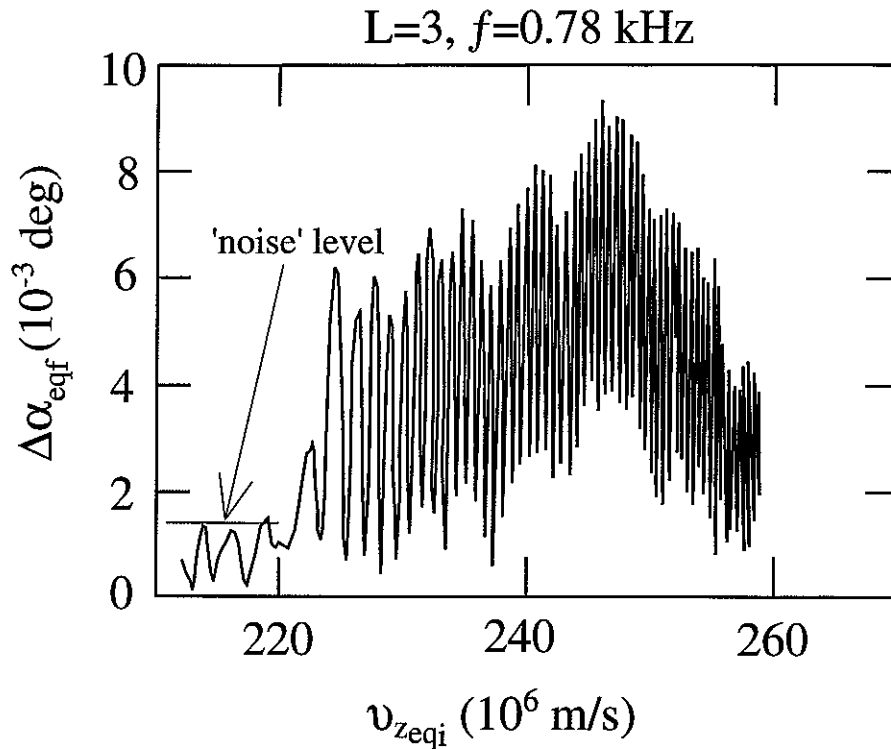


**Figure 5.14. Dependence of particle scattering on initial  $v_{zeq}$ .** The root-mean-square value of the particle pitch angle change  $\Delta\alpha_{eqf}$  is plotted for different initial electron velocities  $v_{zeq}$ . Pitch angle scattering depends strongly on  $v_{zeq}$  with local maxima and minima corresponding respectively to the constructive and destructive interference between the two resonant encounters of the particles with the wave. With the decrease in  $v_{zeq}$ , scattering eventually reaches the 'noise' level (Figure 5.8).

Single test particle trajectories were examined to determine the region in velocity space that includes all electrons that can resonantly interact with the chosen wave and that could be scattered into the loss cone. The size of the  $v_{z_{eq}} - \alpha_{eq}$  cell and the minimum and maximum value of the initial  $\alpha_{eq}$  were determined in the manner identical to that described in section 5.3. Since we are now interested in all possible resonant interactions with near-loss-cone electrons regardless of their energy, the lower and upper limits for the initial  $v_{z_{eq}}$  are determined by the resonant interaction region in the velocity space itself and restrictions on the model validity rather than by the narrow electron energy range considered, as was the case in section 5.3.

The value of the lower limit of  $v_{z_{eq}}$  is smaller than the equatorial resonant velocity  $v_R(\lambda = 0^\circ)$  (a parameter that depends on the medium and wave characteristics as discussed in more detail in section 3.4) and was chosen such that all electrons whose pitch angle scattering due to the resonant interaction with the wave is larger than the 'noise' scattering due to the non-resonant

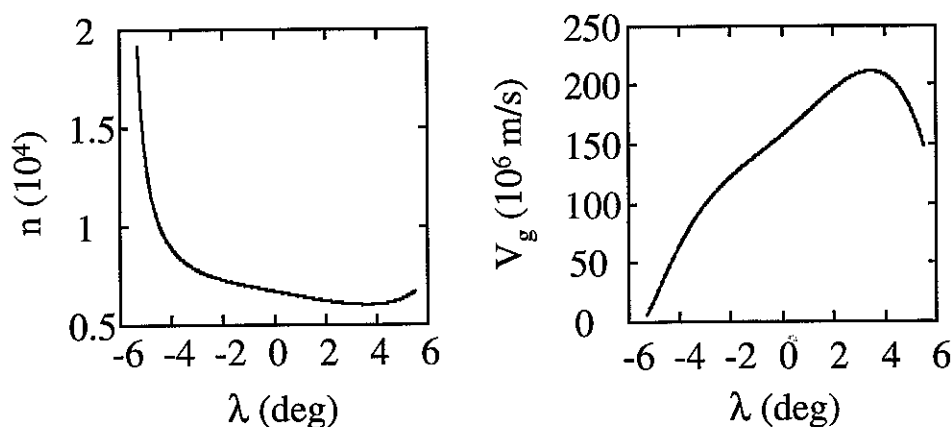
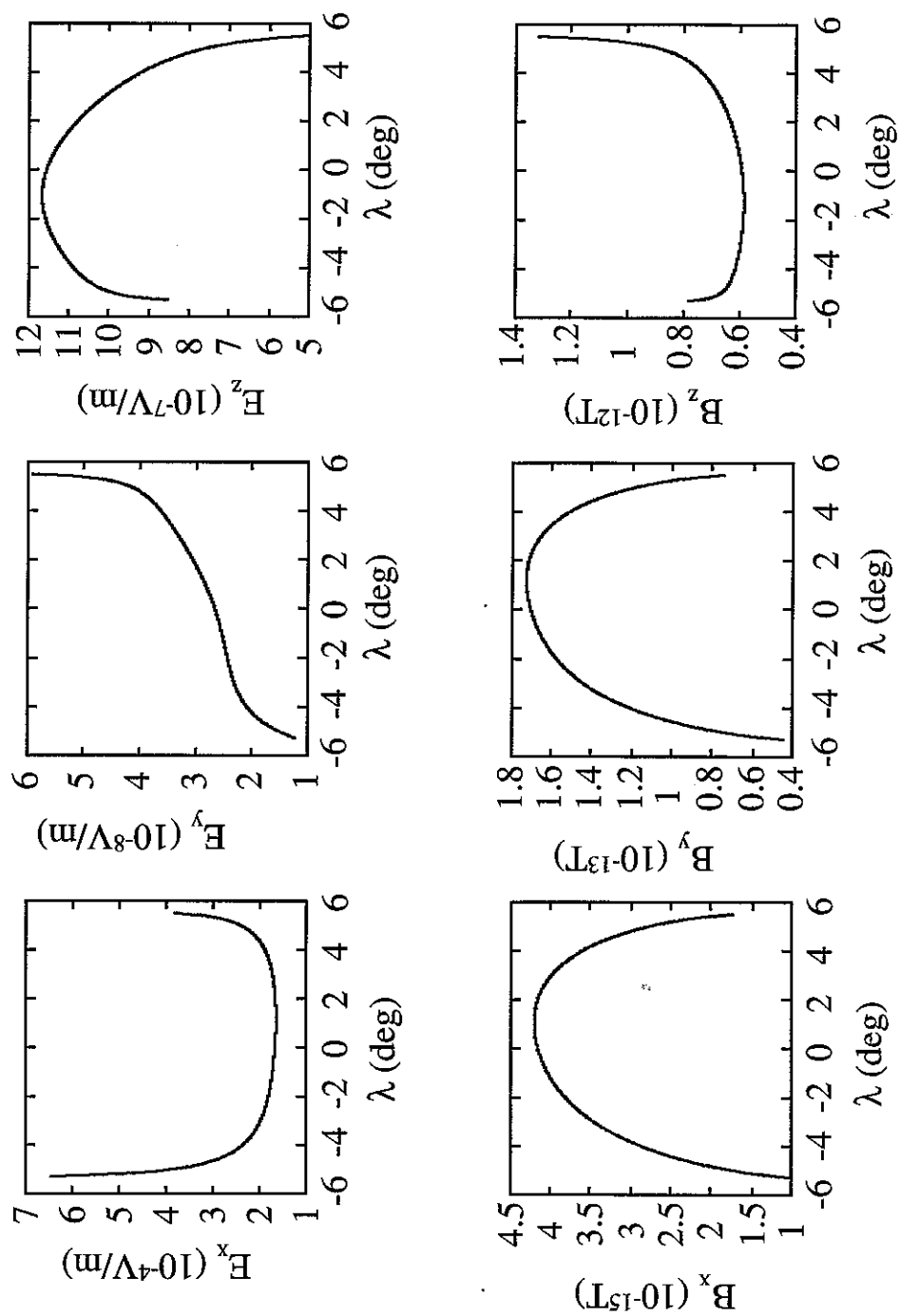


**Figure 5.15. Dependence of the wave parameters on geomagnetic latitude along the field line.** (also see next page) For a 0.33 kHz whistler mode wave that settles down at  $L \approx 4$ , best fit to the numerical data from the raytracing was used to determine the wave normal angle dependence on geomagnetic latitude  $\psi(\lambda)$  along the  $L=4$  field line. For such a wave, the dependence of wave electric ( $E_x, E_y, E_z$ ) and magnetic ( $B_x, B_y, B_z$ ) fields, refractive index  $n$ , and group velocity  $V_g$  on latitude  $\lambda$ , at  $L=4$  are given.

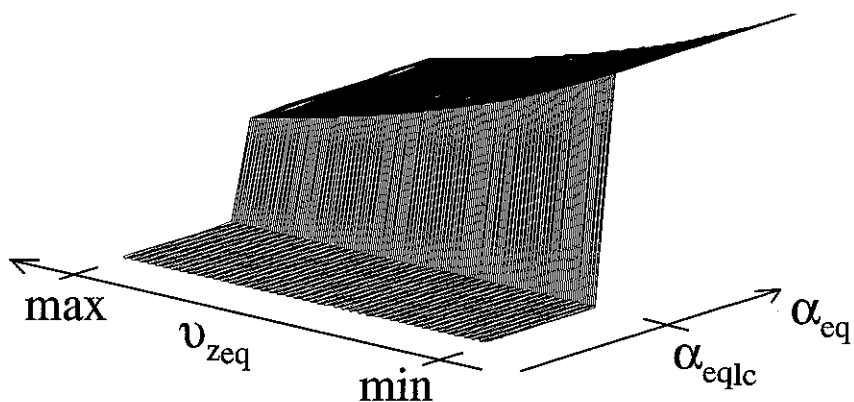


interaction with the wave (e.g.,  $v_{zeq} \ll v_R(\lambda = 0^\circ)$ ), are included (Figure 5.8). After it reaches the maximum value (for  $v_{zeq}$  slightly higher than  $v_R(\lambda = 0^\circ)$ ), the rms value of the pitch angle change  $\overline{\Delta\alpha_{eqf}}$  decreases rapidly to the 'noise' level with the decrease in  $v_{zeq}$  (Example on Figure 5.14 is given for the interaction with MR whistler at  $L = 3$ ). These curves, obtained by examination of single test particle trajectories, were used to determine  $\min(v_{zeq})$ . The upper limit for  $v_{zeq}$  is determined by the constraint on validity of our simulation model, that is that resonant interaction has to take place at a magnetic latitude where wave parameters do not change significantly over one gyroperiod in the reference frame of the electron. Figure 5.15 shows the dependence of electric and magnetic fields as well as the refractive index and wave group velocity on latitude for a wave that settles down at  $L = 4$ . Wave parameters change relatively more rapidly with geomagnetic latitude for  $\lambda < -4.5^\circ$  and  $\lambda > 5^\circ$ , so at  $L = 4$  we choose to consider resonant interactions of the given wave with near-loss-cone radiation belt electrons with energy such that  $v_{zeq} < \max(v_{zeq}) = \min[v_R(\lambda = -4.5^\circ), v_R(\lambda = 5^\circ)]$ .

Figure 5.16 shows the near loss cone electron distribution function resulting from a one-pass interaction with a 0.33 kHz oblique whistler wave at  $L = 4$ . Local maxima and minima in electron scattering occur due to the constructive and destructive interference between the two resonant encounters (on both sides of the equator) of the particles with the wave that occur for  $v_{zeq} > v_R(\lambda = 0^\circ)$  (see sample trajectories in Chapter 4). Maximum penetration into the loss cone ( $\sim 5 \times 10^{-4}^\circ$ ) occurs for  $v_{zeq} = 198.4 \times 10^6$  m/s, which is slightly higher (2.96%) than  $v_R(\lambda = 0^\circ) = 192.7 \times 10^6$  m/s.

The distribution functions similar to that shown in Figure 5.16 and which result from a one-pass interactions with the wave are also computed for  $L = 2$  and 3 and are subsequently used to calculate the precipitated differential electron spectra as shown in Figure 5.17 for all three  $L$ -shells. In general, MR whistler components which settle down on higher  $L$ -shells resonantly interact with and scatter lower energy electrons. For example, a 0.33 kHz whistler

Initial distribution function  
 $f \sim v^{-6}$  ( $10^8$  el/cm<sup>2</sup>-s-sr-keV at 1keV)



Distribution function  
 after one-pass interaction

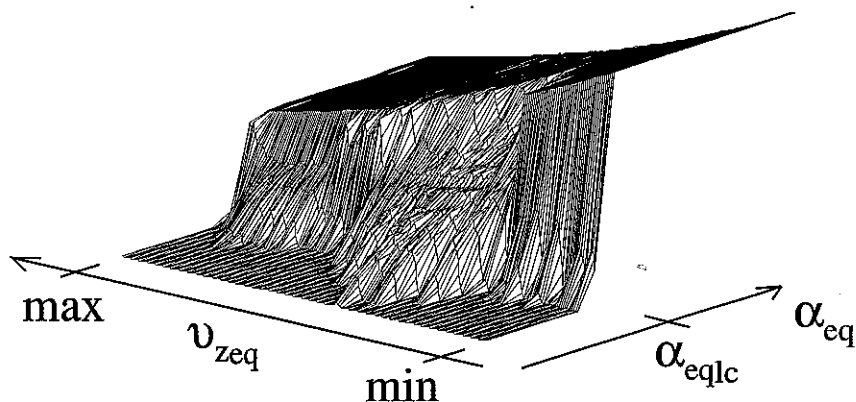


**Figure 5.16.** The initial and final near-loss-cone electron distributions for a one-pass interaction with a 0.33 kHz whistler wave at  $L=4$ . Local maxima and minima in electron scattering occur due to the constructive and destructive interference between the two resonant encounters of the distribution with the wave.

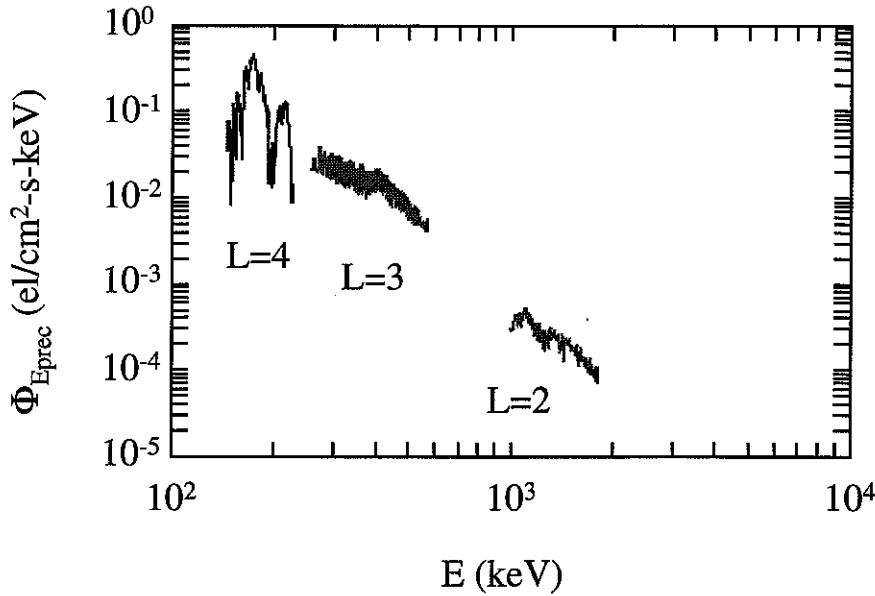


**Figure 5.17. Precipitated differential electron spectra.** For all three cases considered, precipitated differential electron spectra is calculated from the distribution function (such as that in Figure 5.16) after a one-pass interaction with the corresponding wave.

wave at  $L=4$  scatters electrons in the 150–220 keV range, whereas the 2.6 kHz MR whistler component that settles down at  $L=2$  scatters electrons in the 1–2 MeV energy range. Precipitated differential electron flux is in general higher for lower energy electrons that are scattered on higher  $L$ -shells. Maximum value of the precipitated differential electron flux at  $L = 4$  is  $\Phi_{E_{prec}}(173 \text{ keV}) = 4.6 \times 10^{-1} \text{ el/cm}^2\text{-s-keV}$  and is three orders of magnitude higher than that due to the resonant interaction with MR whistler at  $L = 2$ ,  $\Phi_{E_{prec}}(1.11 \text{ MeV}) = 5.2 \times 10^{-4} \text{ el/cm}^2\text{-s-keV}$ . Corresponding total precipitated energy fluxes are



$$Q(L=2) = 0.48 \times 10^{-9} \frac{J}{m^2 s} = 0.48 \times 10^{-6} \frac{erg}{cm^2 s}$$

$$Q(L=3) = 2.66 \times 10^{-9} \frac{J}{m^2 s}$$

$$Q(L=4) = 3.14 \times 10^{-9} \frac{J}{m^2 s}$$

and are generally higher for higher  $L$ -shells.

The electron lifetimes corresponding to the precipitated fluxes of Figure 5.17 and calculated using the definitions and assumptions described in the sections 5.1.2 and 5.1.3, are given as a function of electron energy in Figure 5.18. The minimum lifetimes of the electrons with the corresponding energy that are scattered by MR whistlers are of the order of several days and do not differ significantly for interactions on different  $L$ -shells. The minimum electron lifetimes vary from 2.47 days for  $E = 1.11$  MeV electrons at  $L = 2$  to 4.64 days for  $E = 173$  keV electrons at  $L = 4$ .

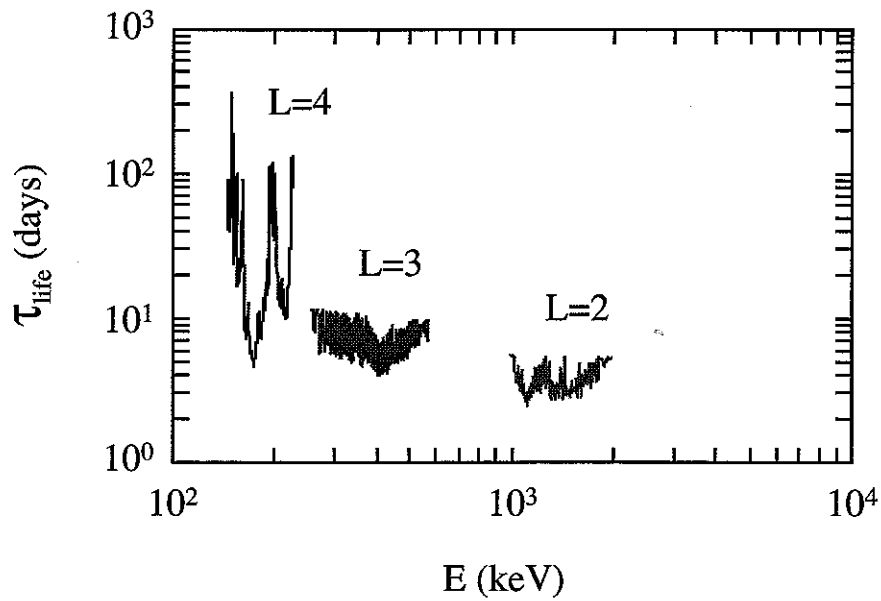


**Figure 5.18. Electron lifetimes.** Precipitated differential electron spectra are used to calculate electron lifetimes as discussed in the text.

In Figure 5.19 we compare our lifetime estimates with those due to cyclotron resonant scattering by whistler mode hiss following large magnetic storms [Lyons *et al.*, 1972]. Interaction between radiation belt electrons and hiss causes precipitation and loss from  $L = 3$  and 4 of electrons in a broader energy range than that due to the resonant electron-MR whistler interaction. At  $L = 3$  and 4 electron lifetimes due to hiss induced losses are smaller than the electron lifetimes due to resonant electron-MR whistler interaction.

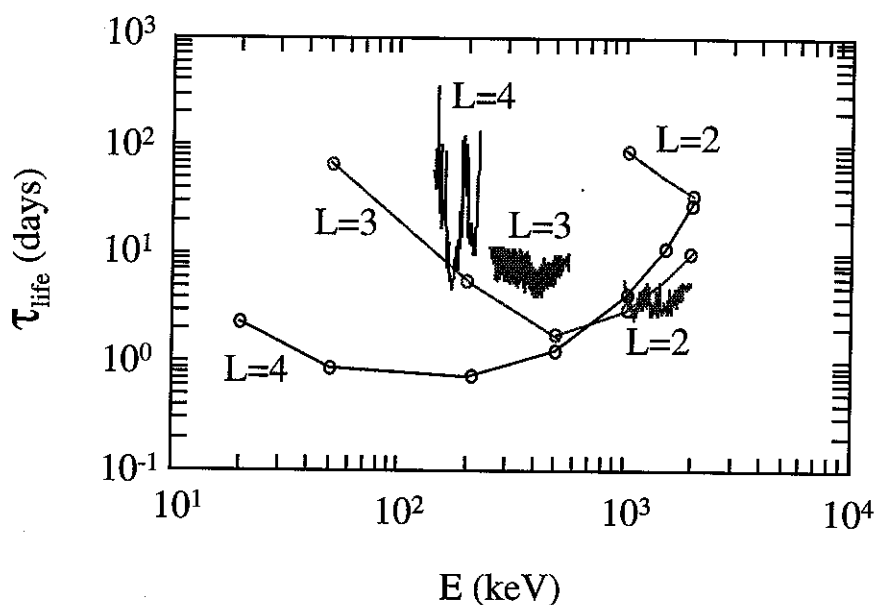


**Figure 5.19. Electron lifetimes compared with previous work.** We compare our lifetime estimates (—) with those due to cyclotron scattering by whistler mode hiss following large magnetic storms [Lyons *et al.*, 1972] (—o—).

However, at  $L = 2$  MR whistlers can contribute more than hiss to the electron loss from the radiation belts. Note that the results given by Lyons *et al.* [1972] are calculated based on the assumption of the continuous presence of a wide band oblique whistler mode signal throughout the entire plasmasphere. In order to be able to compare the two, we also assumed the continuous presence of coherent, narrowband oblique whistler mode signal throughout the entire plasmasphere. However, our results can be scaled to more realistic values by

simple multiplication once the ratios for spatial and temporal presence of the MR whistlers throughout the plasmasphere are available.

## 5.6. Interaction With Incoherent Signals

In this subsection, we briefly discuss dependence on the coherence of the wave of the single particle trajectories and the net pitch angle changes which occur in a single encounter with the wave. This issue is important in view of our assumption of a coherent wave in all of the test particle calculations presented in this report. In principle, whistlers injected into the magnetosphere can be represented as narrowband signals with slowly varying frequency so that the assumption of a coherent wave is valid along each ray path. However, from the point of view of a particle confined to a given field line, the wave phase could in general deviate from that of a coherent wave as described by  $e^{i(\omega t - \vec{k} \cdot \vec{z})}$ , since different points along the field line are illuminated by different rays along which there is a different accumulated phase. It is important to note, however, that for given magnetospheric density gradients (which determine the distribution of ray paths) the deviation in phase would be a deterministic and slowly varying function so that the test particle trajectories would not significantly differ from those for a coherent wave. In other words, just as we have specified a particular variation of the wave normal angle  $\psi$  along the field line (either taken constant as in Chapter 4 and section 5.3 or variable as dictated by raytracing as in section 5.5) we could have added a slowly varying phase term in the equation for the phase  $\eta$  (Eq. 3.7), with little effect on our results. Note that in the case of multiply reflected MR whistlers (section 5.5), our calculations with the assumption of a coherent

wave with specified  $\psi(\lambda)$  are valid for each component of reflected wave which might coexist with others.

With this perspective, we now examine the nature of the particle trajectories as a function of the coherence of the signal. For a detailed comparison of gyroresonant scattering by coherent and incoherent whistler mode waves in the magnetosphere the reader is referred to *Inan* [1987], who showed that, for test particle calculations, the incoherence of the waves can be simulated by means of random frequency modulation and applied this method to the interactions involving ducted whistler mode waves. Results of *Inan* [1987] indicated that although the net scattering of individual test particles were reduced for incoherent waves, the velocity space bandwidth of the interaction increased (i.e., more particles are scattered) and the precipitation flux levels remained about the same for coherent or incoherent waves. Here, we use the same approach to describe the effects of the incoherence of the wave on the scattering of the particles by non-ducted whistler mode waves. For each step along the electron trajectory ( $\Delta\lambda \cong 4.4 \times 10^{-4}^\circ$  corresponding to approximately  $\Delta t \sim 1\mu s$ ) the wave frequency is taken to be given by

$$f_{noise} = f(1 - p R_n)$$

where  $f$  is the fixed, coherent wave frequency,  $p$  is the maximum noise level expressed as a fraction of the wave frequency and  $R_n$  is a random number. As shown by *Inan* [1987], power spectral density of such a signal with randomly modulated frequency is relatively uniform around the center frequency so that this method provides a good representation of an incoherent signal.

In the region where the MR whistler raypath converges to a certain  $L$ -shell corresponding to its frequency (Figure 5.13), the frequency of the MR whistler is very close to the cutoff frequency above which there is no propagation (see Figure 3.3). Therefore we take the random number to be in the range

$$R_n \in [0, 1]$$

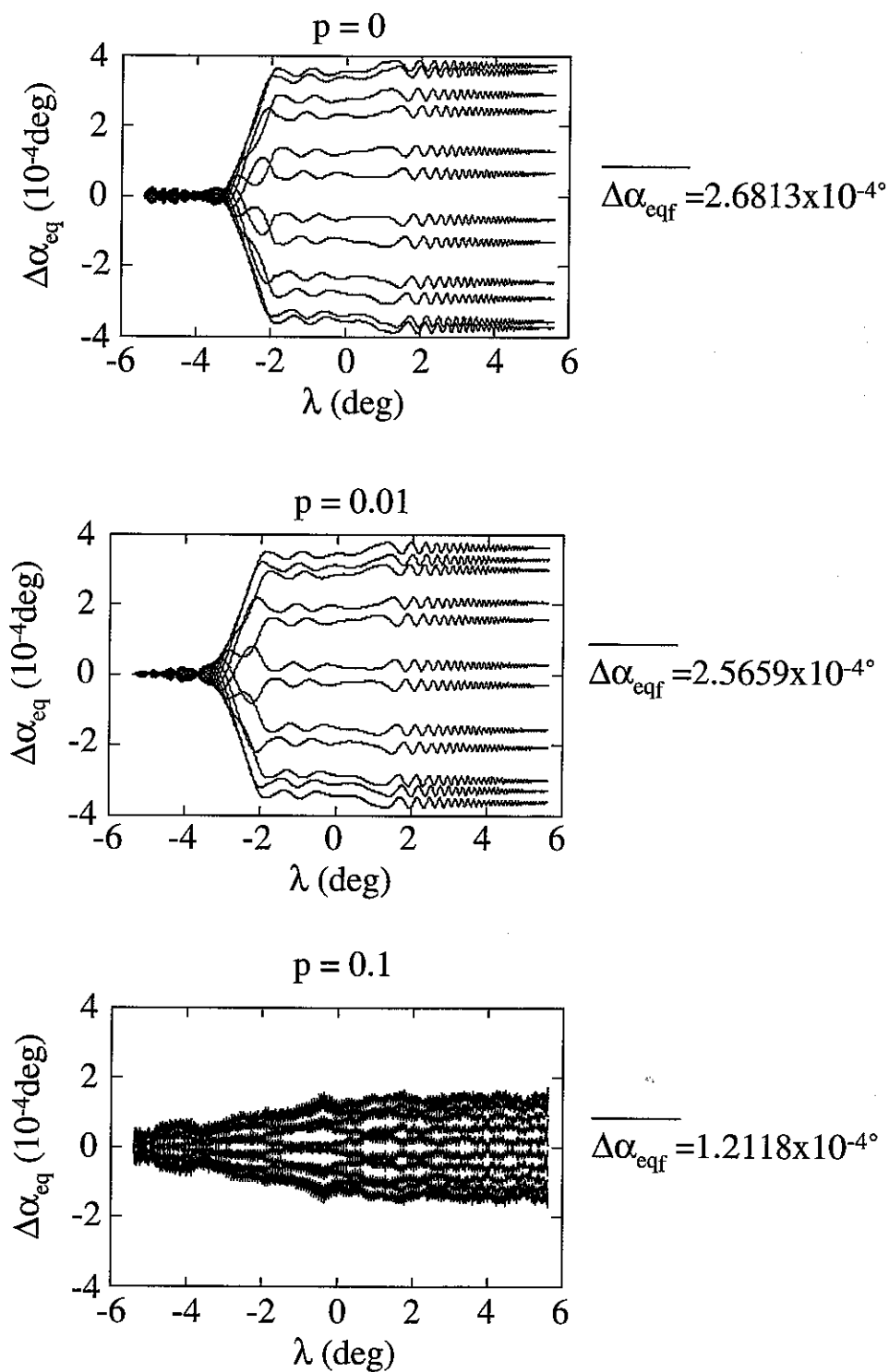


**Figure 5.20. Test trajectories for electrons interacting with incoherent signals.** Test electron trajectories for interaction with a) coherent signal, b) incoherent signal with 1% random frequency noise and c) incoherent signal with 10% random frequency noise.

Figure 5.20 shows trajectories of test electrons interacting with waves of different levels of coherence, as indicated by  $p = 0$ ,  $p = 0.01$  and  $p = 0.1$ . The wave was taken to be at 0.33 kHz, with a wave-normal angle variations along the field line as given in Table 5.2, representing an MR whistler component at  $L = 4$ . The resonant interaction with all three signals cause scattering in electron pitch angle. The rms of pitch angle change due to scattering by the incoherent whistler with  $p = 0.01$  is equal to  $\overline{\Delta\alpha_{eqf}} = 2.5659 \times 10^{-4^\circ}$  and is somewhat smaller than the  $\overline{\Delta\alpha_{eqf}} = 2.6813 \times 10^{-4^\circ}$  for the interaction with coherent,  $p = 0$  whistler. Scattering due to the interaction with the incoherent wave with  $p = 0.1$  produces  $\overline{\Delta\alpha_{eqf}} = 1.2118 \times 10^{-4^\circ}$ , approximately two times smaller than the scattering for coherent waves. The general trend of the results is, as expected, a reduction in net scattering for individual test particles with decreasing wave coherence, as was also found by *Inan* [1987] for parallel propagating waves.

# **6.**

## **Summary and Conclusions**

We have carried out test particle simulations of the cyclotron resonant scattering of energetic and suprathermal electrons in a single resonant encounter (one pass) with obliquely propagating monochromatic whistler-mode waves in the magnetosphere. Our results indicate that, for typical parameters as used in this thesis, these interactions result in significant perturbations of the trapped particle distributions and lead to precipitation of particle fluxes into the ionosphere. The primary geophysical significance of our results lie in their implications in terms of (i) radiation belt equilibrium and (ii) effects of the precipitation on the ionosphere.

### **6.1. Radiation Belt Equilibrium**

Although our individual simulations were limited to one-pass interactions with monochromatic oblique waves, when viewed as a whole, they imply that wave energy injected into the magnetosphere by lightning and propagating obliquely in the non-ducted mode may substantially contribute to the establishment of radiation belt equilibrium.

In this context, we have shown that (i) obliquely propagating waves can efficiently resonate with particles of the same energy as they multiply bounce back and forth between hemispheres (Chapter 2), (ii) precipitation fluxes of suprathermal electrons scattered by oblique waves is comparable to or larger than that of energetic electrons scattered by ducted waves (Chapter 4), and (iii) oblique MR waves which settle down on given  $L$ -shells and exist for up to 100 s can significantly affect the lifetimes of the energetic electrons. In the case of the latter, it should be noted that non-ducted whistlers injected into the magnetosphere typically have components over a wide range of frequencies, so that each frequency component would 'settle' on a different  $L$ -shell and the scattering as computed in Chapter 5 can be expected to occur simultaneously over a broad range of  $L$ -shells during the 10–100 s following each lightning discharge.

The implications of our results should be evaluated in the context of recent theoretical and experimental findings which clearly indicate that ducted whistler waves originating in lightning regularly precipitate energetic radiation belt electrons. The ionospheric signatures of the scattering of energetic electrons out of the radiation belts in cyclotron resonant interactions with lightning-generated ducted (i.e., parallel propagating) whistlers has been both theoretically studied in detail [*Inan*, 1977; *Inan et al.*, 1978; *Inan et al.*, 1982; *Chang*, 1983; *Chang and Inan*, 1983b; *Chang and Inan* 1985] and commonly observed [*Inan et al.*, 1990; *Burgess and Inan*, 1990, and references therein]. As a measure of the effectiveness of this interaction, precipitated energetic electron fluxes have been theoretically estimated and compared with experimental data [*Inan et al.*, 1985b; *Inan and Carpenter*, 1987]. Although ducted whistlers often reflect from the lower ionospheric boundary and can bounce back and forth along the duct multiple times, most experimental evidence of ducted whistler induced precipitation involves single encounter interactions with a discrete one-hop whistler. In terms of the contribution of ducted-whistler-induced precipitation to radiation belt losses, the rate of occurrence of lightning and whistlers is thus a determining factor. For an extreme day ducted whistler rate can be as high as 195 whistlers per



minute, but year-round average is 6 whistlers per minute [*Burgess and Inan, 1992*].

However, the bulk of the magnetospheric wave energy from lightning discharges propagates in the non-ducted mode. Non-ducted whistlers do not require the presence of any specific density structures (e.g., ducts) for their propagation and they generally occupy larger regions of the magnetosphere [*Sonwalkar and Inan, 1993*]. On this basis, although the statistics of the occurrence rates of non-ducted whistlers are not well documented, it may safely be assumed that they occur at least as often as ducted whistlers. The rate of event occurrence is important for discrete one-pass interactions such as those involving the first few hops of non-ducted whistlers or with oblique whistlers that are not magnetospherically reflected.

For discrete one-pass interactions, the significance of the processes studied lies in the quantitative precipitation flux levels. As an example of an early stage (first or second hop) of an MR whistler or just an oblique whistler that will not get reflected by the magnetosphere (Figure 4.3), we can consider the  $f=15.79$  kHz,  $\psi=60^\circ$  oblique whistler, introduced in sections 4.3 and 5.3. Resonant interactions of this whistler with the  $E=100$  eV electrons in the equatorial region of  $L=3$  and in the  $\Delta E=0.2$  eV energy range causes precipitation flux of  $2 \times 10^4$  el/cm<sup>2</sup>-s. This value can be compared with that which results from the interaction of  $E=100$  keV electrons in the equatorial region at  $L=3$  with ducted,  $f=1.44$  kHz,  $\psi=0^\circ$  whistlers for which the precipitation flux is 30 el/cm<sup>2</sup>-s in the  $\Delta E=0.5$  keV range. Since fluxes of the later type have been measured on satellites and rockets [*Voss et al. 1984; Goldberg et al., 1986*] and are believed to be significant in terms of radiation belt losses [*Burgess and Inan, 1992*], it appears that the 100 eV electron fluxes due to oblique whistlers would be easily detectable and at least as significant.

Interaction of radiation belt electrons with MR whistlers at a later stage of their propagation (after the settlement of ray paths on a certain  $L$ -shell, when the wave normal angle is high, close to  $90^\circ$ ) endures for as long as the waves exist ( $\sim 100$  s) so that it is appropriate to discuss the consequences of the

losses in terms of radiation belt electron lifetimes. As shown in section 5.5, interactions with MR whistlers causes precipitation of higher energy electrons from lower  $L$ -shells. Electrons in the energy range of 1–2.6 MeV are precipitated from  $L=2$ , whereas from  $L=4$  precipitated electron energy range is 150–220 keV. The precipitated differential electron flux, due to this interaction, is higher for higher  $L$ -shells, and the maximum value is ranging from  $\Phi_{E_{prec}}(1.11 \text{ MeV})=5.2 \times 10^{-4} \text{ el/cm}^2\text{-s-keV}$  at  $L=2$  to  $\Phi_{E_{prec}}(173 \text{ keV})=4.6 \times 10^{-1} \text{ el/cm}^2\text{-s-keV}$  at  $L=4$ . The lifetimes of the radiation belt electrons in a tube around the  $L$ -shell on which the interaction takes place range depending on electron energy from several days to ~100 days and are comparable with lifetimes corresponding to electron loss induced by hiss [Lyons *et al.*, 1972]. The minimum electron lifetimes vary from 2.47 days for  $E=1.11 \text{ MeV}$  electrons at  $L=2$  to 4.64 days for  $E=173 \text{ keV}$  electrons at  $L=4$ .

## 6.2. Effects on the Upper Ionosphere

The electrons lost from the radiation belts due to their resonant interaction with whistler mode waves are precipitated into the ionosphere where they may cause significant disturbances.

Scattering of energetic electrons out of the radiation belts through cyclotron resonant interactions with lightning-generated ducted whistlers has been observed and related to the ionospheric disturbances [Voss *et al.*, 1984, Inan *et al.*, 1985, Inan *et al.*, 1990; Burgess and Inan, 1990, Burgess and Inan, 1992]. As a measure of cyclotron resonant interaction between the radiation belt electrons and ducted whistler mode waves, precipitated energetic electron fluxes have been calculated in theoretical studies and experimentally observed. These results can be combined with the results shown in the previous chapters

to predict, to the first order, the effects on the ionosphere of the electron precipitation by oblique whistlers.

### 6.2.1. Ionospheric Disturbances Caused by Suprathermal Electrons

In section 5.3 the ratio of the differential precipitated energy fluxes for suprathermal and energetic electrons precipitated by oblique and ducted whistler mode waves respectively, is calculated to be

$$\frac{dQ_{oblique}(100\text{eV})}{dQ_{ducted}(100\text{keV})} = 5.9$$

Lightning induced electron precipitation bursts have been measured to have peak flux levels of  $10^{-3}$ – $10^{-2}$  ergs/cm<sup>2</sup>-s [Voss *et al.*, 1984], consistent with the ionospheric disturbances produced by such bursts [Inan *et al.*, 1985a]. Since our simulation model is restricted to the particle precipitation by a coherent signal whereas in reality there are a broad range of frequencies in a single whistler wave and many whistlers originating from a single lightning discharge we expect the total precipitated energy fluxes to be higher than the calculated ones. Therefore, to estimate the total precipitated energy flux of  $E=100$  eV electrons due to their resonant interaction with an incoherent, lightning induced, oblique whistler mode wave we use the peak value of the measured energy flux of 100 keV electrons, caused by the lightning induced ducted whistler and the ratio of the differential precipitated energy fluxes for 100 eV and 100 keV electrons to get

$$Q_{oblique}(100\text{eV}) = 5.9 \times 10^{-2} \frac{\text{erg}}{\text{cm}^2\text{s}}$$

The  $E=100$  eV electron particle flux precipitated by oblique whistler mode wave is then

$$F_{oblique}(100\text{eV}) = \frac{Q_{oblique}(100\text{eV})}{100\text{eV}} = 36.83 \times 10^7 \frac{\text{el}}{\text{cm}^2\text{s}}$$

This precipitated electron flux can lead to measurable light emissions (e.g. 6400Å), X-rays and density enhancement through secondary ionization. For example, using published ion-pair production rates per unit incident electron flux [Rees, 1989, Doolittle, 1982, Banks *et al.*, 1974] we find that the above flux of 100 eV electrons should produce maximum ionization rates of

$$q = F_{oblique}(100\text{eV}) \times 10^7 = 36.83 \frac{\text{ion pairs}}{\text{cm}^3\text{s}}$$

at altitudes of 300–400 km. Such an incremental change in electron density ( $\Delta N_e \cong 36 \text{ cm}^{-3}$  for a 1 s long precipitation burst) is small compared to typical nighttime ambient densities of  $\sim 10^4 \text{ cm}^{-3}$  at these altitudes [Ratcliffe, 1960]. However, it should be noted that relaxation time for excess ionization at these altitudes can be as long as many minutes, [Vickrey and Kelley, 1983] which is much greater than the interval between flashes in typical thunderstorms [Uman, 1984], so that the ionization can be expected to build up as a result of successive flashes. In the course of an hour long thunderstorm, for example, the excess ionization might build up to  $\sim 10^4 - 10^5 \text{ cm}^{-3}$ , constituting a significant disturbance on top of the ambient.

### 6.2.2. On Secondary Ionization in the Lower Ionosphere Caused by MR Whistlers

The ionization rate due to the electron precipitation caused by MR whistlers can be calculated using the same sources for the dependence on altitude and incident particle energy of ion-pair production rate per unit incident flux [Rees, 1989, Doolittle, 1982, Banks *et al.*, 1974].

As a first step we use the results from section 5.3 (see Figure 5.9 for 100 keV electrons precipitated at  $L = 3$  by ducted whistlers with intensity  $S_d = 8.1 \text{ pW/m}^2$ ) and section 5.5 (see Figure 5.17 for 400 keV electrons precipitated at  $L = 3$  by an MR whistler with intensity  $S_{MR} = 113 \text{ pW/m}^2$ ) to determine the

ratio of the 400 keV electron flux precipitated by MR whistlers and 100 keV electron flux precipitated by ducted whistler

$$\frac{F_{MR}(400 \text{ keV})}{F_d(100 \text{ keV})} = \sqrt{\frac{S_d}{S_{MR}}} \frac{\Phi_{E_{prec}}(400 \text{ keV})dE}{\Phi_{E_{prec}}(100 \text{ keV})dE} = 0.89 \times 10^{-4}$$

The square root of the ratio between the Poynting fluxes of the waves reflects the fact that the precipitated differential fluxes  $\Phi_{E_{prec}}$  are proportional to the wave intensity.

For the case of observed fluxes of  $10^{-2}$  ergs/cm<sup>2</sup>-s [Voss *et al.*, 1984] of ~100 keV electrons precipitated by a ducted whistler we find the corresponding particle flux

$$F_d(100 \text{ keV}) = 6.24 \times 10^4 \frac{el}{\text{cm}^2 \text{s}}$$

Using the ion-pair production rates from [Rees, 1989, Doolittle, 1982, Banks *et al.*, 1974] we get the maximum ionization rate caused by 100 keV electrons precipitated by a ducted whistler to be

$$q_d = F_d(100 \text{ keV}) \times 10^{-3} = 62.4 \frac{\text{ion pairs}}{\text{cm}^3 \text{s}}$$

at ~80 km. The maximum ionization rate caused by 400 keV electrons precipitated by an MR whistler, calculated in the same manner is

$$q_{MR} = F_{MR}(400 \text{ keV}) \times 10^{-2} = 5.57 \times 10^{-2} \frac{\text{ion pairs}}{\text{cm}^3 \text{s}}$$

at ~75 km.

The secondary ionization rate caused by 400 keV electrons precipitated by an MR whistler is thus expected to be 3 orders of magnitude smaller than the secondary ionization rate caused by 100 keV electrons precipitated by a ducted whistler. However, because of the difference in the time duration of these two signals the total ionization created in the two cases may well be comparable.

MR whistlers cause a moderate to small ionization rate that lasts longer (100 s) while ducted whistlers cause strong but short ( $< 1$  s) ionization bursts.

The ionization in the lower ionosphere caused by the energetic electrons precipitated by ducted whistlers has been associated with perturbations (so called 'Trimpi' effects) of amplitude and phase of subionospheric VLF, LF, and MF signals, characterized by a sudden onset that lasts from 0.5 to 1.5 s and a roughly exponential recovery of variable duration but a return to ambient within 100 s is common [*Burgess and Inan*, 1992 and references therein].

Ionospheric disturbances caused by MR whistlers would not be expected to have similar signatures, due to the fact that, as shown above, significant ionization changes would build up slowly with time. Since the precipitation due to MR whistlers would continue for up to  $\sim 100$  s, we can expect signal amplitude and phase change to exhibit slow variations in response to single lightning flashes. However, the fact that successive flashes are likely to occur at intervals of  $< 100$  s and the fact that the recovery times for the nighttime D-region [*Glukhov et al.*, 1992] are of the order of 10–100 s would complicate the signatures of this effect in subionospheric VLF data.

# 7.

## Suggestions for Future Work

During the course of the work presented above several ideas for future research have emerged. These topics can be divided into two groups, namely (i) applications of the existing test particle simulation model and (ii) further developments and extensions of the model.

### 7.1. Applications of the Test Particle Simulation Model

#### *Multiple Interactions of the Particle Distribution With the Wave*

The results presented in section 5.5 concerning the interaction between radiation belt electrons and MR whistlers were based on a one pass interaction involving a single encounter of each test particle with the wave. In principle, the distribution function obtained after one pass interaction can be used as the initial distribution function for a second encounter with the wave of all test particles and such an iterative procedure would allow the determination of the time evolution of the distribution function and precipitated particle fluxes. Note, however, that the regions of coverage of the distribution function must

be significantly expanded (nearly doubled) at each iteration and that the source processes for the radiation belt electrons must be taken into account in order for such an iterative process to accurately represent a realistic situation.

### *Interpretation of Satellite Data*

Combining the results of the simulation model with the actual satellite data on MR whistler mode waves from lightning and VLF transmitters would enable the calibration of model predictions and the prediction and estimation of the long and short term time dependence, as well as the dependence on the  $L$ -shell, of magnetospheric distribution functions and precipitated particle and energy fluxes. At the simplest level, better statistics on the distribution of non-ducted whistler intensities and wave normal angles are needed to provide quantitative input for modeling.

### *Effects on the Upper Ionosphere*

A quantitative investigation of the effects of the calculated precipitated particle fluxes on the upper ionosphere compared with past and future measurements would provide a bench mark test for the model validity and its predictions. This study may include modeling of the temporal and spatial dependence of secondary ionization, light emission and other effects of the precipitated radiation belt electron fluxes on the ionosphere and further influence of these effects on the magnetosphere. For example, is it possible that the secondary ionization effect of electrons precipitated by MR whistlers originating in a thunderstorm is strong enough to create ionization build up that by upward diffusion forms a duct, as suggested by *Jasna et al.*, 1992?



## 7.2. Further Developments of the Model

### *Variable Frequency and Discrete Wave Packets*

The main restrictions of the applicability of the model come from the requirements of a monochromatic and continuous wave. Therefore, the first step in an attempt to improve the simulation method would be to extend the test particle model to include wave frequency variations and transient (i.e. pulsed propagation) effects. This would open for investigation a whole new area of resonant interactions between radiation belt electrons and oblique, incoherent, time dependent signals. The wave frequency variations and transient (i.e. pulsed propagation) effects have already been incorporated into test particle simulation models of interactions with ducted waves [Chang, 1983; Chang and Inan, 1983a; Chang and Inan 1983b; Chang et al., 1983; Chang and Inan, 1985; Bell and Inan, 1981; Inan et al., 1982]. Their results combined with our one-pass model, form an excellent basis for future developments of our model to include temporal variations of wave frequency and intensity.

### *Raytracing*

Once the model is extended to include resonant interactions with oblique, variable frequency and temporally structured signals the next step further would be to combine it with a generalized ray tracing formulation [Burtis, 1974; Inan and Bell, 1977] to include more accurate determination of the wave. This would broaden the wave-particle interaction regions from a particular  $L$ -shell to the larger regions which are illuminated by the waves and would allow the incorporation of dependence of the particle distribution function on  $L$ -shell, so that the particle distribution functions can be defined and studied over a range of  $L$ -shells rather than at a particular one.

*Effects of Particles on the Wave*

The mathematical model used in this report neglected the influence of the resonant particle-wave interaction on the wave. A more general solution, however, should include the energy transfer between the particle and the wave during the interaction in both directions, i.e., the modification of the wave in accordance with the fields radiated by the currents produced by the particles [Helliwell, 1967]. This should be done at the each step of the simulated interaction. One theoretical model for the space-time evolution of ducted whistler mode wave growth was developed by Carlson *et al.* [1990]. Since the mechanism for growth in their work is cyclotron resonance between circularly polarized waves and gyrating energetic electrons, it may be possible to extend this research to include oblique whistler mode waves.

## References

- Akasofu, S. I. and S. Chapman, *Solar Terrestrial Physics*, Oxford at the Clarendon Press, 1972.
- Angerami, J. J., and J. O. Thomas, Studies of Planetary Atmospheres, 1, The Distribution of Electrons and Ions in the Earth's Exosphere, *J. Geophys. Res.*, 69, 4537, 1964.
- Banks, P. M., and G. Kockarts, *Aeronomy (Part B)*, Academic Press, New York and London, 1973.
- Banks, P. M., C. R. Chappell, and A. F. Nagy, A New Model for the Interaction of Auroral Electrons With the Atmosphere: Spectral Degradation, Backscatter, Optical Emission, and Ionization, *J. Geophys. Res.*, 79, 1459, 1974.
- Bell, T. F., and U. S. Inan, Transient Nonlinear Pitch Angle Scattering of Energetic Electrons by Coherent VLF Wave Packets in the Magnetosphere, *J. Geophys. Res.*, 86, 9047, 1981.
- Bell, T. F., U. S. Inan, and R. A. Helliwell, Nonducted coherent VLF waves and associated triggered emissions observed on the ISEE-1 satellite, *J. Geophys. Res.*, 86, 4649, 1981.
- Bell, T. F., The Nonlinear Gyroresonance Interaction Between Energetic Electrons and Coherent VLF Waves Propagating at an Arbitrary Angle With Respect to the Earth's Magnetic Field, *J. Geophys. Res.*, 89, 905, 1984.
- Bell, T. F., The Wave Magnetic Field Amplitude Threshold for Nonlinear Trapping of Energetic Gyroresonant and Landau Resonant Electrons by Nonducted VLF Waves in the Magnetosphere, *J. Geophys. Res.*, 91, 4365, 1986.
- Burgess, W. C., and U. S. Inan, Simultaneous Disturbance of Conjugate Ionospheric Regions in Association With Individual Lightning Flashes, *Geophys. Res. Lett.*, 17, 259, 1990.
- Burgess, W. C., and U. S. Inan, The Role of Ducted Whistlers in the Precipitation Loss and Equilibrium Flux of Radiation Belt Electrons, *J. Geophys. Res.*, in press, 1992.
- Burtis, W. J., *User's Guide to the Stanford VLF Raytracing Program*, Stanford University, 1974.

- Carlson, C. R., R. A. Helliwell, and U. S. Inan, Space-Time Evolution of Whistler Mode Wave Growth in the Magnetosphere, *J. Geophys. Res.*, 95, 15,073, 1990.
- Carpenter, D. L., Whistler Evidence of a 'Knee' in the Magnetospheric Ionization Density Profile, *J. Geophys. Res.*, 68, 1675, 1963.
- Carpenter, D. L., Whistler Studies of the Plasmapause in the Magnetosphere; Temporal Variations in the Position of the Knee and Some Evidence on Plasma Motions Near the Knee, *J. Geophys. Res.*, 71, 693, 1966.
- Carpenter, D. L., and J. W. LaBelle, A Study of Whistlers Correlated With Bursts of Electron Precipitation Near L=2, *J. Geophys. Res.*, 87, 4427, 1982.
- Chang, C. H., Cyclotron Resonant Scattering of Energetic Electrons by Electromagnetic Waves in the Magnetosphere, *Tech. Rep. E414-1*, STARLAB, Stanford Electron. Labs., Stanford Univ., Stanford, Calif., 1983.
- Chang, H. C., and U. S. Inan, Quasi-Relativistic Electron Precipitation Due to Interactions With Coherent VLF Waves in the Magnetosphere, *J. Geophys. Res.*, 88, 318, 1983a.
- Chang, H. C., and U. S. Inan, A Theoretical Model Study of Observed Correlations Between Whistler Mode Waves and Energetic Electron Precipitation Events in the Magnetosphere, *J. Geophys. Res.*, 88, 10,053, 1983b.
- Chang, H. C., U. S. Inan, and T. F. Bell, Energetic Electron Precipitation Due to Gyroresonant Interactions in the Magnetosphere Involving Coherent VLF Waves With Slowly-Varying Frequency, *J. Geophys. Res.*, 88, 7037, 1983.
- Chang, H. C., and U. S. Inan, Lightning-Induced Electron Precipitation From the Magnetosphere, *J. Geophys. Res.*, 90, 1531, 1985.
- Chen, F. F., *Introduction to Plasma Physics and Controlled Fusion*, Plenum Press, New York, 1984.
- Dingle, B., and D. L. Carpenter, Electron Precipitation Induced by VLF Noise Bursts at the Plasmapause and Detected at Conjugate Ground Stations, *J. Geophys. Res.*, 86, 4597, 1981.
- Doolittle, J. H., Modification of the Ionosphere by VLF Wave-Induced Electron Precipitation, *Tech. Rep. E4-21301318*, Radiosci. Lab., Stanford Electron. Labs., Stanford Univ., Stanford, Calif., 1982.
- Draganov, A. B., U. S. Inan, V. S. Sonwalkar, and T. F. Bell, Magnetospherically Reflected Whistlers as a Source of Plasmaspheric Hiss, *Geophys. Res. Lett.*, 19, 233, 1992.

- Dungey, J. W., Loss of Van Allen Electrons Due to Whistlers, *Planet. Space Sci.*, 11, 591, 1963.
- Edgar, B. C., The Upper and Lower Frequency Cutoffs of Magnetically Reflected Whistlers, *J. Geophys. Res.*, 81, 205, 1976.
- Foster, J. C., and T. J. Rosenberg, Electron Precipitation and VLF Emissions Associated With Cyclotron Resonance Interactions Near the Plasmapause, *J. Geophys. Res.*, 81, 2183, 1976.
- Glukhov, V. S., V. P. Pasko and U. S. Inan, Relaxation of Transient Lower Ionospheric Disturbances Caused by Lightning-Whistler-Induced Electron Precipitation Bursts, *J. Geophys. Res.*, 97, 16,971, 1992.
- Goldberg, R. A., J. R. Barcus, L. C. Hale, and S. A. Curtis, Direct Observation of Magnetospheric Electron Precipitation Stimulated by Lightning, *J. Atmos. Terr. Phys.*, 48, 293, 1986.
- Gurnett, D. A., and L. A. Frank, VLF Hiss and Related Plasma Observations in the Polar Magnetosphere, *J. Geophys. Res.*, 77, 172, 1972.
- Gurnett, D. A., and U. S. Inan, Plasma Wave Observations With the Dynamics Explorer 1 Spacecraft, *Rev. Geophys.*, 26, 285, 1988.
- Helliwell, R. A., *Whistlers and Related Ionospheric Phenomena*, Stanford University Press, Stanford, Calif., 1965.
- Helliwell, R. A., A Theory of Discrete VLF Emissions From the Magnetosphere, *J. Geophys. Res.*, 72, 4773, 1967.
- Helliwell, R. A., J. P. Katsufakis, and M. L. Trimpi, Whistler-Induced Amplitude Perturbation in VLF Propagation, *J. Geophys. Res.*, 78, 4679, 1973.
- Helliwell, R. A., and J. P. Katsufakis, VLF Wave Injection Into the Magnetosphere From Siple Station, Antarctica, *J. Geophys. Res.*, 79, 2511, 1974.
- Helliwell, R. A., J. P. Katsufakis, T. F. Bell and R. Raghuram, VLF Line Radiation in the Earth's Magnetosphere and its Association With Power System Radiation, *J. Geophys. Res.*, 80, 4249, 1975.
- Helliwell, R. A., S. B. Mende, J. H. Doolittle, W. C. Armstrong, and D. L. Carpenter, Correlations Between  $\lambda 4278$  Optical Emissions and VLF Wave Events Observed at L~4 in the Antarctic, *J. Geophys. Res.*, 85, 3376, 1980.
- Helliwell, R. A., VLF Stimulation Experiments in the Magnetosphere From Siple Station, Antarctica, *Rev. Geophys.*, 26, 551, 1988.

Hess, W. N., *The Radiation Belt and the Magnetosphere*, Blaisdell Publishing Co., Mass., 1968.

Inan, U. S., Non-Linear Gyroresonant Interactions of Energetic Particles and Coherent VLF Waves in the Magnetosphere, *Tech. Rep. 3414-3*, Radiosci. Lab., Stanford Electron. Labs., Stanford Univ., Stanford, Calif., 1977.

Inan, U. S., and T. F. Bell, The Plasmapause as a VLF Wave Guide, *J. Geophys. Res.*, **82**, 2819, 1977.

Inan, U. S., T. F. Bell and R. A. Helliwell, Nonlinear Pitch Angle Scattering of Energetic Electrons by Coherent VLF Waves in the Magnetosphere, *J. Geophys. Res.*, **83**, 3235, 1978.

Inan, U. S., T. F. Bell, and H. C. Chang, Particle Precipitation Induced by Short-Duration VLF Waves in the Magnetosphere, *J. Geophys. Res.*, **87**, 6243, 1982.

Inan, U. S., D. L. Carpenter, R. A. Helliwell, and J. P. Katsufakis, Subionospheric VLF/LF Phase Perturbations Produced by Lightning-Whistler Induced Particle Precipitation, *J. Geophys. Res.*, **90**, 7457, 1985a.

Inan, U. S., H. C. Chang, R. A. Helliwell, W. L. Imhof, J. B. Reagan, and M. Walt, Precipitation of Radiation Belt Electrons by Man-Made Waves: A Comparison Between Theory and Measurement, *J. Geophys. Res.*, **90**, 359, 1985 b.

Inan, U. S., and D. L. Carpenter, On the Correlation of Whistlers and Associated Subionospheric VLF/LF Perturbations, *J. Geophys. Res.*, **91**, 3106, 1986.

Inan, U. S., and D. L. Carpenter, Lightning-Induced Electron Precipitation Events Observed at L2.4 as Phase and Amplitude Perturbations on Subionospheric VLF signals, *J. Geophys. Res.*, **92**, 3293, 1987.

Inan, U. S., Gyroresonant Pitch Angle Scattering by Coherent and Incoherent Whistler Mode Waves in the Magnetosphere, *J. Geophys. Res.*, **92**, 127, 1987.

Inan, U. S. and D. L. Carpenter, Seasonal, Latitudinal and Diurnal Distributions of Whistler-Induced Precipitation Events, *J. Geophys. Res.*, **92**, 3293, 1987.

Inan, U. S., T. G. Wolf, and D. L. Carpenter, Geographic Distribution of Lightning-Induced Electron Precipitation Observed as VLF/LF Perturbation Events, *J. Geophys. Res.*, **93**, 9841, 1988.

Inan, U. S., M. Walt, H. D. Voss, and W. L. Imhof, Energy Spectra and Pitch Angle Distributions of Lightning-Induced Electron Precipitation: Analysis of an Event Observed on the S81-1 (SEEP) Satellite, *J. Geophys. Res.*, **94**, 1379, 1989.

- Inan, U. S., F. A. Knifsend, and J. Oh, Subionospheric VLF "imaging" of Lightning-Induced Electron Precipitation From the Magnetosphere, *J. Geophys. Res.*, 95, 17217, 1990.
- Inan, U. S., and T. F. Bell, Pitch Angle Scattering of Energetic Particles by Oblique Whistler Waves, *Geophys. Res. Lett.*, 18, 49, 1991.
- Jasna, D., U. S. Inan and T. F. Bell, Equatorial Gyroresonance Between Electrons and Magnetospherically Reflected Whistlers, *Geophys. Res. Lett.*, 17, 1865, 1990.
- Jasna, D., U. S. Inan and T. F. Bell, Precipitation of Suprathermal (100 eV) Electrons by Oblique Whistler Waves, *Geophys. Res. Lett.*, 19, 1639, 1992.
- Kennel, C. F., and H. E. Petschek, Limit on Stably Trapped Particle Fluxes, *J. Geophys. Res.*, 71, 1, 1966.
- Laaspere, T. and R. A. Hoffman, New Results on the Correlation Between Low-Energy Electrons and Auroral Hiss, *J. Geophys. Res.*, 81, 524, 1976.
- Lohrey, B., and A. B. Kaiser, Whistler-Induced Anomalies in VLF Propagation, *J. Geophys. Res.*, 78, 2142, 1979.
- Lyons, L. R., R. M. Thorne, and C. F. Kennel, Electron Pitch-Angle Diffusion Driven by Oblique Whistler-Mode Turbulence, *J. Plasma Phys.*, 6, 589, 1971.
- Lyons, L. R., R. M. Thorne, and C. F. Kennel, Pitch-Angle Diffusion of Radiation Belt Electrons Within the Plasmasphere, *J. Geophys. Res.*, 77, 3455, 1972.
- Lyons, L. R., and R. M. Thorne, Equilibrium Structure of Radiation Belt Electrons, *J. Geophys. Res.*, 78, 2142, 1973.
- Mende, S. B., R. L. Arnoldy, L. J. Cahill, Jr., J. H. Doolittle, W. C. Armstrong, and A. C. Fraser-Smith, Correlation Between  $\lambda 4278$ -A Optical Emissions and a Pc 1 Pearl Event Observed at Siple Station, Antarctica, *J. Geophys. Res.*, 85, 1194, 1980.
- Park, C. G., Methods of Determining Electron Concentrations in the Magnetosphere from Noise Whistlers, *Tech. Rep. 3454-1*, Radioscience Laboratory, Stanford Electron. Labs., Stanford Univ., Stanford, Calif., 1972.
- Park, C. G., The Role of Manmade VLF Signals and Noise in Wave-Particle Interactions in the Magnetosphere, *Proc. International Symp. on Solar-Terrestrial Physics*, Boulder, Colo., D. Williams (ed.), June 1976.
- Park, C. G., D. L. Carpenter, and D. B. Wiggin, Electron Density in the Plasmasphere: Whistler Data on Solar Cycle, Annual, and Diurnal Variations, *J. Geophys. Res.*, 83, 3137, 1978.

- Ratcliffe, J. A., *Physics of the Upper Atmosphere*, Academic Press, New York and London, 1960.
- Rees, M. H., *Physics and Chemistry of the Upper Atmosphere*, Cambridge University Press, Cambridge, 1989.
- Roberts, C. S., Electron Loss From the Van Allen Zones Due to Pitch Angle Scattering by Electromagnetic Disturbances, *Radiation Trapped in the Earth's Magnetic Field*, ed. by B. M. McCormac, D. Reidel Publ. Co., Dordrecht-Holland, 1966.
- Roberts, C. S., Cyclotron Resonance and Bounce Resonance Scattering of Electrons Trapped in the Earth's Magnetic Field, *Earth's Particles and Fields*, ed. by B. M. McCormac, Reinholdt, New York, 1968.
- Roberts, C. S., Pitch-Angle Diffusion of Electrons in the Magnetosphere, *Rev. Geophys.*, 7, 305, 1969.
- Roederer, J. G., *Dynamics of Geomagnetically Trapped Particles*, Springer, New York, 1970.
- Rosenberg, T. J., R. A. Helliwell, and J. P. Katsufakis, Electron Precipitation Associated With Discrete Very-Low-Frequency Emissions, *J. Geophys. Res.*, 76, 8445, 1971.
- Rosenberg, T. J., J. C. Siren, D. L. Mathews, K. Marthinsen, J. A. Holtet, A. Egeland, D. L. Carpenter, and R. A. Helliwell, Conjugacy of Electron Microbursts and VLF Chorus, *J. Geophys. Res.*, 86, 5819, 1981.
- Schild, M. A., and L. A. Frank, Electron Observations Between the Inner Edge of the Plasma Sheet and the Plasmasphere, *J. Geophys. Res.*, 75, 5401, 1970.
- Schulz, M., and L. J. Lanzerotti, *Particle Diffusion in the Radiation Belts*, Springer, New York, 1974.
- Sonwalkar, V. S., and U. S. Inan, Thunderstorm Coupling to the Magnetosphere, to be submitted to *J. Geophys. Res.*, 1993.
- Spjeldvik, W. N., and R. M. Thorne, The Cause of Storm After Effects in the Middle Latitude D-Region, *J. Atmos. Terr. Phys.*, 37, 777, 1975.
- Stix, T. H., *The Theory of Plasma Waves*, McGraw-Hill, New York, 1962.
- Thorne, R. M., E. J. Smith, R. K. Burton and R. E. Holzer, Plasmasheric Hiss, *J. Geophys. Res.*, 78, 1581, 1973.
- Tsurutani, B. T., and E. J. Smith, Postmidnight Chorus: A Substorm Phenomenon, *J. Geophys. Res.*, 79, 118, 1974.



Uman, M. A., *Lightning*, Dover Publications, Inc., New York, 1984.

Vickrey, J. F. and M. C. Kelley, Irregularities and Instabilities in the Auroral F Region, in *High-Latitude Space Plasma Physics*, edited by B. Hultqvist and T. Hagfors, Plenum Publishing Corporation, 1983.

Voss, H. D., W. L. Imhof, J. Mobilia, E. E. Gaines, M. Walt, U. S. Inan, R. A. Helliwell, D. L. Carpenter, J. P. Katsufakis, H. C. Chang, Lightning-Induced Electron Precipitation, *Nature*, 312, 740, 1984.

Walt, M., W. M. MacDonald, and W. E. Francis, Penetration of Auroral Electrons Into the Atmosphere, in *Physics of the Magnetosphere*, edited by R. L. Carovillano, J. F. McClay and H. R. Radoski, pp. 534-555, D. Reidel, Dordrecht, Holland, 1968.